University of Southampton

THE STRUCTURE AND CATALYTIC BEHAVIOUR OF SUPPORTED RHODIUM AND RHODIUM/PALLADIUM NANOPARTICLES

Bhrat Jyoti

A thesis submitted for the Degree of Master of Philosophy

Department of Chemistry

December 2002

UNIVERSITY OF SOUTHAMPTON

ABSTRACT

FACULTY OF SCIENCE
CHEMISTRY

Master of Philosophy

THE STRUCTURE AND CATALYTIC BEHAVIOUR OF SUPPORTED RHODIUM AND RHODIUM/PALLADIUM NANOPARTICLES

By Bhrat Jyoti

Energy Dispersive Extended X-ray Absorption Fine Structure (EDE), Transmission Electron Microscopy (TEM) and X-ray Photoelectron Spectroscopy (XPS) have been employed as principle techniques to investigate the local structure and catalytic properties of Rh and Rh/Pd nanoparticles supported on γ-Al_2O_3.

The Rh catalyst systems were prepared with a metal loading from 2.5wt% to 10wt%, and included systems prepared with chlorinated and nitrated precursors. The Rh/Pd systems were prepared with a combination of the metal components that did not exceed 5wt%.

All of the Rh only systems exhibited a rapid room temperature oxidation in their 'fresh' states, which was seen to be a recurring trend with the chlorinated systems, irrespective of particle size depicted by TEM. The oxidation, also delineated by XPS, under these conditions was seen on the highly dispersed systems, which would not be predicted by the low dispersed, bulk case. The nitrated Rh systems exhibited a reduced propensity for the oxidation, and EXAFS and TEM data reported that particle size effects were not the reason for the observed structural differences. Re-oxidation of the systems after exposure to H_2 did appear to vary with metal loading, pointing to a structural factor. However, the dynamic equilibrium between the oxidised and reduced Rh phases was still present. These differences were not propagated under the catalytic conditions employed, which was the reduction of NO by H_2. All of the systems exhibited virtually the same activity and selectivity, and the consequent production of N_2O could therefore be assigned to be intrinsic to the bi-stable Rh nanoparticles. After 'light off' and the collapse of the oxidised Rh phase, particulate Rh was seen to be very selective for the reduction of NO to N_2.

The introduction of an adjunct metal, palladium, to these systems to potentially remove the bi-stable Rh phase and unwanted production of N_2O resulted in alloying between the components and a segregation of Pd to the surface of the particles, shown by XPS. Both the EDE and XPS results showed varying the loading of Pd could subsequently change the phase of the Rh, and therefore the Rh could be insulated against the aforementioned oxidation. However, although the phase was eliminated, the production of N_2O was found to be an intrinsic catalytic property of Pd, and no 'intermediate' phase was found to exist.

The study of a physically mixed sample found the system, somewhat surprisingly, to be the 'desired' catalyst in the scope of this study. The Pd component was found to 'communicate' with the Rh via what was most likely H_2 spillover. This meant that although the oxidation of the discrete Rh component still transpired, the promotion of this phase to the highly selective metallic phase occurred at much lower light off temperatures compared to the alloyed systems. The absence of 'Pd-like' behaviour, when compared to the 'Pd-only' system, showed a physical result of the proposed H_2 spillover. However, for the elimination of consequent N_2O production and an understanding of the complex processes occurring over all of the systems studied, further work and concepts need to be evoked.

In summary, the *in situ*, time resolved, double edge EDE/MS experiments has allowed the observation of a range of dynamic processes occurring over the catalyst systems during the reduction of NO by H_2. The complimentary probes utilised showed the physical behaviour of the systems in unprecedented detail, both statically and in time-resolved studies.

Contents

Chapter 3- Rhodium Only Systems

Chapter 4- Rhodium and Palladium Systems

Acknowledgements

I would firstly like to thank my supervisor Professor John Evans for all his support and guidance throughout my MPhil, and for looking after me at the ESRF and Daresbury (supplies of beer and cakes!!). I would also like to thank my 'second' supervisor Dr Mark Newton for his constant guidance, help and humour, without which this thesis would not be as it is. There are too many 'thank you' factors associated with Mark, so all I can say is I am looking forward to the next three years of my PhD! I would also like to thank Dr Steven Fiddy and Dr Andy Dent for all the assistance they have given me. Thanks are also due to Dr Sofia Diaz-Moreno at the ESRF for all the help she gave.

I promised that I would mention the following people on my floor, so here they are (only joking guys!): Colin, "Vince", Tickler Graham, Pete and Tony.

I would also like to thank my best friends, all the Bellemoor lot, Symonds' lot and the 'Monte' lot, you know who you are, and you are too many to list! A special thanks to my mate Bon, we are in this together man!!

Lastly, but by no means least, I would like to thank my family, my sisters, mum and dad (and sonny!)

Chapter 1

Introduction

1.1 Introduction

This thesis encompasses an investigation into the dynamic surface chemistry of selected supported rhodium and palladium catalysts. The scope of this investigation specifically targets an understanding of the nature of the Rh and Pd nanoparticles, and their subsequent properties under reactive conditions. The experimental methodologies will endeavour to not only observe the catalytic dynamics present but also concentrate on the structural effects and processes that occur within these systems. The main techniques employed for these aims are Extended X-ray Absorption Fine Structure (EXAFS), principally Energy Dispersive EXAFS (EDE), X-ray Photoelectron Spectroscopy (XPS) and Transmission Electron Microscopy (TEM). All of these spectroscopic techniques are related in their basic principles, but yield differing information on the systems under investigation. All of the techniques employed have been chosen to give a 'complete' understanding as possible into the complex 'whole' of the systems utilised. This chapter therefore serves as an overview of the field of heterogeneous catalysis, related existing work and the overall aims of the project. It will also introduce the catalytic processes chosen for the observation of the activity and properties of the systems.

1.2 Catalysis

The definition of a catalyst is that it increases the rate at which a chemical reaction reaches equilibrium, by lowering its activation energy, without itself being consumed in the process. A catalyst may therefore produce a greater proportion of the desired product, as it may selectively lower just one of the several reaction pathways that are present. Catalysts are therefore extensively utilised in nature, industry and in the laboratory. An example of the importance of catalysts is evident in the estimation that they contribute to one-sixth of the value of all manufactured goods in industrialised countries,[1] and nearly 70% of all industrial chemical processes use a catalyst at some stage in their manufacture.[2]

The subject of catalysis can be divided into two broad domains, homogeneous and heterogeneous catalysis. The differences between these two areas can be viewed effectively by looking at the properties of each catalyst type with respect to the phases present.

Homogeneous catalysts are generally based around well defined organometallic compounds which may be synthesised with a high degree of purity. As such, and at least initially, such systems present only one form of active site to the substrate molecules. Therefore homogeneous catalysts generally yield a high level of selectivity.

However, as the reactants, products, and the catalyst itself, exist in the same phase, separation of these components, and reclamation/recycling of the catalysts, can be problematic.

These problems are minimised when the catalysts, products, and reactants exist in differing phases, as is the case with a heterogeneously catalysed reaction. However, the use of solid catalysts leads to a greater potential for unwanted 'side' reactions and therefore decreased selectivity- the surfaces of the active phase and support material are heterogeneous in an unwanted sense.

In heterogeneous systems the notion of dispersion is used to describe the effective concentration of active metals sites. Simply stated as the fraction of active phase atoms existing at the surface of the catalyst, this recognises the fact that only active phase atoms at the surface of supported particles will be available for reaction. Therefore, by using a high area dispersant, such as alumina, and nanoscale active phase particles, very large effective concentrations of the active and therefore high turnovers can be achieved. This simple notion is, however, predicted on the assumption that the reactive properties of the active phase are not adversely affected by the increasingly smaller size of the active phase particles required to obtain the greatest dispersion. The high proportion of exposed, and hence potentially 'active' atoms means a definite catalytic advantage over other similar heterogeneous systems. These low dispersed systems include single crystal and thin film analogues which, explained below, exhibit markedly different catalytic behaviour to highly dispersed systems.

Therefore the most effective catalyst in principle would be a heterogeneous catalyst with only one type of active/catalytic site. Due to this ease of separation of products, heterogeneous catalysts are used in the majority of industrial processes.[3]

1.3 Supported Rhodium and Palladium Metal Species

The deposition of metal particles onto supports to yield a catalyst is a method that is often used throughout industry. Examples of these systems are diverse and numerous as is their application. Some of the most commercially viable and widely known application of these systems is the use of specific noble metals, such as finely divided platinum-rhodium particles, in automobile catalytic converters for conversion of exhaust gases, such as CO and hydrocarbon oxidation to CO_2. Another primary reaction associated with this system is the reduction of NOx species to N_2.

The choice of γAl_2O_3 as the oxide support used for the catalysts was based on it being a prototypical material in this field of study. Of the two forms of anhydrous alumina, the other being αAl_2O_3, γAl_2O_3 exhibits a 'defect' spinel structure, with a deficit of cations.

γAl_2O_3 combines a relatively high surface area (ca. 100 m^2g^{-1}) with advantageous physical properties such as thermal stability, making it a potentially useful dispersant for active metal species. Al_2O_3 also possesses both Brønsted (OH groups) and Lewis acid (Oxygen deficient Al sites) character. However, whilst these properties are exploited in a variety of areas in catalysis, they will not be considered in detail here, as they are not significant contributors to the catalytic reaction under the study in this thesis.

Perhaps the most effective method to visualise the basic properties of rhodium and palladium as catalysts is in their role in the 'three way' automotive exhaust catalyst system. The scope of these systems is inherently related to this study, with factors such as the use of NO/H_2 gas in experimental conditions closely related.

1.4 The Three-Way Automotive Exhaust Catalyst System

The use and continual development of automotive three-way catalysts have been an active and dynamic area of chemistry and other domains, such as engineering, since their commercial introduction in the early 1980s.

The three-way catalyst system therefore simultaneously promotes the reduction of nitrogen oxides and the oxidation of carbon monoxides and hydrocarbons. The net principle reactions that are performed by these catalysts are therefore as follows:

$$2NO + 2CO \rightarrow N_2 + 2CO_2 \quad (1.1)$$

$$2NO + 2H_2 \rightarrow N_2 + 2H_2O \quad (1.2)$$

Reactions (1.1) and (1.2) are therefore the desired reactions to take place over the catalyst.

Prior to this, emission control catalysts were purely oxidation catalysts, and the reduction of the nitric oxides was achieved via various engine modifications, namely exhaust gas recirculation.[1]

The detrimental environmental effects of exhaust emissions have seen various worldwide exhaust emission regulations, and therefore the increased use of catalytic converters. Other stringent laws such as the Zero Emission Vehicle and emission standards have led to the perpetual development of these catalysts and all the related systems involved.[4]

The typical 'ceramic monolith' catalytic converter is composed of cordierite ($2MgO.2Al_2O_3.5SiO_2$) in a honeycomb structure. This is covered with a layer of alumina, 30-50μm thick, which acts as a support for all the metals. Other additives such as ceria are added to increase the durability and performance of the catalyst. The catalyst composition varies to application, but the primary metal constituent in all three-way catalysts is rhodium, the noble metal that is primarily associated with the reduction of NO_X species.

The increasing use of palladium, for the effective oxidation of CO and hydrocarbons, in the bimetallic system over the use of platinum is due to the increased durability under high temperature oxidising conditions and a lower light-off temperature. However, the relative use of Pt and Pd in catalyst formulation fluctuates in response to the cost, and other economic factors, of these metals.

The recent interest in replacing rhodium and/or platinum with palladium due to these economic factors has lead to extensive studies into the effectiveness of the idea. As mentioned before, rhodium is favoured over all three metals for the reduction of NO_X species. It also has comparatively high activity, low ammonia production and a NO_X conversion 'window' that extends to leaner or more oxidising conditions. This has significant ramifications for recent 'lean burn' engines,[5] in which progressively more oxidising

conditions are used, i.e. a high air: fuel ratio. Palladium is less active in these conditions, and has a smaller activity 'window' in leaner conditions for NO_X conversion.

Although palladium is poisoned by lead over time, its durability and thermal stability is preferred over platinum. The main disadvantage of palladium can be observed in its poor conversion of NO_X species under net reducing conditions. Another disadvantage leading on from this includes the production of unwanted hydrogenation species such as NH_3. Other studies conducted for the reduction of the expensive rhodium component in these systems have suggested alloys comprising of platinum/molybdenum,[6] although no widely used solution has been implemented.

1.5 Related Catalytic Reactions And Existing Related Work

The principle catalytic reactions that occur over the surface of the catalytic converter form a basis of understanding of the processes that occur over the systems investigated in this study. The main target of engine management systems is the stoichiometric balancing of exhaust streams to yield a simultaneous reduction of NO_X products and oxidation of CO/hydrocarbons. In this sense the two principal and heavily studied reactions are the CO/NO reaction over rhodium and the reduction of NO by H_2 and hydrocarbons, the latter being most relevant in the current case. Figure 1.1 highlights the mechanism, proposed by Hecker and Bell,[4] of the reaction between NO and CO over rhodium. This can be summarised as the decomposition of nitric oxide proceeding the removal of the oxygen from the catalyst via a reaction with a reducing agent, in this case CO.

This reaction occurring over Rh, as with all the processes, is sensitive to the changes in the surface morphology of the incipient metal, i.e. differing kinetic behaviour ensuing over single crystal and supported catalysts.

$CO \rightarrow CO_a$ (1)

$NO \rightarrow NO_a$ (2)

$NO_a \rightarrow N_a + O_a$ * (3)

$NO_a + N_a \rightarrow N_2 + O_a$ * (4)

$2N_a \rightarrow N_2$ * (5)

$CO_a + O_a \rightarrow CO_2$ * (6)

$NO_a + N_a \rightarrow N_2O$ * (7)

$N_2O \rightarrow O_a + N_2$ * (8)

- * indicates irreversible reaction.
- Reaction 5 is thought to be the rate limiting step. The recombination of N_a is shown to be a function of Rh particle size, an issue addressed in this study.
- Reaction 7 is the reaction to be minimised, or eliminated in an 'ideal' catalyst.

Figure 1.1: Mechanism of the NO/CO reaction.

The overall catalytic reaction of the NO reduction by H_2 can be observed as:

$NO_x + H_2$ (and CO) $\rightarrow N_2 + CO_2 + H_2O$ (a)

In relation to this study, the concept of understanding and deriving the relationships between structure and reactivity, a widespread aim in many areas of science, comes into focus. In catalysis specifically, this aim is at the centre of understanding how a catalyst functions. This in turn means that factors such as catalyst design and modification can be rationalised.

Figure 1 highlights the CO/NO reaction occurring over metallic rhodium. The widespread view of the Rh component in such catalysts, and one that underpins the axiom that single metal crystals[7,8,9] may be utilised as reasonable models of the systems, is of an essentially static metallic phase over which the processes outlined above occur.

However, Rh nanoparticles are not static but labile in some environments. The corrosion of very small Rh particles under CO to yield supported $Rh^I(CO)_2$ species has been known and studied since 1957.[10] The driving force for this phase transforming process has been rationalised with relatively simple thermodynamic arguments based upon the molecular heat of adsorption of CO on Rh, and estimates of Rh-Rh bond energies in such particles.[7]

That this process is generally agreed to proceed via molecular adsorption of CO, this factor also limits the range of Rh particle size that may be corroded in such fashion. Therefore where quantitation has been undertaken this pathway is only significant for very small, very highly dispersed, Rh particles containing on average only ca. 10 atoms.

The contribution that this reaction path has under real catalytic conditions is not well known though the $Rh^{I}(CO)_2$ species has been shown to be a 'spectator' in CO oxidation catalysis.[11] However, it is also known that this species is thermally labile and susceptible to reduction by H_2.[12]

Recently a new type of adsorption driven process, that is demonstrably rapid and capable of instantaneously oxidising particles up to 20-30Å across (containing hundreds of Rh atoms), has been demonstrated. Moreover this process has been shown to be deterministic in terms of both selectivity and light off in the reduction of NO by H_2 over supported Rh catalysts.

This process is fundamentally different to the CO induced corrosion of small Rh particles as it is driven by the dissociation of oxidants such as NO[13] and O_2.[14] Molecular dissociation releases much more energy than molecular adsorption and in these cases proceed very rapidly. This results in a rapid local heating of the Rh particles leading to the potential for a rapid attainment of previously inaccessible equilibrium structures. In the case of Rh this results in an instantaneous change of phase from 'metallic' to 'oxidic' at room temperature. Single crystal Rh surfaces only show significant surface oxidation under extremely lean O/CO environments and only at temperatures in excess of 500K.[15,16,17] A metallic Rh phase is only obtained under relatively H_2 rich conditions and at temperatures where the new oxidised phase itself is unstable (ca. 470K).[13]

These observations help to explain why, for reactions involving NO models based upon measurements made on Rh single crystals fail to model net reaction orders and activation energies successfully.[7] Further similar effects are observed in CO oxidation.[14] By their very nature such models do not allow for gross changes in reactivity as a function of Rh particle size and therefore cannot model these sorts of metaphasic processes.

Given this evidence of the behaviour of highly dispersed Rh under the mentioned catalytic conditions, three criteria for a potential second metal to alloy with the Rh are proposed.

The adjunct metal should have a lower propensity to oxidise, and consequently a lower propensity to dissociate NO. The metal should also have the 'correct' chemistry in terms of contributing to the overall catalyst performance in areas such as CO/O_2 reactions and other important catalytic reactions such as hydrocarbon oxidation.

Both Pt and Pd could be selected as the second metal for alloying, but Pd was selected due to its increasing importance in the mentioned three-way catalyst system. Another factor for selecting Pd was the apparent synergistic behaviour observed when alloyed with Rh,[18] derived from structurally indirect probes such as Infrared spectroscopy and reactivity measurements.

The case of supported bimetallic catalysts, specifically Rh and Pd catalysts, again highlights some contradictory factors regarding the historical 'view' of these systems. As before, previous work[19] using single crystal and catalysts derived from pure metal[20] have concluded that at moderate temperatures, Rh and Pd are essentially immiscible across the compositional range. This is highlighted in figure 1.2, a phase diagram for a Rh-Pd system[20] showing the separation of the alloy into Pd-rich and Rh-rich phases at 873K.

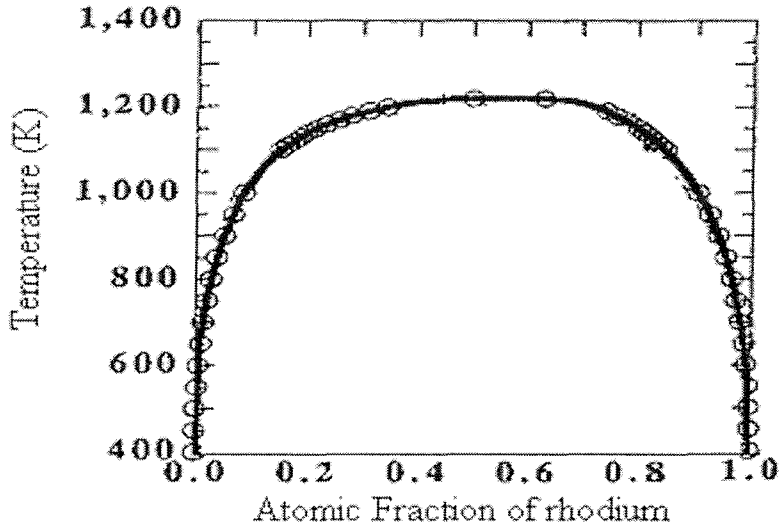

Figure 1.2: Phase diagram for the Rh-Pd system, showing the separations into metal-rich phases at 873K.[20] A single solid phase exists above the solid line, and a bi-phase below.

However, studies using IR,[21] observing CO and NO adsorption on SiO_2 supported Pd-Rh catalysts, indicate that, on the nanoscale the formation of alloyed particles is possible. The results obtained are not structurally deterministic, but offer the possibility of miscibility within the systems under investigation.

To investigate the structural factors stated above, a novel range of complementary experimental techniques are needed to observe the dynamic behaviour present in these systems. This can be achieved via X-ray photoelectron spectroscopy, and principally by Energy Dispersive EXAFS (EDE). The latter technique allows the interrogation of the active phase structure from both Rh and Pd *k* edges simultaneously and in a time resolved manner, which will yield a unique structurally deterministic perspective of the systems under investigation. Hence, in this study a microreactor based, EDE method is employed to probe both Rh and Pd *k* edges concurrently.

1.6 Aims Of This Thesis

This thesis will therefore endeavour to investigate a series of important questions posed on the systems under investigation.

Firstly, the factors affecting the catalytic systems consisting of only Rh will be investigated. The intrinsic properties of the systems with differing metal loadings and preparation technique will be probed, to highlight any changes with factors like reaction light off temperatures and selectivity between the systems. Other factors like increased metal loading affecting the apparent room temperature oxidation of Rh will be careful.

The inclusion of Pd with Rh will then be investigated, the basis of this being if alloy formation between the two metals is possible. If formation is possible, factors such as possible segregation events and total particle sizes will be observed. Structural determinations such as the respective positions on the surface of the support of the metals under differing conditions will also be probed.

A variety of preparation techniques of the Rh-Pd systems will be employed to investigate the possible differing catalytic performance, and whether the alloying is preparation dependent. A controlled experiment observing the intrinsic properties of a physical mixture of the two metals will be carried out to delineate any similarities and/or differences.

The role of Pd in the systems will be investigated, with factors such as the possible isolation of Rh against oxidation by Pd. If this protective property is observed, further experiments on the systems will be performed to outline any changes in the reactivity and selectivity of the catalysts.

1.7 References

(1) D.F Shriver, P.W. Atkins, C.H. Langford, 'Inorganic Chemistry', Oxford University Press, 1997

(2) Chemical and Engineering News, 'Survey of US industrial chemicals', April 12th 1993.

(3) W. Klein, *Angew. Chem., Intl. Ed. Engl.*, 1990, **29**, 235.

(4) K.C. Taylor, *Catal. Rev. Sci. Eng.*, 1993, **35**, 457.

(5) P. Araya, C. Ferrada, J. Cortés, *Catal. Lett.*, 1995, **35**, 175.

(6) N.W Cant, D.E. Angove, D.C. Chambers, *Appl. Cat. B.*, 1998, **17**, 63.

(7) V.P. Zhdanov, B. Kasemo, *Surf. Sci. Rep.*, 1997, **29**, 31.

(8) E.I Altman, R.J. Gorte, *J. Catal.*, 1988, **113**, 185.

(9) W.A. Brown, D.A. King, *J. Phys. Chem. B.*, 2000, **60**, 17.

(10) A.C. Yang, C.W. Garland, *J. Phys. Chem.*, 1957, **61**, 1504.

(11) P. Basa, D. Panyatov, J.T. Yates, *J. Phys. Chem.*, 1987, **91**, 3133.

(12) H.F.T. Van't Blik, J.B.A.D. Van Zon, T. Huizinga, J.C. Vis, D.C. Koningsberger, R. Prins, *J. Phys. Chem.*, 1983, **87**, 2264.

(13) T. Campbell, A.J. Dent, S. Diaz-Moreno, J. Evans, S.G. Fiddy, M.A. Newton, S. Turin, *Chem. Comm.*, 2002, 304.

(14) M.A. Newton, B. Jyoti, A.J. Dent, S. Diaz-Moreno, S.G. Fiddy, J. Evans, *J. Phys. Chem. B.*, Submitted.

(15) C.H.F. Feden, D.W. Goodman, D.S. Blair, P.J. Berlowitz, G.B. Fisher, S.H. Oh, *J. Phys. Chem.*, 1998, **92**, 1563.

(16) J. Koshy, *Thin Solid Films*, 1978, **51**, 217.

(17) G.L. Kellog, *J. Catal.*, 1985, **92**, 167.

(18) S.H. Oh, J.E. Carpenter, *J. Catal.*, 1986, **98**, 178.

(19) H. Noh, J.D. Clewley, T.B. Flanagan, A.P. Craft, *Journal of alloys and compounds*, 1996, **240**, 235.

(20) Y. Wang, J.S. Faulkner, *Phys. Rev. Lett.*, 1993, **70**, 3287.

(21) Y.J. Mergler, D.R.G. Ramsaransing, B.E. Nieuwenhuys, *Recl. Trav. Chim. Pays-Bas.*, 1994, **113**, 431.

Chapter 2

Experimental Methods

2.1 Introduction

The catalytic systems under investigation within the scope of this thesis have been studied using a variety of analytical techniques. The investigation of the complex catalytic systems requires techniques that are complimentary in nature, for a 'complete' understanding of the systems and the processes inherent to them. The techniques employed for this purpose include EXAFS (Extended X-ray Absorption Fine Structure), in particular EDE (Energy Dispersive EXAFS), which is the principal technique employed via microreactor experiments. The combination of the microreactor-based EDE with Mass Spectrometry allows the capacity to study both structure and reactivity simultaneously, factors that are major considerations in the scope of this study. TEM (Transmission Electron Microscopy), XPS (X-ray Photoelectron Spectroscopy) and BET (Brunauer Emmett Teller) measurements were also utilised. All of the techniques used are complementary and have assisted in the understanding of the structure and chemical processes occurring at the surface of the supported catalyst systems. EDE provides information concerning the local structure around the absorbing metal centre, which is continually monitored *in situ* throughout the temperature programmed reaction. This information includes determination of types of coordinating atoms, coordination numbers and bond distances. TEM was used as an adjunct technique providing information that was complementary to the average particle size information derived from EXAFS. XPS was utilised to further investigate the chemical nature of the 'fresh' Rh and Pd components, i.e. the relative composition of the particles in their bulk and at their surfaces. The technique was also used to semi-quantitatively assess levels of chlorine retention. This chapter therefore describes the methodologies utilised in this study, as well as the description of the techniques applied, in both a practical and theoretical manner. The manner in which the techniques are complimentary and their subsequent limitations within the scope of this study are also reported.

2.1.1 Basic considerations

A number of the techniques utilised here involve the detection of electrons that are emitted or scattered from the sample. As such these spectroscopies share a number of common principles and characteristics. For instance, XPS and EXAFS share core hole generation as the initial excitation event. All of the spectroscopies used utilise the fundamental physics of electron-matter interactions in differing ways to yield the information that they do.

2.1.2 Basic Processes: Inelastic and Elastic processes

2.1.3 Inelastic Processes

Inelastic processes in this case are scattering events that lead to a loss of energy in the electron. This energy loss effectively leads to the loss of information pertaining to the initial state from whence the electron was derived and any structural information that may only be derived from electrons that have been elastically scattered, i.e. with no concomitant loss of energy.

The presence of inelastic effects has two major ramifications. The first is the generation of an 'inelastic tail' of electrons at $E<E_B$. This tail contributes to background intensities that need to be subtracted from EXAFS and XPS prior to analysis; excessive scattering of this sort can therefore complicate data processing and subsequent analysis.

Secondly, and more fundamentally, inelastic scattering limits the physical distance over which elastically scattered electrons may be detected, and it therefore limits the effective range over which chemical state and structural information may be derived. Figure 2.1 shows an inelastic mean free path curve.[1]

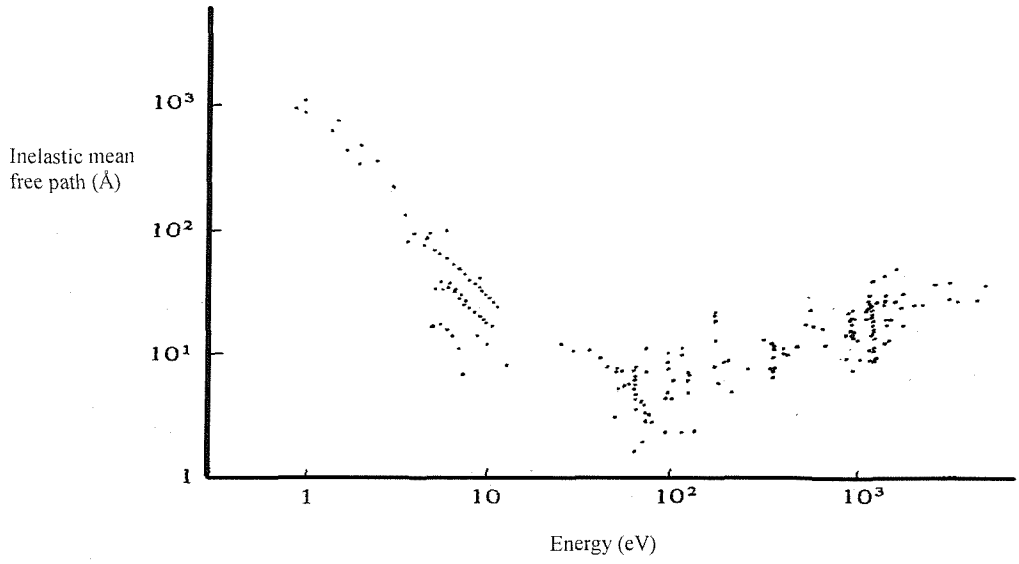

Figure 2.1: Collection of experimental determinations of inelastic scattering electron mean free paths as a function of energy above the Fermi level for many different materials.[1]

From the inelastic mean free path curve we can see that for electrons with kinetic energies typically detected in XPS (<1.5keV) that the mean free paths are relatively short (<20-30Å). It is this that gives XPS its intrinsic surface sensitivity as electrons will only escape the sample to be detected from the outer 20-30Å of the sample.

At the much higher electron energies used in TEM (ca. 100keV) it can be seen that the mean free paths of the electrons will be much greater, leading to the limiting requirement for sample thickness in TEM of ca. 1μm.

EXAFS in transmission mode (see below) does not utilise direct detection of the elastically scattered electrons and therefore has no intrinsic surface sensitivity. In this case however the effect of inelastic processes acts in a different way, limiting the distance over which elastically scattered electrons may travel before they experience energy loss and become non-contributory to EXAFS. As such, it is these processes that constrain the EXAFS effect to the determination of local structure information only.

2.1.4 Elastic Processes

Elastic processes that occur within the mentioned techniques fall under three main categories, diffraction, scattering and effects due to excitation/de-excitation events involving initially unoccupied molecular orbitals (XANES, see below). The scope of this study is primarily concerned with scattering events, although diffraction from the monochromators used in the apparatus can interfere considerably with EXAFS measurements for example. Diffraction can also be a useful tool in some TEM applications,[2] for example surface 3D modelling of clusters present.[3]

2.2 X-ray Photoelectron Spectroscopy (XPS)

A spectroscopy that utilises core level shifts to derive chemical state information is X-ray Photoelectron Spectroscopy (XPS). XPS uses a fixed (energetically) X-ray source (monochromated Al k_α, E_K=1486.6 eV, linewidth 0.35 eV in this thesis) to eject photoelectrons from the core levels of having energy E_b<hν. These electrons are then directly detected using a hemispherical electron analyser.

Photoelectron spectroscopy is in principle a simple process. When a photon of energy $h\upsilon$ penetrates the surface of a solid and is absorbed by an electron with a binding energy E_{BE} below the vacuum level, the electron can escape the atom with a subsequent kinetic energy E_{KE}. Equation 1 shows the Einstein relationship which is known as the photoelectric effect.

$$E_{KE} = h\upsilon - E_{BE} \qquad \text{eq. 2.1}$$

The distribution of the resultant photoelectron intensity with respect to its energy is therefore termed XPS. The photoionisation that occurs in fact requires a minimum of threshold photon energy for the electron to overcome the energy barrier between the vacuum and Fermi levels, which is the work function, denoted Φ.

XPS therefore involves photon excitation involving primary core level electron ejection. Following the formation of a core hole, Auger electron generation or fluorescence emission occur as secondary processes. These processes lead to separate techniques in themselves and have differing sensitivities according to the size of the emitting atom. The energy relationships in these processes are as follows:

$$E_{KE} = h\upsilon - E_K - \Phi \quad \text{(XPS)} \quad \text{Eq. 2.2}$$

$$E_A = E_K - E_{L1} - E^*_{L2,3} \quad \text{(Auger)} \quad \text{Eq. 2.3}$$

$$h\upsilon' = E_K - E_{L1} \quad \text{(Fluorescence)} \quad \text{Eq. 2.4}$$

The L1 term nominally corresponds to the 2s energy level, which in turn denotes K- s L1 as being forbidden. The L2,3 terms from the 2P energy level therefore corresponds to a Kα doublet.

The core energy levels are measured from the Fermi energy level. The asterisk indicates the excited state after producing the core hole in level L_1. These processes can be visualised in figure 2.2, which shows an energy level diagram[4] highlighting the fundamental XPS processes following the formation of a core hole state.

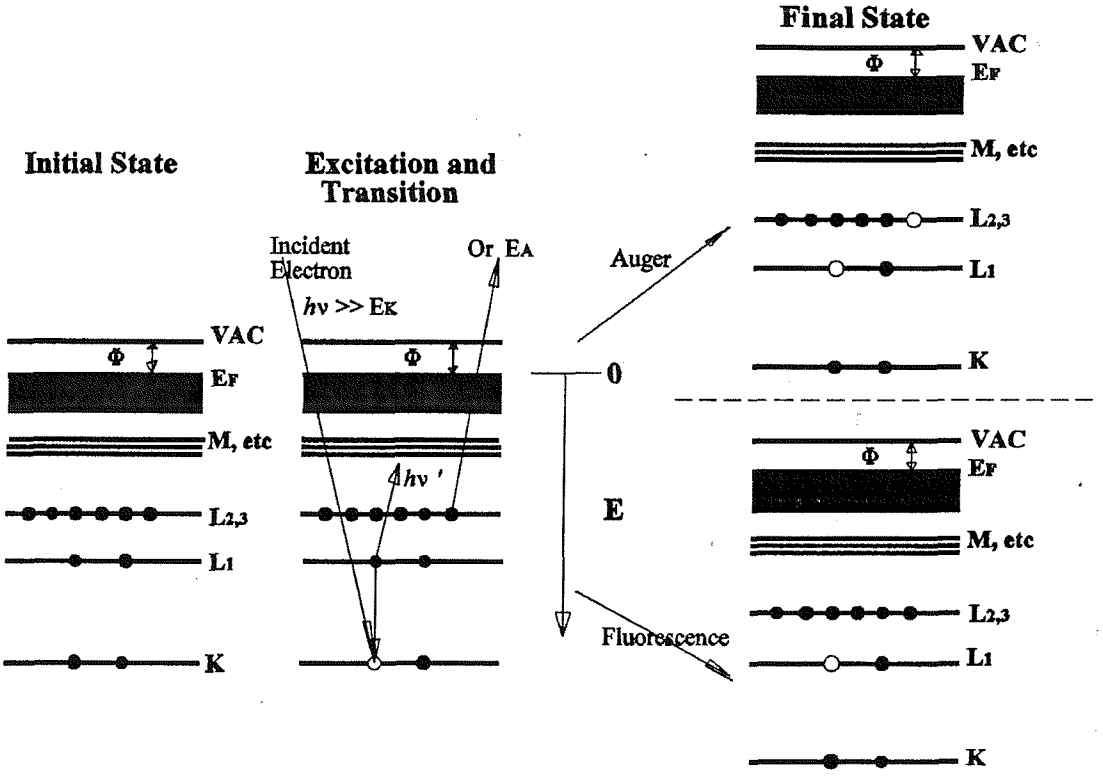

Figure 2.2: Energy level diagram showing the fundamental XPS process and Auger electron/fluorescence emission following formation of a core hole state.[4]

It is important to note here that only XPS reflects the initial state directly; Auger emission and fluorescence are the result of the final states response to the creation of a core hole.

The initial state argument here is that the E_B of the XPS electron reflects directly the effective charge felt by the initial core level electron and is therefore indicative of the chemical state of the unexcited atom. This means that core level shifts due to particle size, photoemission from surface atoms (as compared to bulk), which do not directly reflect the initial chemical state can also complicate analysis. Therefore a relationship exists between the inherent binding energy and the chemical state of the element.

XPS measurements in the scope of this study will therefore be used to elucidate the Rh and Pd ratios and the Rh, Pd and Cl ratios present in the catalytic systems. The chemical state of the elements in their 'fresh' state exposed to air will also be estimated.

2.2.1 Experimental

XPS measurements were carried out using a Scienta ESCA300 XPS analyser. The Al X-rays used were monochromated, yielding a net energy resolution of ca. 0.35 eV.[5] The samples were pressed into 7mm discs using a maximum of 1.25 tons of pressure and ca. 20mgs of sample. Samples that could not be pressed into discs were mounted onto hydrocarbon tape before analysis. The base pressure of the analysis chamber was $5x10^{-10}$ mbar, and a 'load lock' system was used for the introduction of the samples.

The compositional analysis performed on the catalyst systems utilised a different method for analysis than the discrete chemical state analysis explained above. The compositional analysis uses the total intensity measurements obtained rather than the peak positions. The analysis also relies upon the knowledge of the relative probabilities of core level excitation from each level involved.

2.3 XANES

Figure 2.3.1 highlights the XANES region in an absorption spectrum of a palladium foil, which runs from just before the edge to ~ 50 eV beyond the edge. The sharp peaks and oscillations present are caused by electronic transitions of the core electron to discrete bound valence levels, just before and on the edge.

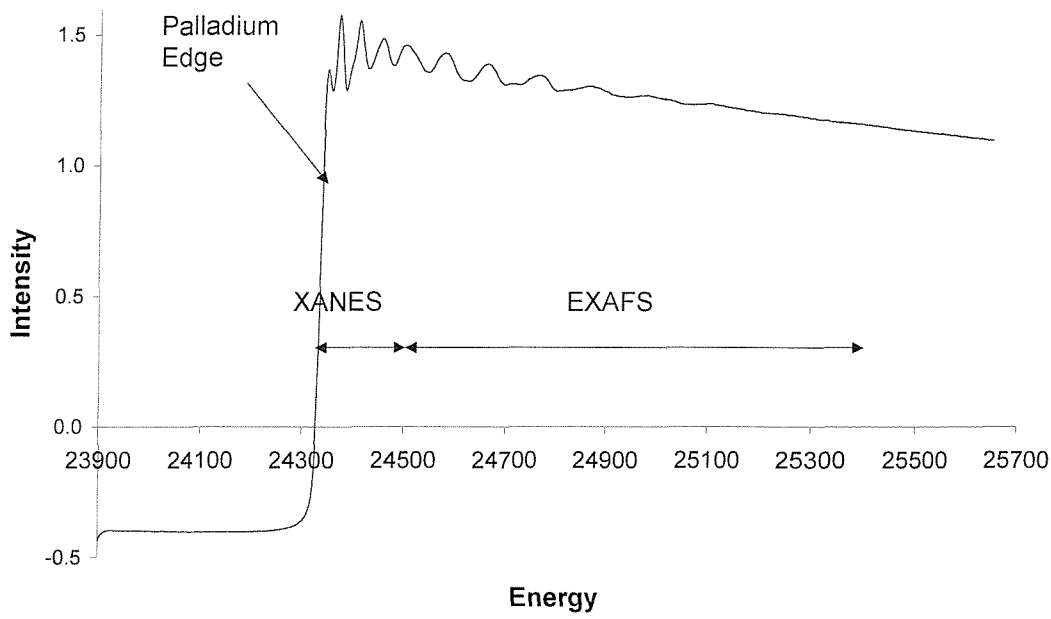

Figure 2.3.1: An X-ray absorption spectra of a palladium foil, highlighting the regions of interest.

The structure observable in the XANES region is dominated by excitations into unoccupied electron states. As with XPS, to a first approximation XANES is a probe of chemical state and electronic structure. However, as the inelastic mean free path curve of the electrons at these energies (<50 eV) are very long, this situation is greatly complicated by the potential for complex multiple scattering events.

Because of this, and the limited energy resolution of the EDE experiment as carried out in this thesis, means that this region has not been studied in detail. Measurements of the intensity of the 'white line' in such spectra have, however, been used qualitatively to assess the net levels of oxidation in the Rh component.

2.4 EXAFS

2.4.1 EXAFS Theory

Extended X-Ray Absorption Fine Structure spectroscopy (EXAFS) is a technique utilised in this study to provide local structural information of the surface-supported metal species.

When an X-ray of a particular wavelength impinges upon an atom, the radiation may be absorbed. This effect causes the subsequent ejection of a core electron with an energy equal to the incident X-ray energy minus its binding energy. This in turn results in an outgoing photoelectron wave from the absorbing atom. Modulation of this wave occurs by backscattering from the surrounding atoms. EXAFS is therefore the phenomenon of oscillations in the absorption coefficient as both the outgoing and backscattered waves interfere, constructively or destructively, on the variation of the X-ray beam wavelength.

This process occurs due to the wavelength of the ejected photoelectron being dependant on its energy, and therefore the phase of the backscattered wave at the central absorbing atom will consequently change with the energy of the incoming photon.

$\mu(E)_x$ is the absorbance and can be represented by:

$$\mu(E)_x = [\mu(E)_s + \mu(E)_m + \mu(E)_0 + \mu(E)_{EXAFS}]_x \qquad \text{Eq. 2.5}$$

The absorbance is therefore the addition of $\mu(E)_s$, the sloping spectrometer baseline, $\mu(E)_m$ the absorption due to the matrix in which the absorbing atom is embedded, $\mu(E)_0$ the absorption observed for the corresponding free atom, and $\mu(E)_{EXAFS}$ represents the modulation in the adsorption around $\mu(E)_0$. The EXAFS intensity, represented by $\chi(E)$, is contrived by subtraction of the background components and normalisation with respect to the free atom absorption. This is represented by equation 2.6:

$$\chi(E) = \mu(E)_{EXAFS}/\mu(E)_0 = [\mu'(E)/\ \mu(E)_0] - 1 \qquad \text{Eq. 2.6}$$

A schematic view of this phenomenon is shown in figure 2.3.2:

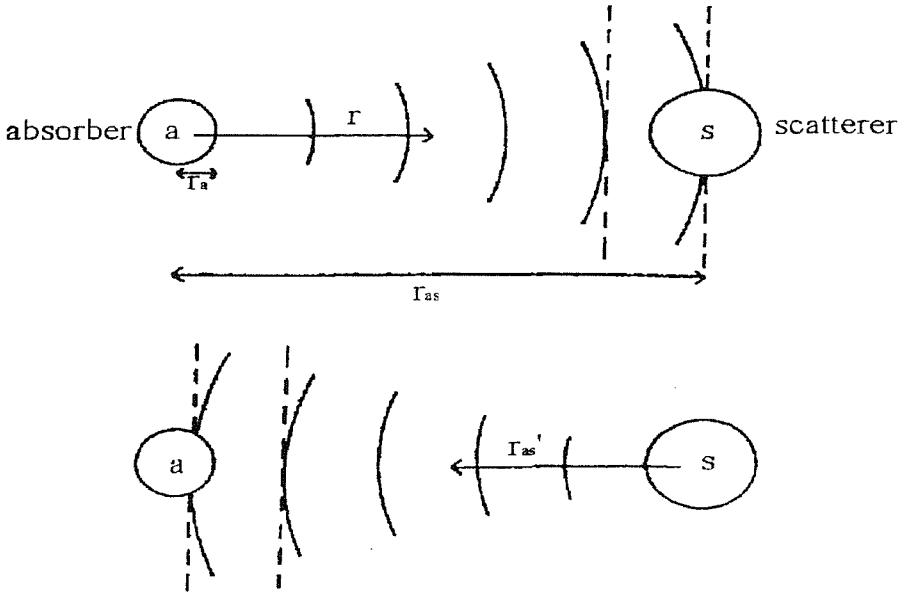

Figure 2.3.2: A schematic of the EXAFS scattering phenomenon.[35]

The phenomenon of multiple scattering takes effect if an ejected photoelectron encounters more than one backscattering atom before returning to the absorbing atom. This can be a significant contributor towards the overall EXAFS.

The first consideration here is that multiple scattering effects will tend to contribute at increasing k (electron energy); this is simply a result of the increasing mean free path of the electrons.

The multiple scattering effect will be highest for high symmetry arrangements of atoms. This is because at higher electron energies a second effect is seen. As the photoelectron energy increases, the cross section for back scattering (through ca. 360° and the principle effect used in EXAFS) diminishes. Concurrently the cross section for forward scattering (through 180°) increases. What this means is that atoms in a linear configuration, for example, and beyond the principal scatterer, will experience an enhanced flux of electrons and thus contribute to the observed EXAFS to a greater degree than they would in the absence of this effect.

EXAFS therefore has a significant advantage of being an analytical technique that is element specific and can be utilised regardless of the physical state of the material.

Systems that are in solution, in the gas phase or amorphous solids can therefore be characterised. The problem associated with poor signal to noise ratio obtained is a definite disadvantage. This is due to the oscillation of the absorption coefficient being a weak effect, which requires a high X-ray flux to obtain a workable signal to noise ratio.

The Debye-Waller (DW) factors associated with EXAFS are of central importance to this study due to the inherent effect it has on the EXAFS data. The Debye-Waller factor, denoted as σ^2, is consisted of two main components, caused by static and thermal disorder. An overview of the single scattering theoretical expression of the EXAFS event effectively highlights the origin of the DW factor and the relationship it has with temperature dependency in EXAFS intensities. The generally used EXAFS equation for an unoriented sample with Gaussian disorder with only one type of atom present in the *j*th coordination shell is as follows.[6-12]

$$\chi(k) = (\mu-\mu_0) / \mu_0 \qquad \text{Eq 2.7}$$

$$= \Sigma \frac{\mathbf{N}_j F_j(k)}{kR_j^2} \exp(-2k^2 \sigma_j^2) \exp(-2R_j/\lambda) \sin[2kR_j + \phi_j(k)] \qquad \text{Eq 2.8}$$

Where $F_j(k)$ is the backscattering amplitude from each of the N_j surrounding atoms in the *j*th shell with a DW factor of $2\sigma_j^2$ R_j away. The term $\exp(-2R_j/\lambda)$ is used to account for the inelastic losses in the scattering process with λ being the electron mean free path. The term σ reflects the mean squared deviation in bondlength from the average (equilibrium) bond length due to static and dynamic variations in this parameter. Equation 2.8 therefore shows the close relationship between the DW factor and the effective coordination number obtained. The static disorder stems from the fact that all the atoms within a shell are at different distances from the central atom. Additionally, the distance of an atom from the absorbing species is not constant due to thermal motion effects. Therefore atoms that are close to the central atom will move in sync, this correlation becoming weaker at larger distances. This means that shells at larger distances from the central atom will have larger DW values, and also at higher temperatures. This apparent increase in DW values has a dampening effect on the EXAFS. Hence the analysis of the EXAFS data would be affected to

a large extent by the DW factors, as temperatures of up to 673K are used, and the determination of the correct DW factors is central to achieving the restoration of accurate spectra and hence reliable results. The result of the EXAFS equation therefore shows relationships that are related to this study:

$I \alpha Ne^{(-\sigma 2)}$, therefore Eq. 2.9

$N \alpha I/[e^{(-\sigma 2)}]$. Eq. 2.10

N is therefore a sensitive function of the DW factor and a small variation in the DW factor will result in a relatively large change in the value of N required to fit the measured intensity. Subsequently this effect will be greater at higher k values due to the k^2 term in the exponent in equation 2.10.

The experimental method that was utilised to determine the correct DW factors for the systems under investigation is given in the following chapters.

2.4.2 Data Acquisition

Synchrotron radiation is highly intense, highly collimated, electromagnetic radiation which can be produced over a broad range of wavelengths. These properties make it suitable to acquire EXAFS data. EXAFS spectra were recorded at the synchrotron source located at station ID24, Grenoble, France. There are two modes that can be used to acquire data, transmission and fluorescence mode.

2.4.3 Transmission mode

For samples in solution or as thin solid samples, EXAFS spectra are via two ionisation chambers. Io is placed in front of the sample, and I_t is placed behind in a linear arrangement. Noble gases are used in each chamber, each with differing X-ray absorption coefficients such that Io absorbs –20%, and I_t –80% of the incoming radiation. As the wavelength of the X-rays vary, the relative absorption is as follows:

$$I_t = I_0 \exp(-\mu t) \qquad \text{Eq. 2.11}$$

[μ= absorption coefficient; t= thickness of sample.]

Solid samples are usually ground into a fine homogeneous powder, and either the sample is placed in the set up as described above, or into a suitable holder and a medium, such as air, is used as Io. The latter technique is therefore employed in this study.

2.4.4 Fluorescence mode

Fluorescence mode is used when the sample under investigation is too absorbing and cannot be diluted in any way without altering its inherent properties. It is also utilised when there is a low concentration of absorbing atoms present in the sample, i.e. in very thin or dilute samples. The fluorescence intensity is therefore the measure of absorption probability. The fluorescence yield over the background scatter is maximised (for dilute samples) by placing the sample 45° to the X-ray beam, with the detector perpendicular to the beam.

2.5 Energy Dispersive EXAFS

EXAFS can be used for kinetic studies with regards to the often complex mechanisms involved during a chemical reaction. In addition to this, EXAFS studies can present the structures of intermediate species in catalytic systems. In much faster processes such as many *in situ* catalytic reactions, traditional scanning EXAFS does not have the capability to analyse these systems. This is because of the inherent time scales associated with the acquisition of

EXAFS spectra. A popular approach to this problem is the isolation of the labile intermediate via low temperatures to allow enough time for spectra to be taken.
In addition to this the acquisition time has been reduced by the increased use of insertion devices at synchrotron sources.

Another technique in the form of Quick EXAFS (QEXAFS), allows EXAFS spectra to taken over a range of around 500eV in less than two minutes.[13] This is achieved by a continuously driven, cooled monochromator, which is used in conjunction with a fast solid state detector.[14,15] The lower *k* range employed, and lower signal to noise ratio in the subsequent data means that, in general, only a restricted number of shells are analysable.[16]

Energy Dispersive EXAFS (EDE) on the other hand is a technique that uses an elliptically bent crystal monochromator to simultaneously yield the required spectral range.[17-20] The monochromator either be in reflection or transmission geometry. The sample to be analysed is placed at the focal length of the monochromator, and a position-sensitive detector measures the intensity of the differing wavelengths present. The detectors are typically photodiode detectors or CCD cameras.[21,22] Therefore a full absorption spectrum may be obtained by measuring the intensity distribution with and without a sample. This is possible due to the fixed energy-position correlation present on the detector. The technique has been used since 1981, where the 'multi-edge' possibility of EDE was implicitly recognised by Matsushita and Phizackerley[23] and by Couves *et al.*[24] in 1991. It is only until recently however that a practical application of this unique property has been demonstrated.[25]

2.5.1 Experimental

EDE/MS measurements were made by loading ca. 20 mg of a sample into a quartz tube (ca 3mm id, wall thickness ca. 0.2mm) and held in place using quartz wool plugs, yielding a sample bed of around 5mm in length. The tube was then placed into a microreactor and a 0.5mm mineral insulated thermocouple was inserted directly into the catalyst bed. This allowed the sample to be heated to ca. 673K at $10Kmin^{-1}$. The gases were under mass flow control, the NO and H_2 were set to give 5 $mlmin^{-1}$ each over the sample bed. The actual stoichiometry of the catalytic mixture was ca. 40%NO:60%H_2, with the balance made up with He (therefore around 90% of the gas flow was He). This gave gas hourly space

velocities (GHSV) of ca. 10^4 hr^{-1}. The resultant composition of the products was continuously monitored via a Pfeiffer mass spectrometer equipped with a fused silica capillary to give a constant inlet rate to the mass spectrometer. 16 relevant mass fragments were continuously monitored. A full analysis of the equipment is given below in section 2.7.

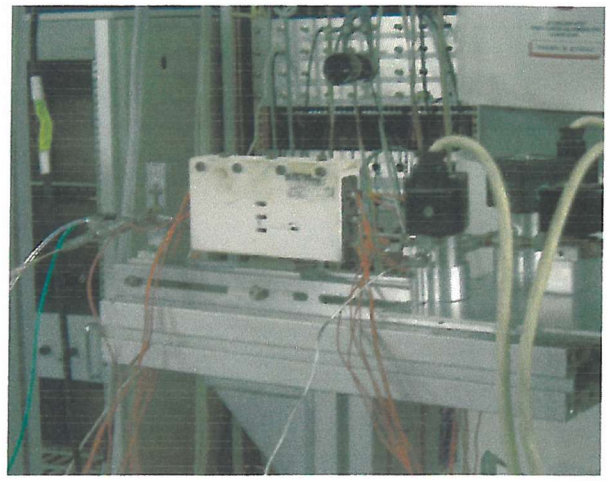

Figure 2.4: Experimental apparatus showing microreactor, including gas valves, quartz tube, and heating equipment

EDE measurements at ID24, Grenoble, France were performed at the Rh K edge using an asymmetrically cut (6°) Si[111] monochromator in Laue (transmission) configuration.[26] This yields a horizontal beam focus on the sample of ca. 70-80 μm and a spread of X-ray energies of ca. 2.5 keV.[27] Detection of the subsequent EXAFS produced was made via a phosphor masked, Peltier cooled, CCD camera (Princeton). The vertical focus was 200-300 μm. The hard (>23 keV) X-ray energies passing through air has been to be an excellent background (I_0) for EDE measurements, while this is only taken at the beginning and end of each experiment to allow continuous monitoring of the sample.

2.5.2 Data analysis

2.5.2.1 Energy Calibration

The 'raw' EXAFS data obtained was calibrated using a foil of the particular *k* edge being looked at, as direct energy calibration is impossible. The procedure for this calibration is shown in the following chapters.

EXAFS data accumulated may be analysed via two stages. Firstly, the actual EXAFS spectra must be separated from the background absorption. This is called background subtraction, and is done via a computer programme by Binsted[28] called PAXAS. Another PC based program called EXCURV98[29] was used to fit the data. The program utilises a spherical wave formalism, which fits the resulting spectrum of $\chi(k)$, the intensity, versus k, the reciprocal space.

2.5.2.2 PAXAS

PAXAS uses subtraction of the pre-edge background to remove the absorption due to the spectrometer. Subtraction of the post-edge background removes the absorption due to all the other elements within the system, for example any anomalous signals stemming from the monochromator. Therefore a poor post-edge subtraction can dominate the EXAFS features, resulting in the distortion of the amplitude of the EXAFS oscillations. This leads to anomalous features at R values less than 1Å in the Fourier transform of the data. It is therefore the role of the background subtraction to minimise the effect of the peaks or features at the lower R value range. This is due in principal by setting a 'window' in R space to include only the 'real' coordination shells present. An iteration procedure is then performed on the variables in the resulting polynomial expression and the next analytical stage is ready to be performed on the resulting data.

2.5.2.3 EXCURV98

EXCURV98, as explained above, utilises a spherical wave formalism which stems from the curved wave theory[30] to fit the data. The programme uses a theoretical model of the EXAFS oscillations, in conjunction with an array of algorithms, to yield structural information. The phenomenon of the ejected photoelectron wave passing through the potential of neighbouring atoms causes phaseshifts, which are calculated by *ab initio* methods.

The calculations essentially model the surrounding environment of the absorbing atom, using the nearest neighbouring atom to build the model. The following describe the major parameters and limits to EXAFS curve fitting.

Structural parameters :

NS – The number of shells for which the model is calculated

N_n – The number of atoms in shell n

T_n – The type of atom in shell n

E_{min} -The minimum energy used to calculate the theoretical spectrum

E_{max} -The maximum energy used to calculate the theoretical spectrum

A_n – The Debye-Waller factor for shell n, given as $2\sigma^2$, where σ is the mean square variation in interatomic distances

E_f - The difference between the calculated Fermi level energy and the known values for the element.

AFAC-The energy independent amplitude factor that accounts for the reduction in amplitude to multiple excitations occurring at the central atom. It is different for each absorbing element, and is obtained from the analysis of model compounds

VPI - The constant imaginary potential which describes the lifetime of the core hole, and accounts for inelastic scattering due to the neighbouring environment

L_{max} –The maximum angular momentum used in theory calculations

The effectiveness of the fit can be measured by discrete values which are regarded as effective parameters and limits.

When a set of parameters is refined within EXCURVE, a minimum In the Fit Index is calculated, principally by adding the differences of the experimental and theoretical data points. Values of the Fit Index should fall between $5x10^{-4}$ and $8x10^{-4}$ to be considered a good fit.

The R-factor is used as an estimation of goodness of fit. It is calculated by the sum of all the errors between all the data points, giving the result against the experimental curve in percentage form. The R-factor should not nominally exceed 30%, but some systems such as dilute systems or the catalysts observed in this study, values of around 45% are acceptable.

Debye-Waller (DW) factors should lie between 0.004 and 0.03, although this can vary, dependent on the sample. Related factors such as DW and coordination values should not be refined together. If the parameters are met during analysis, the accuracy of the first shell coordination distances can be expected to be ± 0.01Å[31] and coordination numbers to fall between ± 10%.[31,32] An example of the results obtained after analysis in EXCURVE is given in figure 5.

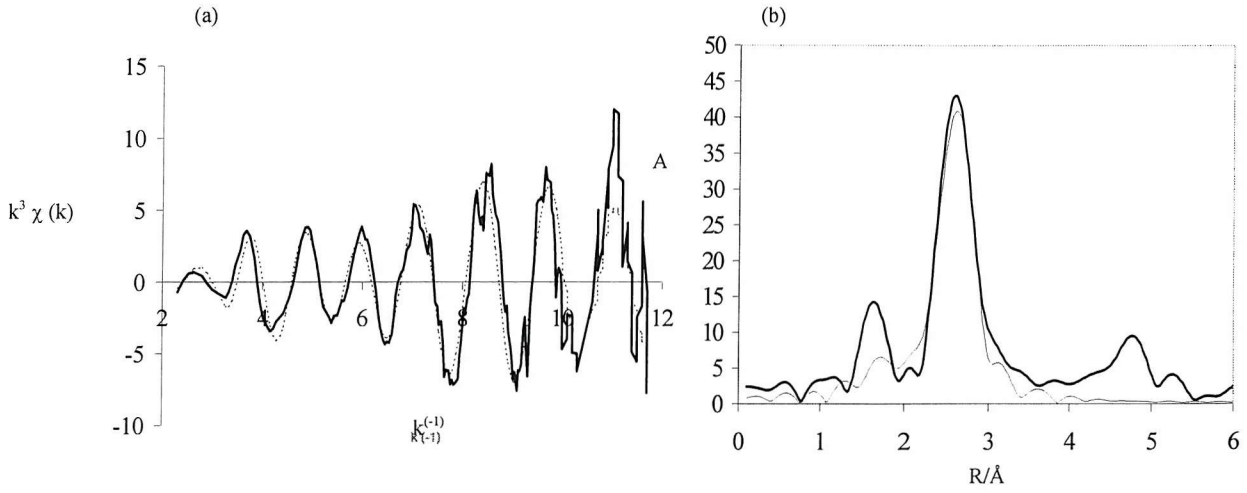

Figure 5: An example of the results obtained after analysis in EXCURVE (a) k^3 weighted EXAFS data, (b) radial distribution curve from Fourier transform of EXAFS, data for (a) and (b) derived from 7.5wt%Rh supported on γ-Al_2O_3 at 673K. Solid lines indicate theoretical fit, dotted lines are experimental values.

2.6 Transmission Electron Microscopy

An electron microscope utilises a focused, narrow beam of high-energy electrons which is directed at a specimen to be analysed. Images of the surface can then be obtained via two techniques. If the sample is thick, secondary emissions from the surface are used, called scanning electron microscopy (SEM). For thin samples, the images are formed by passing electrons through the sample, called transmission electron microscopy (TEM). The maximum obtainable resolution for an image, defined as the closest spacing between two points that can be distinguished through the microscope, is directly proportional to the wavelength of the light impinging on the sample. Electron microscopy therefore has a significant advantage over conventional light microscopy, as a beam of electrons at 100keV has a wavelength of 0.0037nm, compared to around 400nm for a light microscope. Table 2.1 highlights these differences.

Type of microscopy	Resolution (nm)	Magnification	Depth of Field (μm)
Light (λ = 400nm)	150	10^3	<1
Electron (for a 100keV electron beam)	0.2	10^6	10

Table 2.1: Properties of light and electron microscopy

The electron beam used for TEM is generated typically between 100 and 200keV, yielding a resolution of ~0.2nm and a magnification $1x10^6$. TEM therefore can afford both ultrastructural and microstructural information on the specimen surface. The primary electrons that pass through the sample may be transmitted without being deflected, elastically scattered (i.e. diffracted), or inelastically scattered. Images formed in brightfield mode, for example, are the result of variable transmittance across the sample surface. This means that parts of the sample where the electron beam has passed through unhindered will appear white. Where inelastic scattering has occurred, the image appears darker. This phenomenon occurs when the mean atomic number and the thickness of sample increases, known as the mass-thickness contrast. In darkfield mode, for which the samples must be very thin (<95nm), an image is produced by selecting a diffracted beam, and then moving the detector

off the axis of the incoming electrons. The images are viewed on a scintillation screen via magnification by electromagnetic projector lenses.

All TEM images used in this study were obtained on a JEOL FX 2000 transmission electron microscope, equipped with a Tracor 5400 system, set in brightfield mode. The samples were prepared by crushing ca 10^{-4}g of catalyst into a fine powder. 2ml of distilled water is then added slowly to the mortar and then ground further until a fine suspension is obtained. This mixture is then transferred to a sample vial and placed in an ultrasonic bath for at least 10mins. A small drop of the suspension is taken from the very top of the vial and is then placed onto a TEM copper disc with a fine carbon grid. The discs are then left to dry for 48 hours in a vacuum desiccator. Figure 2.6 shows an example of a TEM image in brightfield mode, the image has been 'locally equalised' to show the particles present on the surface.

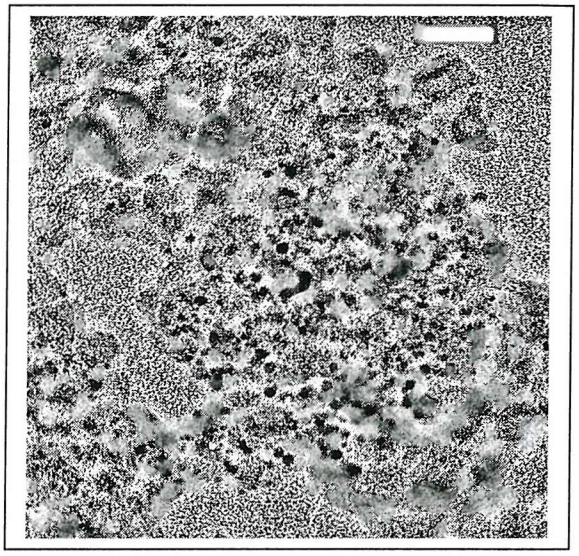

Figure 2.6: A TEM image of 5wt%Rh supported on γ-Al_2O_3, the dark areas show the Rh particles. The scale bar represents 20nm.

2.7 Temperature Programmed Plug Flow Microreactor Studies.

The microreactor apparatus used in this study is designed to allow the *in situ* characterisation of the catalyst samples by Energy Dispersive EXAFS. As explained above, the material is required to be held in a configuration that allows the transmission of the X-rays through the sample. This is achieved in this case via the use of a quartz tube as the

sample holder. Figure 2.7 shows a schematic of the major components of the microreactor utilised in this study.

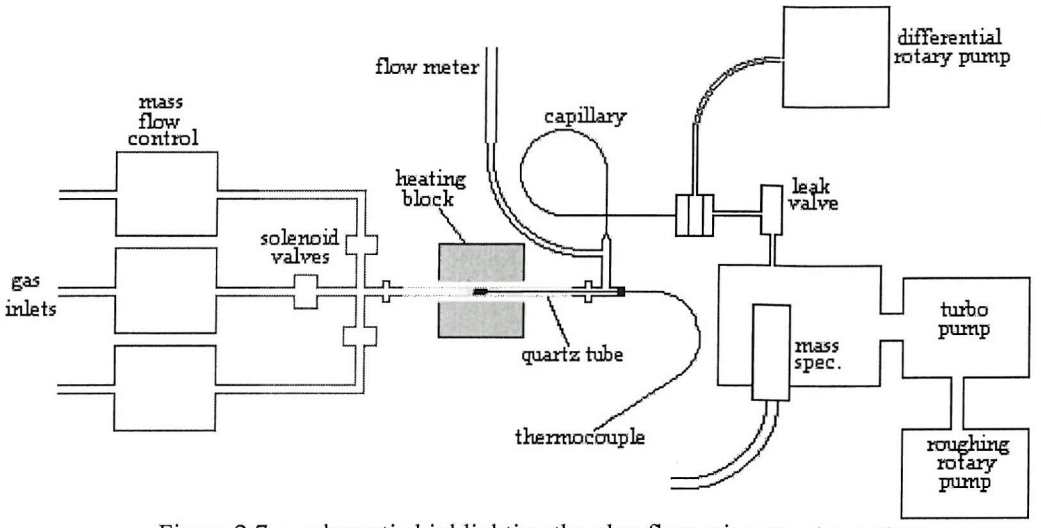

Figure 2.7: a schematic highlighting the plug flow microreactor system

This configuration allows up to three different gases/gas mixtures to flow through the system, the flow rate of the gas controlled by UNIT 7300 mass flow controllers. The selection or mixing of the gases before they enter the catalyst bed is done via a set of solenoid valves.

A typical experimental set up includes a catalyst charge, ~20mg, loaded into a pre-marked position in a ca 200mm long quartz tube (ca. 3mm id, wall thickness ca. 0.2mm). The packed sample is held in place by quartz wool plugs, yielding a sample bed length of around 5mm. The tubes are equipped with push on fittings, one end is attached to the outlet from the solenoid valves, and a 0.5mm mineral insulated thermocouple is directly inserted into the sample bed at the other end. A proportion of the gas effluent that does not pass through the flow meter may be 'tapped' into the UHV chamber via the steel capillary and leak valve. The reaction gas composition can then be analysed with the incorporated mass spectrometer.

The mass spectrometer used in this study was a Pfeiffer vacuum Omnistar mass spectrometer. Resulting ions can be detected in two ways: by the Faraday plate or an electron multiplier. Due to its sensitivity, the electron multiplier detector was used in all the EDE experiments. The dynodic strip, which forms the basis of this detector, has a typical potential drop of 2kV across it. Bombarding the cathode with ions from the analyser results in the emission of electrons. These resulting electrons are directed, by a magnetic field, back towards the dynodic strip in a cyclic path. The resulting current is increased as each impinging electron results in the emission of several more electrons. This process is then repeated at set stages along the strip towards the anode, greatly amplifying the signal.

Figure 2.8 shows the microreactor apparatus, and the heating system can also be viewed here. Up to twelve 75W cartridge heaters are inserted into a two-piece brass block, which accommodates the quartz tube. For optimal temperature stability and attainment, a ceramic hood is utilised. A Eurotherm 902 series temperature controller controls the power output, and effectively the correct heating rate, to the cartridge heaters.

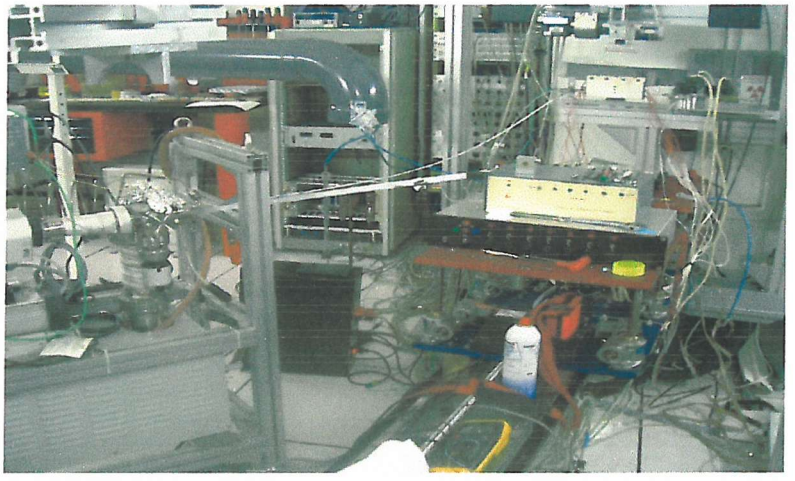

Figure 2.8: microreactor apparatus showing mass spectrometer, and heating equipment

2.8 Isothermal Nitrogen Adsorption Analysis

The phenomena of nitrogen adsorption on an oxide surface can be observed to occur in two stages. At low pressures of the adsorbate, an initial monolayer is formed. The second stage is observed upon further adsorption at higher pressures where multilayers of the substrate are formed. The isotherm that is utilised for these processes is known as the BET isotherm, created by Brunauer, Emmett and Teller in 1938,[34] and is utilised to determine the total surface area of the oxide support in this study:

$$\frac{V}{V_{mon}} = \frac{cz}{(1-z)\{1-(1-c)z\}} \qquad \text{where } z = \frac{p}{p^*} \qquad \text{Eq. 2.12}$$

Equation 12 highlights p^* as the vapour pressure above a layer of nitrogen that is more than one molecule thick, essentially thought of as a pure bulk liquid. V_{mon} is the volume of the monolayer, and c is a constant which corresponds to the following expression:

$$c \approx e^{(\Delta_{des}H^\circ - \Delta_{vap}H^\circ)/RT} \qquad \text{Eq. 2.13}$$

when this coefficient is large (c>>1), the isotherm simplifies to the following expression:

$$\frac{V}{V_{mon}} = \frac{1}{1-z} \qquad \text{Eq. 2.14}$$

Equation 2.14 is therefore most applicable to the systems used in this study, as $\Delta_{des}H^\circ$ is essentially much greater than $\Delta_{vap}H^\circ$. From this, the calculated volume can be related to the number of moles of gas adsorbed, and hence the surface area in m^2. A value of m^2g^{-1} can be found if the mass of material is known. BET data can therefore yield information on the physical properties of the catalysts in question, such as total surface area, porosity and poresize distributions. BET measurements were made using a Quantachrome Nova 3000 series BET machine.

2.9 Synthesis and Pre-treatment of Catalysts.

The following catalysts were made with varying metal loading. The support used was γAl_2O_3 (aluminium oxide c from Degussa):

- 10%Rh, 7.5%Rh, 5%Rh; 2.5%Rh, 1%Rh.
- 10%Pd, 5%Pd, 2.5%Pd, 1%Pd.
- 4.5%Rh:0.5%Pd, 4%Rh:1%Pd, 3%Rh:2%Pd, 2%Rh:3%Pd, 1%Rh:4%Pd.

A physical mixture was also made, comprising of equal amounts of 5wt%Rh and 5wt%Pd.
A 'chlorinated' and 'chlorine-free' set of samples was made for each of the permutations. This was due to the investigation into the role of chlorine in the catalytic systems. Existing theories include chlorine simply covering the catalyst surface, or by effectively increasing the metal particle size. The corresponding precursors for each set were as follows:

(a) $RhCl_3.3H_2O$ and $PdCl_2$ for chlorinated set, denoted RhCl systems

(b) $Pd(CH_3CO_2)_2$ and $Rh(NO_3)_3$ for chlorine-free set, denoted RhN systems.

2.9.1 Method

The precursors were weighed out according to the amount of support used (2g) and dissolved in ~5ml of distilled water. The $PdCl_2$ was dissolved in acidified water (pH 1.5).
The alumina was placed into a beaker with a magnetic stirrer and the two solutions were added simultaneously and stirred until a homogeneous substance was obtained. The co-impregnated (CI) sample was then dried overnight. The samples were sieved to a 90μm fraction.
Each of the samples was split, 1g to be calcined/reduced and 1g to be calcined, for future in-situ reduction experiments.
Reduction conditions: Under a 60:40 mix of H_2:He ($20mlmin^{-1}$) at 573K for 6 hours.
Calcination conditions: Under flowing O_2 ($20mlmin^{-1}$) at 673K for 5 hours.
Each sample was purged under the gas for 1 hour and cooled under the gas before being transferred to sealed sample jars. No attempt was made to stop the samples being exposed to air.

Due to an apparent synergism effect on the alloy samples, discussed in a following chapter, a stepwise impregnation (SI) technique was carried out on the following alloy samples:

- 4%Rh:1%Pd, 3%Rh:2%Pd, 2%Rh:3%Pd, 1%Rh:4%Pd.

These were made as chlorinated samples only, using the same aqueous phase dilution.
After drying overnight, the first supported noble metal, Rh, was calcined at 573K for 2 hours. Following the final impregnation of Pd the dried sample was calcined at 673K for 5 hours, and then reduced under a 60:40 mix of H_2:He ($20mlmin^{-1}$) at 573K for 6 hours.

2.10 References

(1) D.P. Woodruff, T.A. Delcher, 'Modern techniques of surface science', 1989, Cambridge University Press.

(2) M. Harada, K. Asakura, Y. Ueki, N. Toshima, *J. Phys. Chem. B.*, 1993, **97**, 10742.

(3) A.I Frenkel, C.W. Hills, R.G. Nuzzo, *J. Phys. Chem. B.*, 2001, **121**, 16.

(4) J.C. Riviére, 'Surface analytical techniques', 1990, Clarendon Press.

(5) G. Beamson, D. Briggs, 'High resolution XPS of organic molecules- the Scienta ESCA 3000 data book, 1992, John Wiley and Sons, Cambridge.

(6) D.E. Sayers, E.A. Stern, F.W. Lytle, *Phys. Rev. Lett.*, 1971, **27**, 1204.

(7) E.A. Stern, *Phys. Rev. Lett. B.*, 1974, **10**, 3027.

(8) R.G. Greenler, R.R. Rahn, J.P. Shwartz, *J. Catal.*, 1971, **23**, 42.

(9) F.W. Lytle, D.E. Sayers, E.A. Stern, *Phys. Rev. Lett. B.*, 1975, **11**, 4825.

(10) E.A. Stern, D.E. Sayers, F.W. Lytle, *Phys. Rev. Lett. B.*, 1975, **11**, 4836.

(11) E.A. Stern, 'Theory of EXAFS: principles, applications and techniques of EXAFS, SEXAFS and XANES, 1988, John Wiley and Sons.

(12) G. Lu, M. Chen, L. Ma, *Acta. Chimica. Sinica.*, 1989, **47**, 37.

(13) N.A. Cruise, J. Evans, *J. Chem. Soc. Dalton Trans.*, 1995, 3089.

(14) J. Evans, *Chem. Industry*, 1995, 135.

(15) G. Sankar, P.A. Wright, S. Natarajan, J.M. Thomas, G.N. Greaves, A.J. Dent, B.R. Dobson, C.A. Ramsdale, R.H. Jones, *J. Phys. Chem.*, 1993, **97**, 9550.

(16) B.S. Clausen, L. Grabaek, G. Stefferson, P.L. Hanson, H. Topsoe, *Catal. Lett.*, 1993, **20**, 23.

(17) R.B. Gregor, F.W. Lytle, *J. Catal.*, 1980, **63**, 476.

(18) S.J Gurman, *J. Phys. C.*, 1983, **16**, 2987.

(19) M. Hagelstein, C. Ferrero, U. Hatje, T. Ressler, W. Metz, *J. Synchrotron Rad.*, 1995, **2**, 174.

(20) M. Hagelstein, C. Ferrero, M. Sanchez del Rio, U. Hatje, T. Ressler, W. Metz, *Physica B.*, 1995, **208**, 223.

(21) T. Ressler, M. Hagelstein, U. Hatje, W. Metz, *J. Phys. Chem.*, 1997, **101**,

6680.

(22) G.E. Derbyshire, W.I. Helsby, A.J. Dent, S.A. Wright, R.C. Farrow, G.N. Greaves, C. Morrell, G.I. Baker, *Daresbury Laboratory technical Memorandum,* DL/SCI/P723E.

(23) T. Matsushita, R.P. Phizackerley, *Jpn. J. Appl. Phys.*, 1981, **20**, 2223.

(24) J.W. Couves, J.M. Thomas, D. Waller, R.H. Jones, A.J. Dent, G.E. Derbyshire, G.N. Greaves, *Nature*, 1991, **354**, 465.

(25) S.G. Fiddy, M.A. Newton, T. Campbell, J.M. Corker, A.J. Dent, I. Harvey, G. Salvini, S. Turin, J. Evans, *Chem. Commun.*, 2001, 445.

(26) M. Hagelstein, C. Ferraro, U. Hatje, T. Ressler, W. Metz, *J. Synchrotron Radiat.*, 1998, **5**, 1396.

(27) M.A. Newton, A.J. Dent, J. Evans, *J. Chem. Soc. Rev.*, 2002, **31**, 83.

(28) N. Binsted, PAXAS: Program for the analysis of X-ray adsorption spectra, University of Southampton, 1988.

(29) N. Binstead, EXCURV98, CCLLRC Daresbury Laboratory computer program, 1998.

(30) S.J. Gurman, *J. Phys. C.*, 1988, **21**, 3699.

(31) J.M. Corker, J. Evans, H. Leach, W. Levason, *Chem. Commun.*, 1989, 181.

(32) B.K. Teo, 'EXAFS: Basic principles and data analysis', 1986, Springer Verlag, Berlin.

(33) S.J. Gurman, in 'Applications of Synchrotron radiation', 1989, Blackies, Glasgow.

(34) D. Dollimore, G.R. Heal, *J. Appl. Chem.*, 1964, 101.

(35) D. Burnaby, PhD Thesis, University of Southampton, 2000.

Chapter 3

Rhodium Only Systems

3.1 Introduction

The role of rhodium as a primary component in catalytic systems such as the three-way automotive exhaust catalyst has always been of scientific interest due to its ability to catalyse the selective reduction of NO_x species to N_2.[1] By using an array of complementary techniques such as EDEXAFS, TEM, XPS and mass spectrometry this chapter aims to probe the dynamic relationships that exist between the structure of a range of supported Rh catalysts and their capacity to selectively catalyse the reduction of NO by H_2.

3.2 Determination of Debye-Waller factors in variable temperature EDEXAFS studies

As mentioned in the experimental chapter, the inherent relationship between static and dynamic disorder (as analytically accounted for by using DW factors) and coordination numbers in EXAFS means that for the restoration of accurate coordination numbers to be undertaken correct estimates of the DW factors need to be made. This is particularly true in variable temperature studies of the type undertaken here. Figure 3.1 illustrates this for typical foil spectra taken at 298K and 673K, the raw EXAFS highlighting the effect of temperature.

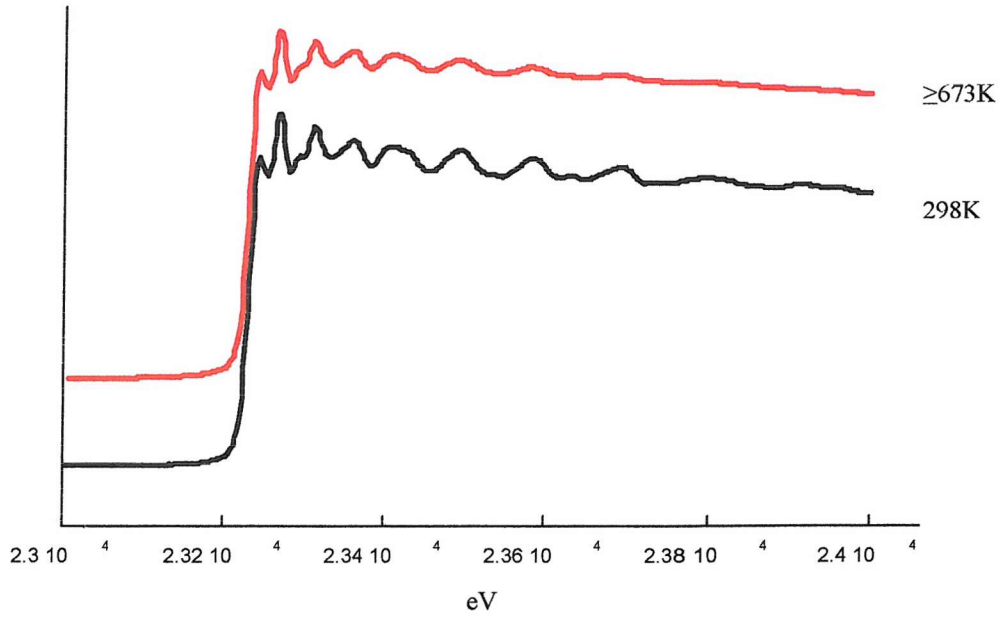

Figure 3.1: EXAFS signature showing a Rh foil at the temperatures indicated. A difference in EXAFS intensity is observed with increasing temperature.

As the FCC structure of the foil remains invariant between these two cases, the apparent difference in EXAFS signal with increasing temperature therefore cannot be due to differences in coordination number. If these or any spectra with a variance in temperature were to be analysed with the same DW factors, a severe underestimation of the occupation of the Rh shells for spectra at high temperatures would result. As such a method of correctly determining the DW factors as the temperature is increased is needed for the accurate analysis of spectra.

As this study deals with nanoparticulate systems, containing a range of particle sizes, the use of a foil is not necessarily the most effective method to determine the DW factors. This is principally because it cannot be assumed that the static and dynamic components of the DW factors, and their variation with temperature will be the same in the nanoparticulate case as in the bulk foil.

In an attempt to address this problem, a 5wt% Rh sample was re-reduced *in situ* in a gas flow to 673K. EDE measurements were then performed on the sample as it cooled. This procedure assumes that no changes occur in both metal particle size distribution or morphology when the sample is in the cooling cycle from 673K, meaning changes in EXAFS are only attributed to changes in sample temperature. The resulting spectra were analysed and refined for the first shell metal co-ordination number (N_1^{metal}), metal-metal bond length and Fermi level (E_f) values. The spectra were analysed over a constant spectral width (Δk=2-13 $Å^{-1}$), holding the DW factor constant. At each temperature a range of DW factors (0.004-0.036) was analysed and the R factors determined. The minimum in the subsequent plot of R factor versus DW factor yielded the correct DW factor for the given temperature. This method can be effectively visualised in figure 3.2, which shows the DW factors obtained via the minima of the subsequent R factor at a given temperature. The figure also highlights the inherent errors involved in determining DW factors, as the minima in the R versus DW curves are broad. Hence the accuracy of the DW factors actually used has an error of ± 10% involved, giving the potential for error in subsequent coordination numbers as 10-20%. The subsequent extrapolation of this line gave the correct DW factors for use in analysing the EXAFS data, shown in figure 3.3.

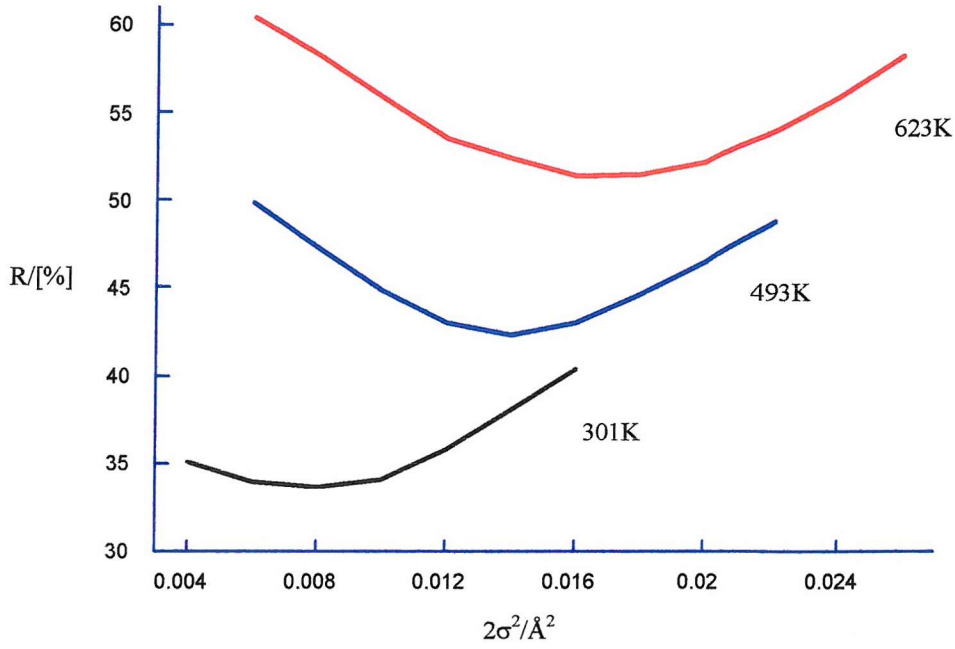

Figure 3.2: Plot of R factor versus DW factor highlighting the method used for correct DW factor determination.

The corresponding N_1^{Rh} values obtained at each R factor minimum is as follows: 301K N_1^{Rh}= 3.2; 493K N_1^{Rh}=7.2; 623K N_1^{Rh}=7.8.

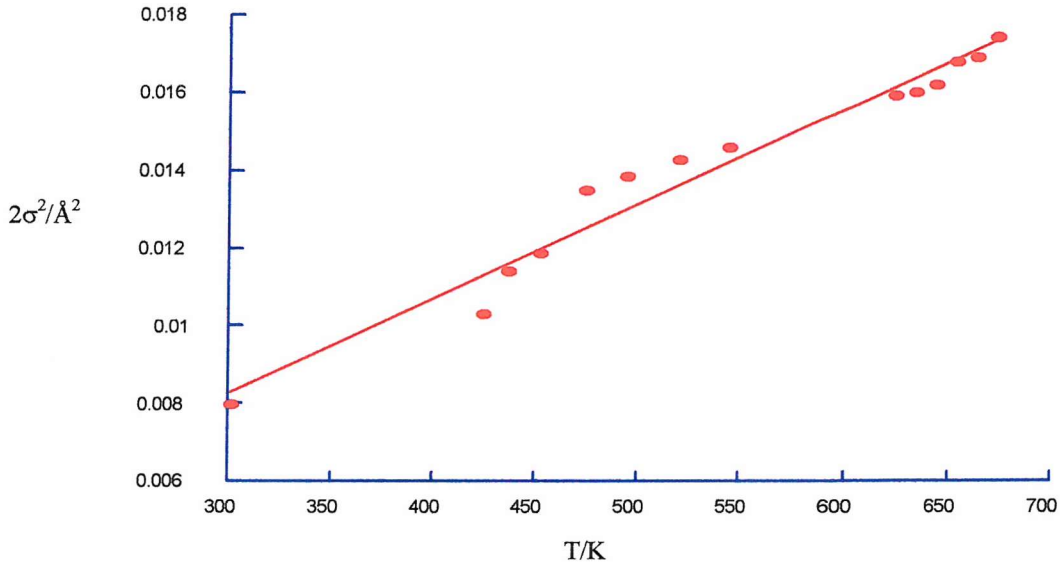

Figure 3.3: Plot of derived DW factor as a function of temperature, showing raw data and statistical fit.

3.3 Energy Dispersive EXAFS Study of Rh Supported Nanoparticles on γ-Al_2O_3

The Rh K-edge EDE spectrum for a Rh foil is shown in figure 3.4. The bond lengths obtained for Rh metal by X-ray crystallography[1] are also shown in table 3.1. The figure highlights that the energetic calibration performed is correct and the bond lengths obtained are reasonable, as the results correlate well to the crystallographic data shown. The calibration factor is very important in EDE as the use of a bent monochromator, as opposed to a conventional double crystal monochromator, makes direct energy calibration impossible. Therefore the raw data is collected as a function of pixel number and then converted for use in analysis.

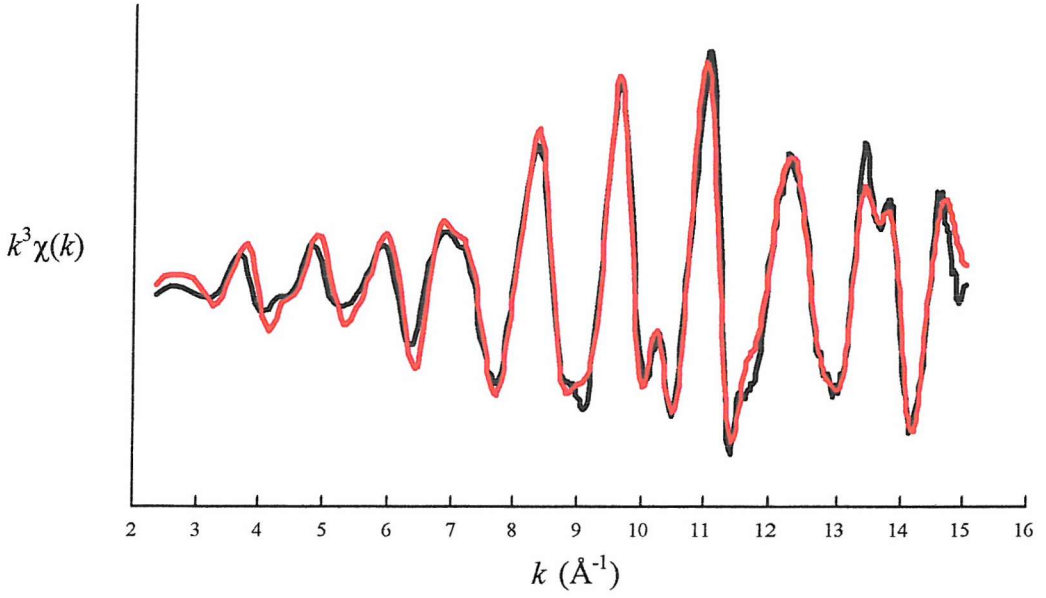

Figure 3.4: Rh *k*-Edge EXAFS spectra for Rhodium foil. The red line indicates a theoretical fit; the black line shows the experimental data.

Rh shell	k_{min} (Å^{-1})	k_{max} (Å^{-1})	Shell	CN	*r/Å*	$2\sigma^2$/Å^2	X-Ray bond length/Å
(N_1)	2	15	Rh	12	2.683	0.009	2.69
(N_2)	2	15	Rh	6	3.808	0.012	3.8
(N_3)	2	15	Rh	24	4.664	0.012	4.66
(N_4)	2	15	Rh	12	5.38	0.018	5.38
(N_5)	2	15	Rh	24	6.029	0.012	6.01

Table 3.1: Elemental coordination (N_x^s), bond length (R), and statistical parameters derived from explicit analysis of EDE spectra*. Ef= -2.48, R= 20.66. The coordination number remains fixed, r, DW and Ef factors are refined. This format is applicable for all the subsequent data tables.

* Errors in bond length determination are estimated to be ca. 2%.

Figure 3.5 shows k^3-weighted Rh K edge EDE spectra for the various catalytic systems investigated in this study, all exposed to air at room temperature. The data for these 'fresh' systems clearly indicates the presence of an oxidic Rh phase in all of the systems, not of metallic Rh as might be expected from the reduction step used in their synthesis. Even at relatively high metal loading, i.e. 10wt% Rh, a predominant oxidic signature is present, highlighted by the low elemental coordination number given in table 3.2, which also shows the data for the other RhCl systems. This effect can also be observed in figure 3.5, which shows the corresponding N_1-Rh values for the 'fresh' systems, clearly indicating an oxidic Rh phase present. Only the 10wt% system exhibits a slight metallic Rh signature via an increase in its N_1-Rh value, however the increase is not significant and the phase of Rh can still be assigned to be predominantly oxidic. The data obtained from the 2.5wt% RhCl system was not amenable to analysis due to a poor signal/noise ratio, highlighted in the figure. The data obtained over a short *k* range does however show that a similar character exists with the 2.5wt% system when compared to the other systems.

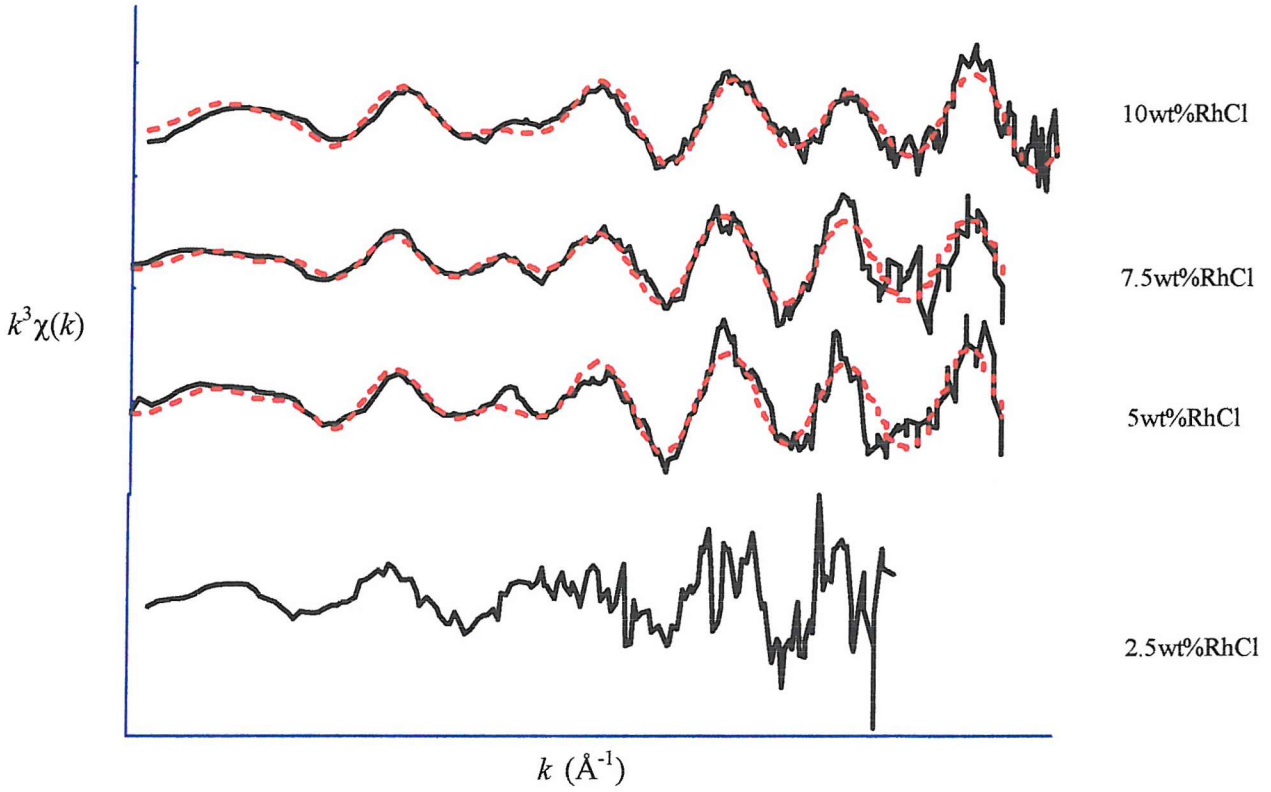

Figure 3.5: k^3-weighted EDE spectra of the 'fresh' RhCl systems. Solid lines show actual spectra and dotted lines show theoretical spectra (format for all subsequent spectra).

Sample	Scatterer (s)	k_{min} (Å^{-1})	k_{max} (Å^{-1})	CN	*r*/Å	$2\sigma^2$/Å^2	E_F	R (%)
10wt% RhCl	O	2	12	2.72	2.002	0.005	-2.92	42
	Rh	2	12	4.1	2.658	0.008		
7.5wt% RhCl	O	2	12	2.3	1.989	0.005	-4.4	32
	Rh	2	12	3.9	2.663	0.010		
5wt% RhCl	O	2	12	2.4	2.01	0.005	-2.3	46
	Rh	2	12	3.8	2.664	0.009		

Table 3.2: Data derived from analysis of EDE spectra in figure 5. Errors in coordination for the oxidic spectra should be regarded as between 15-20%

Figure 3.6 shows the EXAFS obtained for the catalytic systems under a 40:60 mix of NO/H_2 at 10mlmin^{-1}, after a room temperature reduction by H_2. The figure highlights the state of the catalysts prior to the *in situ* experiment and the apparent room temperature oxidation of the Rh is observed again. The k^3-weighted data also establishes the data quality obtained from the experiment.

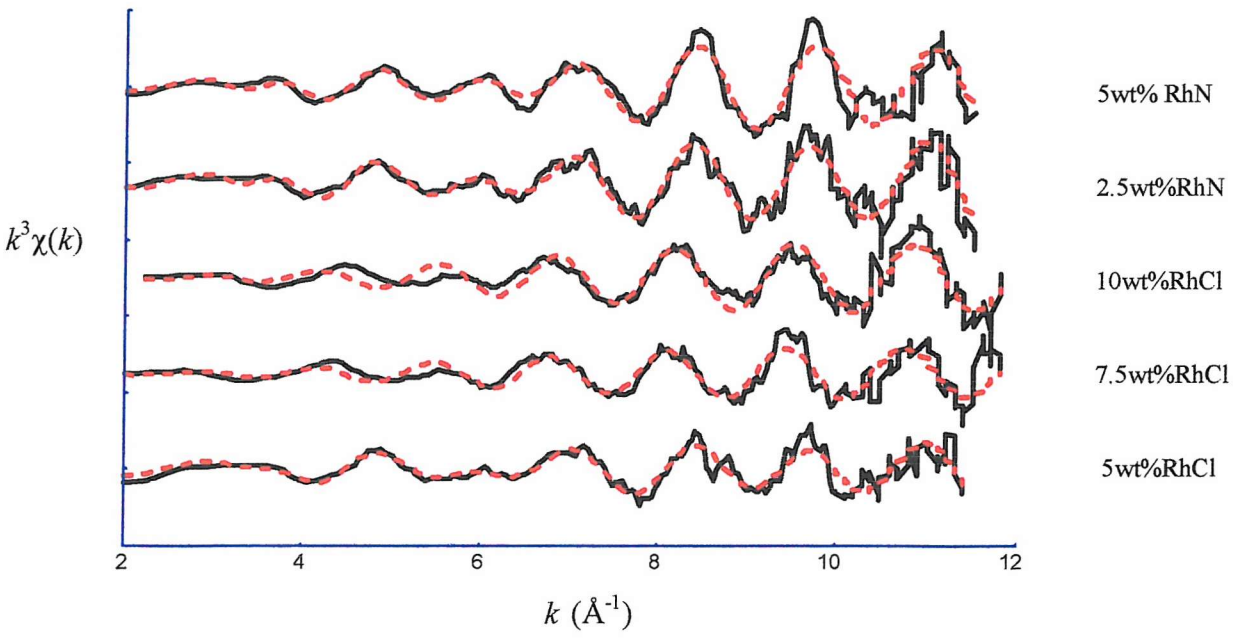

Figure 3.6: k^3-weighted EDE spectra of the RhCl and RhN systems under a 60:40 mix of NO/H_2.

Spectrum	Scatterer (s)	k_{min} (Å^{-1})	k_{max} (Å^{-1})	CN	*r*/Å	$2\sigma^2$/Å^2	E_F	R (%)
5wt% RhN	O	2	12	1.3	2.08	0.005	-4.5	45
	Rh	2	12	4.6	2.66	0.009		
2.5wt% RhN	O	2	12	1.9	2.04	0.005	-2.7	47
	Rh	2	12	3.9	2.68	0.009		
10wt% RhCl	O	2	12	2.3	2.01	0.005	-1.6	42
	Rh	2	12	5.2	2.68	0.008		
7.5wt% RhCl	O	2	12	2.0	2.03	0.005	-2.6	45
	Rh	2	12	4.5	2.67	0.009		
5wt% RhCl	O	2	12	1.8	2.01	0.005	-4.7	51
	Rh	2	12	2.7	2.67	0.009		

Table 3: Data derived from analysis of EDE spectra in figure 6.

The EDE signatures for the 7.5wt%, 10wt% RhCl and the RhN systems show the systems not to be as extensively oxidised compared to their 'fresh' state previously observed, the reasons for this are discussed below.

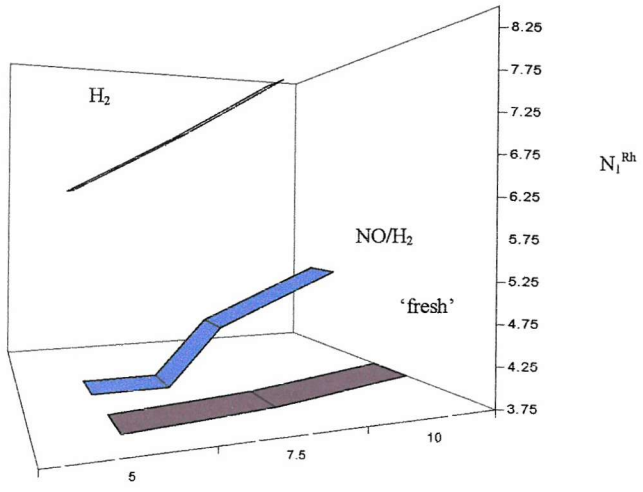

Figure 3.7: N_1-Rh data for 'fresh', under H_2 and under 60:40 NO/H_2 catalytic mixture, RhCl systems. An apparent increasing coordination number with increasing metal loading is present, this effect being significant after exposure to NO/H_2.

A linear relationship is observed with the data obtained from the systems exposed to H_2, shown in figure 3.7. The room temperature reduction by H_2 of the Rh component yields a metallic Rh phase whose average particle size increases with metal loading. Figure 3.7 also shows the coordination data for the RhCl systems after exposure to a 60:40 H_2:NO mix of gases, which shows a significant linear relationship between N_1^{Rh} value and metal loading. A differential in re-oxidation of the Rh is observed, this effect being most marked for the lower loaded systems.

Figure 3.8 shows examples of the Fourier transforms for selected systems, each indicating the presence of an oxygen shell before the Rh shell at ca. 2.67Å.

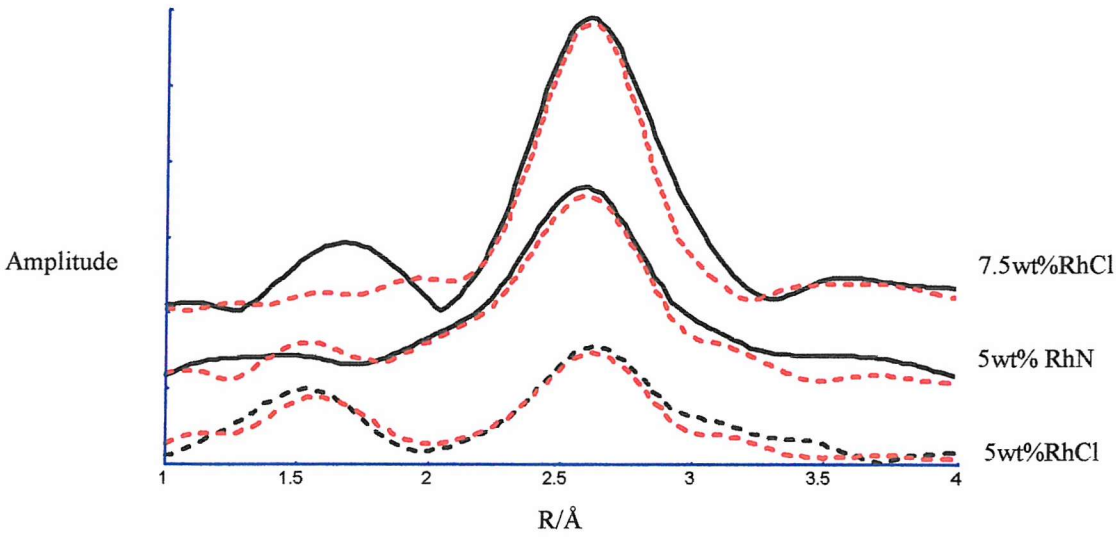

Figure 3.8: Selected Fourier transforms of systems under NO/H_2 reaction mixture, indicating the oxygen shell.

Figure 3.9 shows representative k^3-weighted EDE spectra derived during the reaction of the 5wt%Rh catalyst at the temperatures indicated. The system is an effective example in highlighting the dynamic processes that occur over the Rh systems during the temperature controlled reaction. Table 3.4 shows the physical data associated with the spectra for the system, which includes the errors involved in analysing the data obtained from the catalyst.

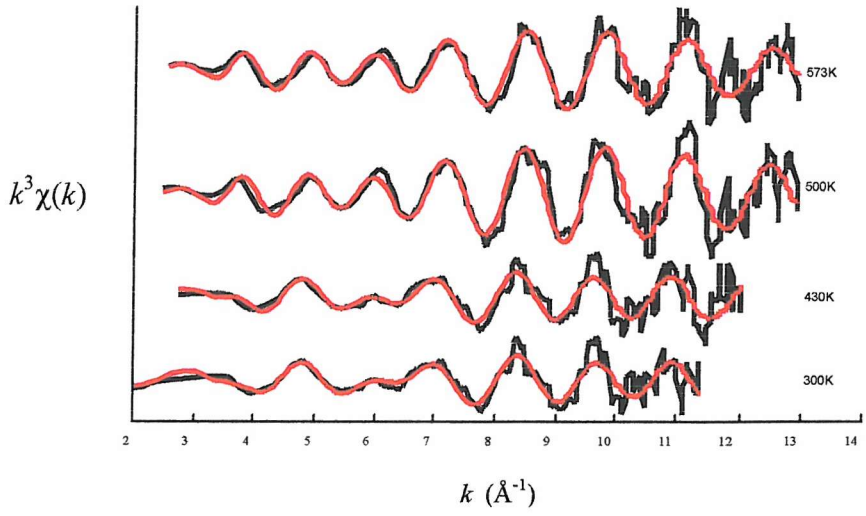

Figure 3.9: Representative k^3-weighted EDE spectra obtained during the NO/H_2 catalytic reaction over 5wt% RhCl system at the temperatures indicated.

Sample	T/K	Scatterer (s)	k_{min} (Å^{-1})	k_{max} (Å^{-1})	CN	*r*/Å	$2\sigma^2$/Å^2	E_F	R (%)
5wt% RhCl	303	O	2	12	2.3	2.07	0.005	-6.0	59
		Rh	2	12	2.9	2.68	0.010		
	423	O	2	12	2.0	2.05	0.005	-6.4	59
		Rh	2	12	3.7	2.69	0.012		
	493	Rh	2	12	7.9	2.65	0.013	-11.0	46
	573	Rh	2	12	7.6	2.64	0.016	-10.0	50

Table 3.4: Data derived from analysis of EDE spectra in figure 9.Errors pertaining to metallic Rh systems are ca. 10-15%.

The k^3-weighted data here serves the purpose of establishing the data quality of individual spectra obtained during the catalytic experiment, which is inherent to the analysis of spectra at differing temperatures.

Figure 3.10 shows the Rh coordination number data for the various systems obtained in the temperature controlled in situ experiment, with a 10% (40:60) mix of NO/H_2/in 90% He as the reaction feedstock, over the temperature range of ca. 300K to 600K. The figure highlights the initial coordination number to be $N_1^{Rh} \approx 4$, irrespective of metal loading. A slight increase in initial coordination number between the 5wt%Rh and 10wt%Rh can be observed, for example N_1^{Rh}=3.6 and N_1^{Rh}=4.5 at 338K respectively, but the increase is within error limits and cannot be viewed as significant.

By ca. 425K the Rh phase appears to be oxidised even further, and this is also seen in the reduction of high *k* EXAFS intensity in the data obtained for these systems. In the region 470K the Rh phase rapidly changes to a metallic state with N_1^{Rh} of about 8. The collapse of the oxidic Rh phase is observed in the same temperature region for all of the metal loadings.

An apparent increase of coordination number with increasing metal loading is observed again in the metallic Rh phase, 5wt%Rh N_1^{Rh} being 7.5 and 10wt%Rh being 8.1 at 518K, the difference present but not statistically significant. The metallic coordination data obtained from the 2.5wt%Rh system shows a marked difference between the similar 5-10wt%Rh systems, with a maximum N_1^{Rh} of about 6. This indicates a possible metal loading limit to which any difference in EXAFS data can be observed.

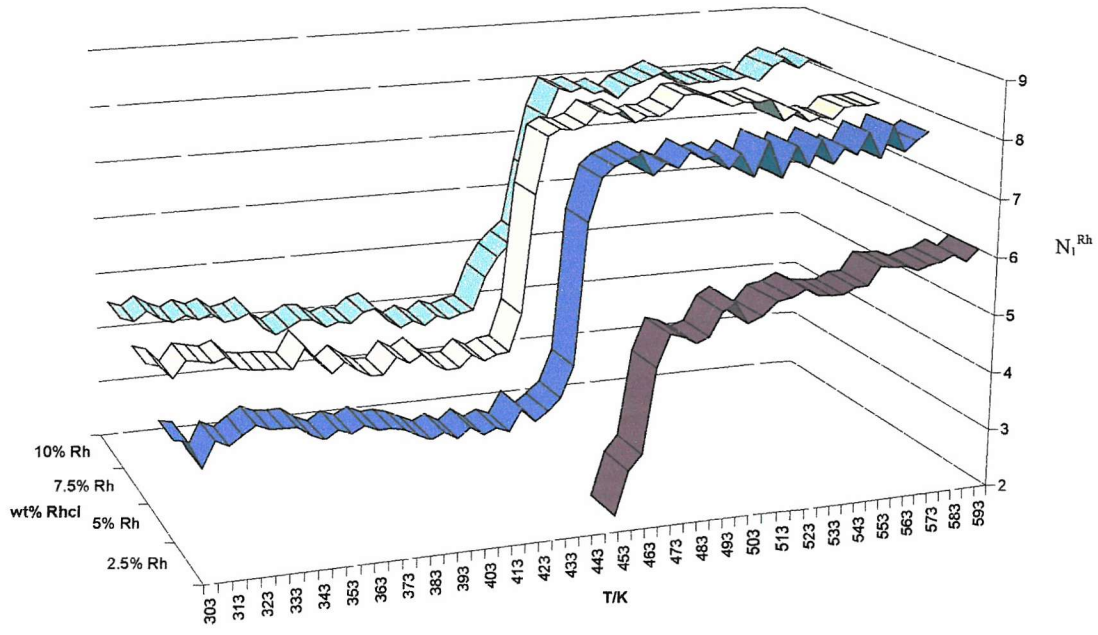

Figure 3.10: Coordination data for the Rh systems over the temperature range 300K to 600K

The bond length (r) data acquired for the Rh systems highlights the apparent low temperature oxidic Rh phase, the effective Rh-Rh bond distance being ca. 2.67Å. After the light off region and the subsequent collapse into the metallic phase at ca. 470K the Rh-Rh bond distances decrease to a value of ca. 2.65Å. Differences are again observed in the 10wt% system compared to the lower wt% systems, the higher loaded catalyst having an apparent higher Rh-Rh bond length, but again the difference of ca. 0.02Å is not significant. Although there is a significant difference between the 2.5wt% and the higher loaded systems in terms of N_1^{Rh}, there is no considerable difference between the r values obtained from the system.

Figure 3.11 shows representative k^3-weighted EDE spectra derived during the reaction of the 5wt%RhN catalyst at the temperatures indicated, and table 3.5 shows the data associated with the spectra. The figure highlights the reduced levels of Rh oxidation of the Rh particles present in the chlorine free systems, as does the Fourier transform at room temperature for the system shown in figure 3.8. The differences between the RhCl and RhN systems before light off temperatures can be compared directly by the EXAFS data show in figures 3.9 and 3.11.

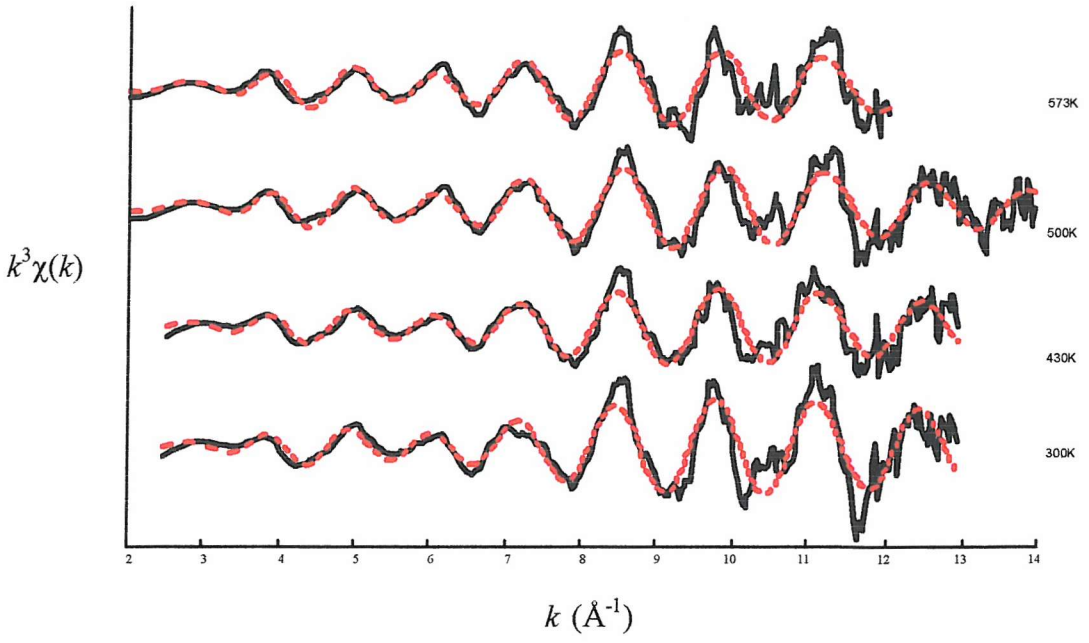

Figure 3.11: Representative k^3-weighted EDE spectra obtained during the 60:40 NO/H_2 catalytic reaction over 5wt% RhN system at the temperatures indicated.

Sample	T/K	Scatterer (s)	k_{min} (Å^{-1})	k_{max} (Å^{-1})	CN	*r*/Å	$2\sigma^2$/Å^2	E_F	R (%)
5wt% RhN	323	Rh	2	13	5.9	2.66	0.010	1.0	53
	423	Rh	2	13	5.7	2.65	0.012	1.4	48
	493	Rh	2	14	7.4	2.64	0.014	-6.9	50
	573	Rh	2	12	7.6	2.65	0.016	-8.4	51

Table 3.5: Data derived from analysis of EDE spectra in figure 3.11.

The EDE experiments performed on the Rh systems made with chloride precursors were also performed on 2.5wt% and 5wt% systems prepared with nitrate precursors, to observe any potential differences between the systems. Figure 3.12 shows the coordination data for the Rh nitrate (RhN) systems across the temperature range, and compares this data with the analogous chloride systems.

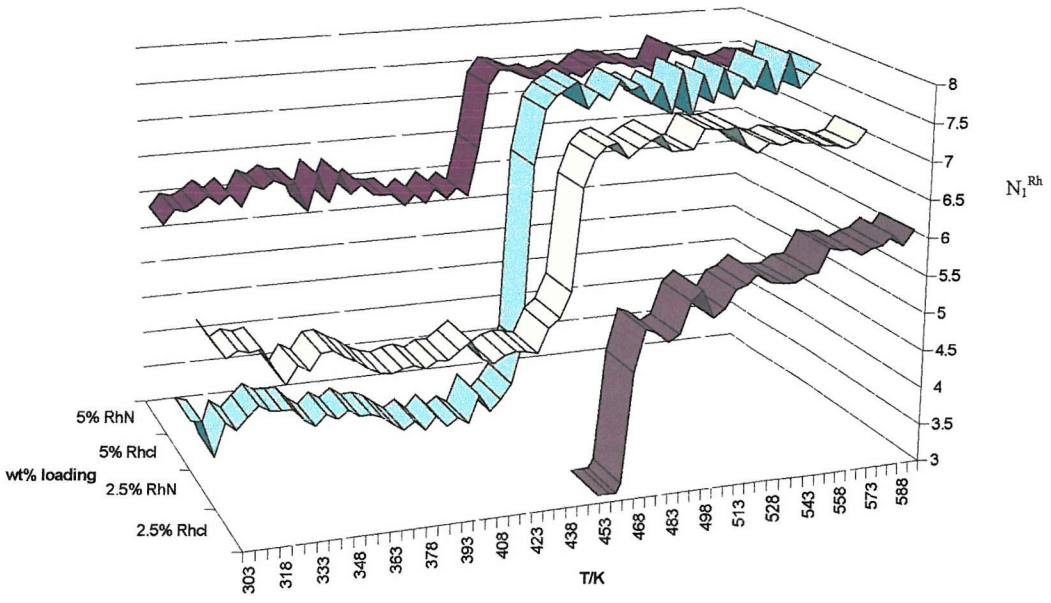

Figure 3.12: Comparison of coordination data from Rh systems using chloride and nitrate precursors.

It is evident from figures 3.11 and 3.12 that the RhN systems are structurally different to the RhCl systems. The most noticeable difference is that the RhN systems are not as extensively oxidised at lower temperatures than the RhCl analogues, for example in the 5wt% case at 308K the RhCl N_1^{Rh} value is 3.5, whereas the RhN N_1^{Rh} value is 6.0. A similar trend is observed in the 2.5wt% case, with the N_1^{Rh} value before the light off region nominally being around 4.5. This system is also markedly different after the light off region, where the coordination number rises to a value of around 7 compared to around 6 for the RhCl system. These results show that the use of a non-chlorinated precursor to support Rh on the surface of the alumina has a considerable impact on the physical state of the catalyst, to the effect that low temperature oxidation significantly curtailed compared to chlorinated analogues. The coordination data here is reported without the intrinsic error levels involved. If these were considered, then only the data from the 2.5wt% systems could be deemed as significantly different.

The r values obtained for the two nitrate systems are nominally the same values as the chloride analogues, although slightly higher r values, ca. +0.01Å are attained in the RhN systems.

3.4 Transmission Electron Microscopy Study Of Rhodium Only Systems

Figure 3.13 shows a TEM image derived from a 'fresh' untreated 5wt%RhCl sample, i.e. the sample has only been subjected to the calcination and reduction procedures, and subsequent room temperature exposure to air. The supported particles, that are associated with the oxidic Rh component of the systems, are clearly visible on the background of Al_2O_3. The dark features present on the TEM images would normally be associated with metallic Rh particles, however the data obtained from EXAFS points to their native state as being largely oxidic. The current obtainable quality of the TEM does not however allow us to state definitively which phase is present under the conditions of the microscopy.

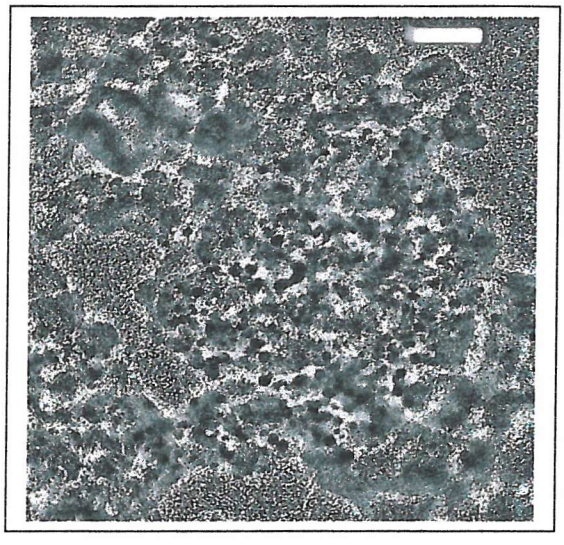

Figure 3.13: A TEM image of 5wt%Rh supported on γ-Al_2O_3, the dark areas show the Rh particles. The scale bar represents 20nm

Analysis of numerous TEM images of the catalytic systems, for which TEM was obtainable, leads to the particle size distribution shown in figure 14. The corresponding data from the TEM analysis is shown in table 3.6. Particles smaller than 4Å were not visible due to contrast features within the TEM images.

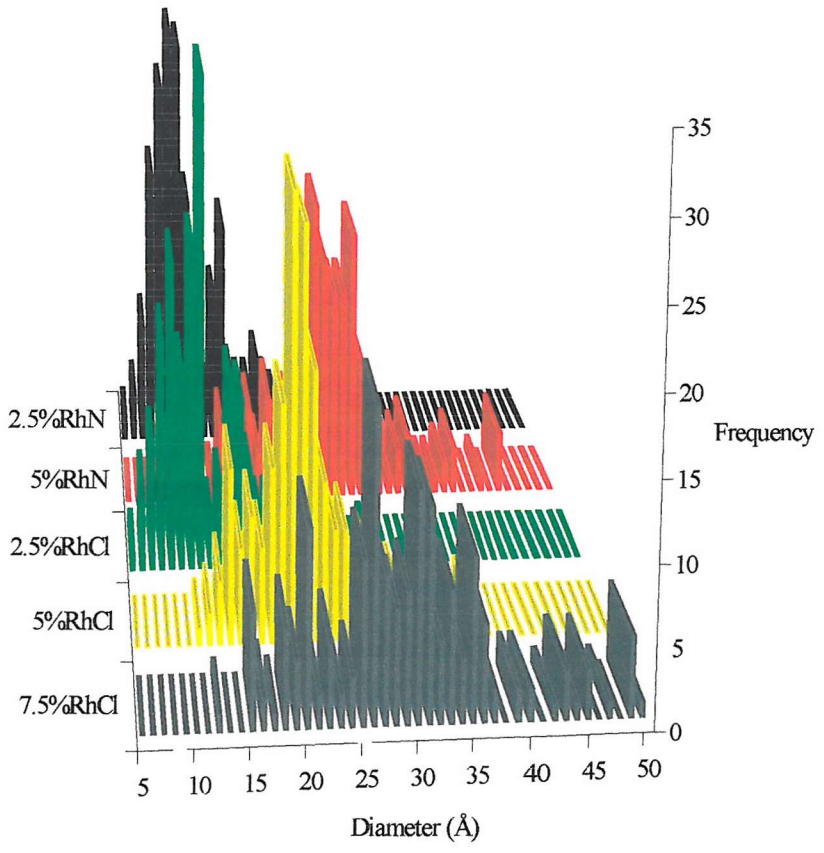

Figure 3.14: Particle size distribution for the Rhodium systems.

	7.5%RhCl	5%RhCl	2.5%RhCl	5%RhN	2.5%RhN
Average particle size (Å)	28.6	21.5	12.3	26	13.3
Std. Deviation	7.9	5.1	4.3	6.8	4.7
Number of atoms in particle (N_T)	612	225	50	460	62
Number of surface atoms (N_s)	228	117	42.8	188	49.6
Dispersion	0.37	0.52	0.85	0.41	0.8

Table 3.6: Information obtained from TEM images of the catalytic systems; (a) the average number of atoms (N_T) and surface atoms (N_s) are reported; (b) these estimates assume a hemispherical morphology; and (c) the dispersion is calculated as (N_s/ N_T).

The RhCl systems shown in the foreground of figure 3.14 highlight some interesting differences between the differently loaded systems.

A marked difference lies in the apparent increase of the average particle size as the Rh metal loading increases, from 12.3Å for the 2.5wt%RhCl system to 28.6Å for the 7.5%RhCl system. The number of atoms in a particle, which assumes a perfect hemi-spherical shape, and hence the corresponding number of atoms present at the surface is also seen to increase with metal loading as expected. The dispersion of the particles across the systems increases as expected with lower metal loading. The 2.5wt% and 5wt% systems show a relatively narrow particle size distribution, centred around 12Å and 20Å respectively, whereas the 7.5wt% system exhibits a larger distribution of particle sizes ranging from 12Å-50Å.

The RhN systems again show a difference with respect to their chloride analogues. The average particle sizes are larger compared to the RhCl systems, significantly in the 5wt% case, where the effective range of particle sizes are much greater than the RhCl system: 18-25Å for the chloride compared with 22-36Å for the nitrate system. However, this differential is not present in the 2.5wt% case.

The method used for calculation of the number of atoms present in the particles can be effectively visualised in figure 3.15, which shows the average coordination of the first coordination shell (N_1) as a function of number of atoms (N_{at}). Equation 3.1 is applied to a series of numbers to obtain the result, where the hyperbolic functions (a,b,c,d) are entered from the parameters of the first coordination shell delineated from the work of *Jentys.*[2] This method is therefore derived for EXAFS studies and specifically pertains to this, the TEM data obtained from the systems utilises average data to calculate the number of atoms. The associated errors are also plotted on the figure, which shows an inherent increase in error with increasing coordination number.

$$N_i = (aN_{at})/(b+N_{at}) + (cN_{at})/(d + N_{at}) \qquad \text{eq. 3.1}$$

Where Ni= (i) 1-5, abcd= parameters for hyperbolic function.

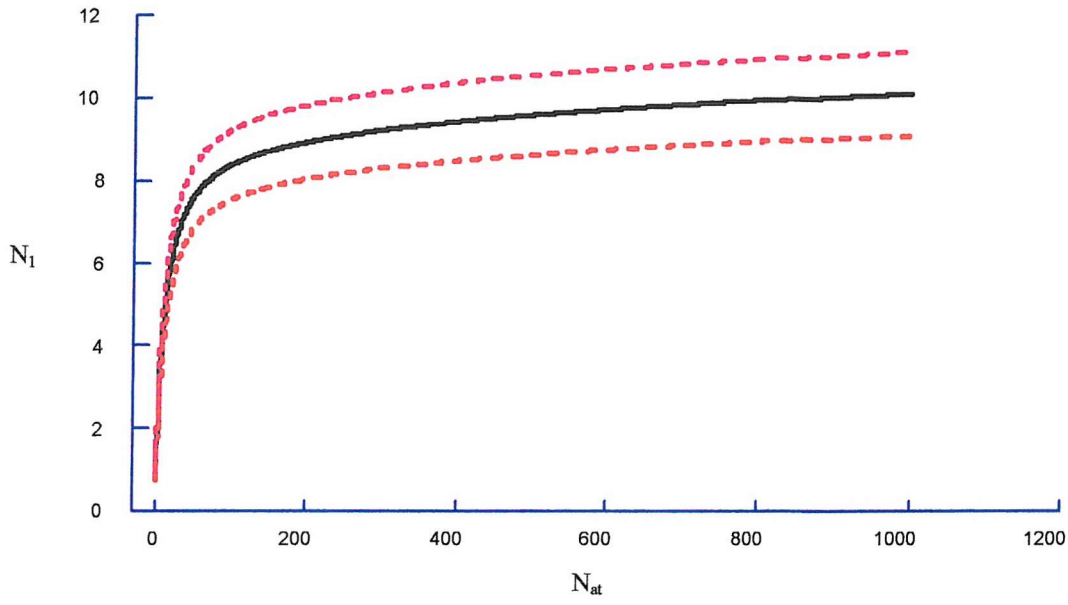

Figure 3.15: Average Coordination of the first coordination shell (N_1) as a function of the number of atoms (N_{at}). The dotted lines indicate the error domain associated with the values.

Figure 3.16 shows the correlation between the number of atoms present per average Rh particle and the metal loading, derived from the TEM data. The figure shows a good relationship, within error, between the theoretical and experimental data obtained from 'metallic' Rh EDE data (derived from room temperature work post H_2 exposure). A direct comparison between the theoretical and experimental values obtained via TEM would not be feasible as the TEM values assume that the particles are wholly metallic, whereas the EDE data shows the Rh phase to be oxidic. The theoretical measurements were obtained from an equation resulting from the work of *Jentys,*[2] allowing for the coordination data from this study to be analysed.

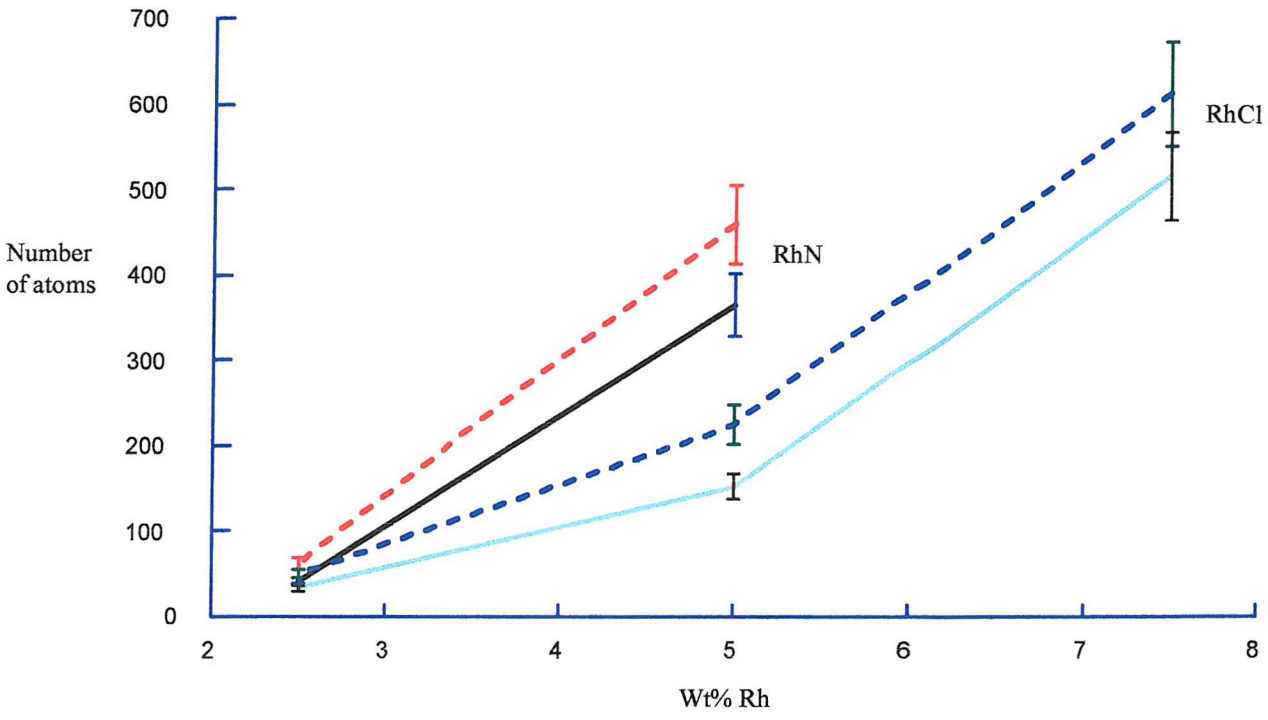

Figure 3.16: Comparison of theoretical and experimental number of atoms versus wt% Rh loading. The dotted lines indicate the experimental values obtained from TEM. Solid lines are those derived from the EDE after room temperature reduction of the catalysts. The error bars assume a ±10% error involved in the calculation of N_{at}. The error bars highlight the increase in error when working with larger coordination numbers in EXAFS.

The figure also highlights two interesting factors: firstly that EXAFS underestimates the 'true' coordination data of a system (derived from theoretical data), and hence the number of atoms present in a system. This effect of EXAFS can be seen despite the large error factors involved. Secondly, the increase in error values with increasing coordination number seen in figure 3.16 means that there is a larger percentage error involved in calculating the number of atoms per particle at higher coordination values (i.e. 'metallic' Rh values), although the TEM may not account for smaller particles present in the systems.

3.5 X-ray Photoelectron Spectrometry (XPS) Study of Rh only Systems

XPS spectra were taken for all Rh systems in their 'fresh' states, and all the data obtained highlight the Rh component to be oxidised at room temperature, thus reinforcing the observations made via the EXAFS experiments.

Figure 3.17 shows a typical XPS spectra sampled from the 5wt% RhCl system. The figure also overlays spectra taken from a bulk Rh foil and a pure sample of Rh_2O_3. It is evident from the differing binding energies obtained from the catalyst and bulk foil that the Rh component is in an oxidic phase, as the binding energy for the catalyst (analysing the 3d 5/2 peak only) is seen to be around 309eV, whereas the metallic Rh signature gives a value of around 307eV. The strong correlation between the catalyst and Rh_2O_3 XPS signature (BE=308.2-308.8) also highlights the phase of the Rh component, although the supported sample has a slightly higher binding energy than bulk Rh_2O_3 (ca. 0.7 eV).

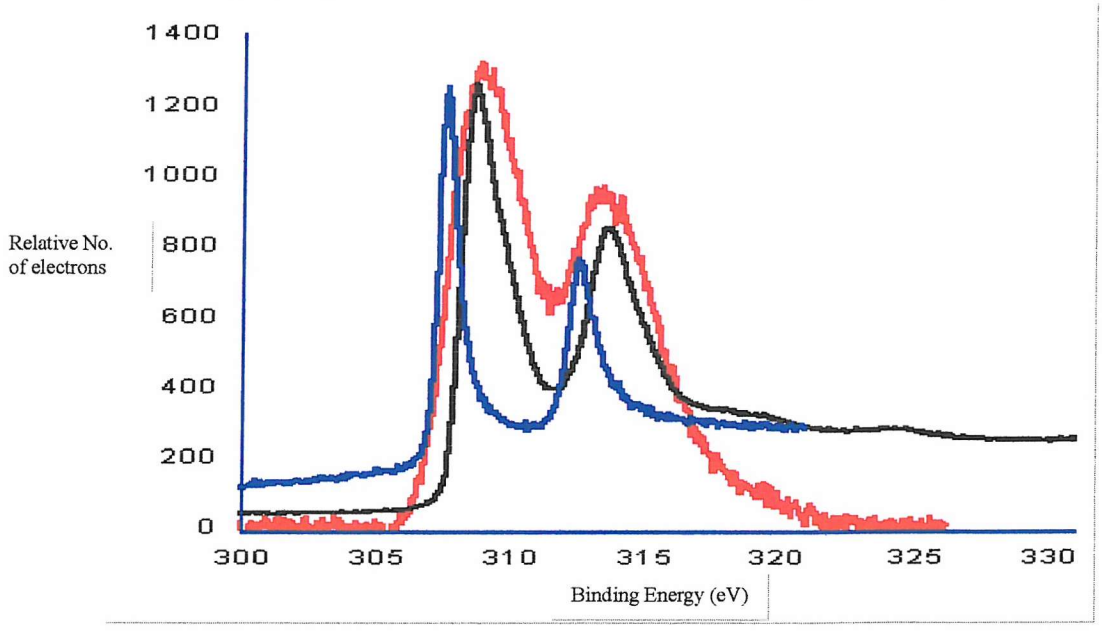

Figure 3.17: XPS spectra taken from the 5wt% RhCl catalyst. The blue line indicates spectra taken from the Rh foil; the black line is taken from the Rh_2O_3 sample; and the red line from the 5wt%RhCl catalyst.

The XPS data taken from the 5wt% catalyst exhibits broader peaks in the spectrum compared to the 'standard' spectra taken of the foil and the Rh_2O_3 sample. This can be principally attributed to the inherent static disorder associated with the catalysts. It is evident from the TEM data that the Rh component exists in differing sized particles, and hence the

Rh is in a variety of environments on the catalyst. Such variance will not be predominant in the 'standard' materials used.

The effect of chlorine present in the catalyst systems (made with the chlorine precursor) was also investigated with XPS. The Rh:Cl ratios were delineated to observe any possible trend with chlorine retention and metal loading. Figure 3.18 shows the increase in chlorine retention with increasing metal loading (and hence increasing particle size and decreasing dispersion).

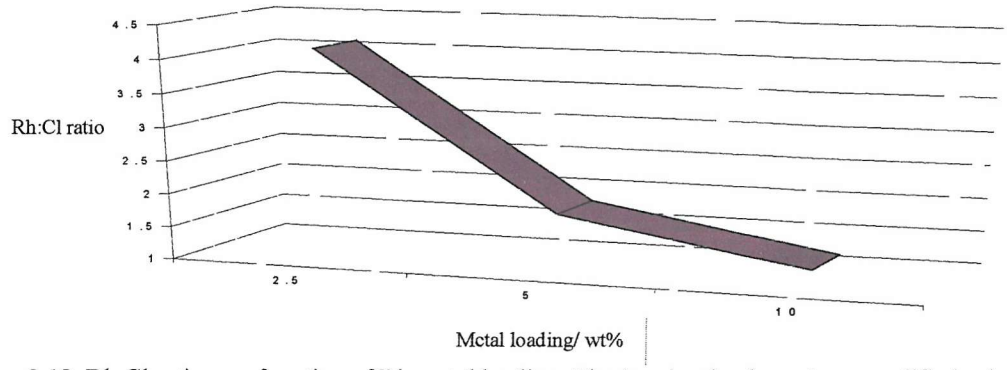

Figure 3.18: Rh:Cl ratio as a function of Rh metal loading. The 'raw' ratios have been modified using calculated sensitivity factors.

3.6 Catalytic Properties Of The Rhodium Systems

The catalytic properties and potential differences of the Rh systems were tested via the observation of two important reactions associated with the Rh component, the conversion of NO and the production of N_2O. Figure 3.19 shows the conversion of NO obtained via *in situ* mass spectrometry during the temperature controlled catalytic reaction for all of the Rh systems. It is evident from the figure that the conversion of NO takes place in the same region of light off, ca. 420K. There appears to be no apparent difference, within error limits, in NO conversion between the systems. Data for the 1% RhCl system is also shown, for which EDE data was of insufficient quality to permit analysis, which highlights the similar behaviour of the systems. Hence the region of light off and the subsequent catalytic reactions can be correlated with the subsequent collapse of the oxidic Rh phase to the metallic Rh phase.

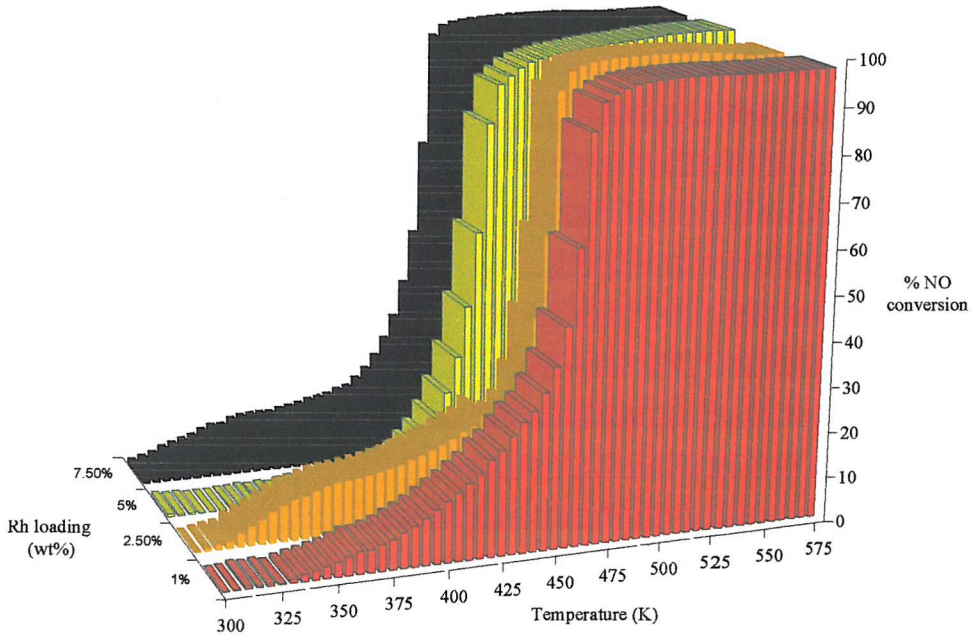

Figure 3.19: NO conversion as a function of reaction temperature in the reduction of NO/He by H_2/He over the RhCl systems. Light off for the conversion of NO occurs, within error, in the same region.

This effect is also seen in the consequent production of N_2O, shown in figure 3.20, where the apparent selectivity towards the catalytic reaction is similar, within error, between the systems. If the error factor is disregarded however, there is a slight decrease in selectivity

with decreasing metal loading. The presence of a second area of light off for the 2.5wt% sample is in fact due to anomalous CO_2 production, but in all cases below 500K this plot is an accurate representation of N_2O selectivity.

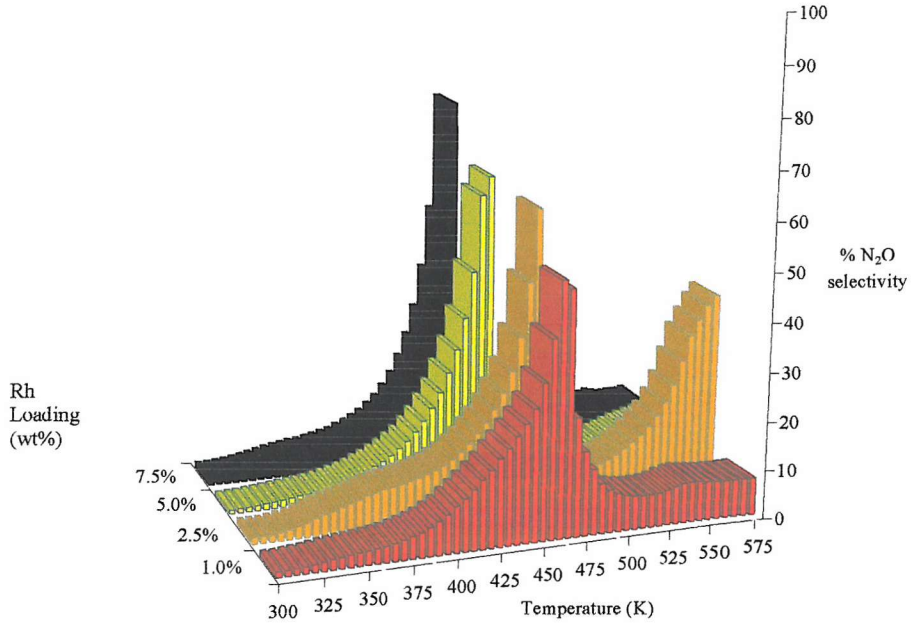

Figure 3.20: N_2O production as a function of reaction temperature in the reduction of NO/He by H_2/He over the RhCl systems. A slight decrease in selectivity with decreasing metal loading is observed.

3.7 Discussion And Conclusions

The Rh only systems investigated in this study were firstly experimented upon in their 'fresh' states after prolonged exposure to air. The techniques used to this end were EDE, TEM and XPS. It is clear form the data acquired from the complimentary EDE and XPS techniques that the 'fresh' Rh/Al_2O_3 samples, maintained under He, is not that expected for metallic Rh. The Rh component of the samples are instead clearly oxidised in all of the systems. This can be visualised in the results obtained from XPS, k^3-weighted EDE signatures and the corresponding low 'oxidic' coordination numbers.

The TEM essentially highlights the 'oxidic' Rh particles that are present at the surface of the catalysts, particles that would usually be associated with the metallic Rh phase. This assumption is present in previous work pertaining to Rh nanoparticles,[3] where the phase of the Rh is assumed to be metallic irrespective of the temperature.

The EDE however shows that the metallic phase cannot be present, as such particles in this phase would give N_1^{Rh} values around 7-8,[4] given their size as determined by TEM. The particles in TEM represent metallic Rh that constitutes only a small fraction of the total Rh content present in the system, the rest taking the form of an invisible oxide coating the Al_2O_3 support. Alternatively, the particles could be metallic but their formation is induced by an electron-induced decomposition of the oxidic phase (produced by the electron beam in TEM), which is indicated by EXAFS.[5]

Utilising different precursors to attain Rh metal loading on the catalysts seems to have a direct impact on the observed Rh phase present in the systems. The use of chlorinated and nitrate precursors yielded differing results compared to the nitrate based systems; the latter exhibiting less extensive oxidation than the former. This effect was observed in the EDE data, via consequently higher N_1^{Rh} values, and TEM, with an increase in subsequent particle sizes. Possible explanations of these effects could be the presence of chlorine in the systems effecting the Rh phase. The influence of chlorine in the work of Joyner and Johnston[6] was seen to affect the Rh systems by affecting the lability of the Rh particles. This work also concluded that the chloride present in the systems stabilised the Rh^I species, which would point to a possible reason why the nitrated systems are less extensively oxidised than the chlorinated systems. Another reason may be the chlorinated system essentially being a

'cleaner' system than the nitrated analogue. The relatively low calcination and reduction temperatures used here could result in N and O atoms remaining adsorbed on the Rh surface. A significant change of such species could pacify the surface by hindering the dissociation of O_2/NO, thus curtailing oxidation in these systems.

The physical state of the Rh component after exposure to the catalytic mixture of 40:60 NO/H_2 is observed to be markedly different from the 'fresh' oxidised state, for the higher loaded 7.5wt and 10wt% RhCl and RhN systems. The exposure process does not result in the same level of oxidation derived for the 'fresh' Rh samples exposed to air for a considerable time. A possible explanation for this is that after the initial, rapid, reaction with NO, a slower process of oxidation occurs. This slower process allows the Rh to oxidise 'fully', and would lead to surmise that the rate of oxidation falls below the capacity to measure it. This correlates well with the postulation made by Martens *et al.*,[7,8] who proposed an initial oxidation of the near surface Rh particles resulting in the formation of a particle comprised of a Rh_2O_3 exterior and metallic core. After this stage further 'bulk' oxidation of the remaining metallic core is considerably slower. The increase in metal loading, which shows less extensive oxidation after exposure, would support this explanation, as an essentially larger metallic Rh core exists in these systems. Again the role of chlorine in the systems may also affect this, as both of the RhN systems appear not to be as extensively oxidised after exposure to the catalytic mixture, compared with their 'fresh' states.

The elementary processes that apply to the formation of the Rh oxidic phase at the surface of the catalyst systems may therefore be broken down into a set of criteria.[4]

- The dissociative adsorption step can be assigned to be facile and highly exothermic, consequently injecting a large amount of energy into the nanocluster supported at the surface;
- The energy injected into the particle is excessive in terms of the particle being unable to release it via the particle-support interface or interaction with the gaseous phase. The particles are not of a sufficient size to provide an adequate energy sink, and therefore particle collapse cannot be prevented.
- The sintering of particles to larger metallic species does not occur due to the subsequent reaction with the gaseous environment possibly producing a new, stable phase.

After delineating that the Rh catalyst systems exhibit a considerable propensity for rapid and low temperature oxidation, the possible dynamic properties of the systems were observed via the NO/H_2 reaction as an in-situ, temperature controlled reaction.

Although there are many differences observed between the systems at room temperature, the catalysts behaved similarly during the catalytic experiment. This result correlates well with previous work regarding the influence of metal particle size on the catalytic properties of Rh.[9,10,25] For example, the activity and selectivity of comparable 2-4wt% Rh particles supported on alumina beads was indistinguishable when observed under the CO-NO reaction.[9] The EDE results follow the catalytic reaction with increasing temperature, and highlight the Rh phase to be oxidised further prior to 'light off'.

The EDE and mass spectrometry results highlight the Rh systems to exhibit a marked increase in catalytic activity over a relatively small temperature range. These rapid oxidative processes may be attributed to fundamental dissociative, potentially adiabatic,[11] chemistry, that occurs at the zero coverage limit upon metallic Rh particles.[12]

After the collapse of the oxidic Rh phase and the formation of particulate Rh at ca. 470K, shown by EDE and mass spectrometry, the value of N_1^{Rh} does not exceed a value of about 8, which indicates nanoparticulate particles containing between 70 and 150 atoms.[2] The catalytic properties were observed via the conversion of NO and the production of N_2O. Again the systems appear to exhibit the same catalytic properties, although a slight decrease in N_2O selectivity is observed with decreasing metal loading. The rapid curtailment of N_2O production shown by MS could be attributed to the formation of N_2O requiring the presence of both metallic Rh and oxidised Rh sites,[13] the latter being unobtainable at temperatures over ca. 500K.

The attainment of the catalytically active Rh phase at ca. 470K correlates well with the findings of Hopstaken *et al.*,[14] who noted that the dissociation of NO proceeds differently over supported Rh systems compared to the single crystal case. Moreover, catalytic studies of supported Rh systems,[3,9,10] similar to the systems investigated here, have generally only observed the metallic Rh phase at temperatures relating to automobile exhaust catalysis (i.e. ca.573K to 773K). Earlier work, such as the work by Oh and Carpenter,[10] did note the presence of an oxidised Rh_2O_3 phase at lower temperatures via XPS measurements, but the assumption of a metallic Rh phase throughout catalytic conditions was still implemented.

The majority of existing work relating to the catalytic properties of Rh make use of either low dispersed Rh single crystals[15-19] or Rh thin films,[20-22] which show markedly different catalytic behaviour to the highly dispersed system used in this system. Even analogous room temperature XPS studies[18] have made use of Rh thin films, thus declaring that metallic phases are present at all temperatures and pressures. It is this axiom, that these findings can be used as reasonable models for the supported Rh case, from previous work that has lead to recent, more thorough[4,5,12,23,24] investigations pertaining to supported Rh nanoparticles. This work, mentioned in chapter 1, accounts for the dynamic behaviour of the Rh particles on the nano scale, and also show that the conclusions drawn from experiments utilising low dispersed systems do not allow for these processes occurring over Rh. An example of this work by Campbell *et al.*[12] shows how metallic Rh nanoparticles are rapidly (within 5 seconds) oxidised by NO at room temperature, an observation that would not have been predicted by the previously mentioned axiom.

In conclusion, the rapid room temperature oxidation of nanoparticulate Rh is seen to be a recurring trend with the chlorinated systems, irrespective of particle size. This rapid oxidation is seen on the highly dispersed systems, which would not be predicted by the low dispersed, bulk case.

However, the RhN systems behave differently, it is clear from the EXAFS and TEM obtained that particle size effects are not the reason for the observed difference between the two systems. Although the RhN systems show larger particle sizes at higher metal loadings (7.5 and 10wt%) than the RhCl analogues, the particle sizes at the 2.5wt% level are essentially the same; therefore this effect cannot be assigned to be structural. For possible reasons outlined above, there is no apparent correlation between the structure of the catalyst, the presence of chlorine and varying metal loading.

All of the Rh systems can be reduced at room temperature by H_2, the potential rates for the re-oxidation of these systems however seems to vary with metal loading. This effect may be caused by a structural factor; the diffusion of O_2 could be slower with increasing metal particle size. However, even at the 10wt% loading a dynamic equilibrium between the oxidised and reduced Rh phases exists.

In terms of reactivity, although there is a difference in structure between the RhN and RhCl systems, the systems all exhibit the same activity and selectivity under catalytic

conditions. There seems to be a common 'intermediate' between the oxidic and metallic Rh phases, as there is enough oxidation at the surface for this to occur. The consequent production of N_2O via the NO^+ species can therefore be assigned to be intrinsic to these bi-stable Rh nanoparticles. From this postulation it would be reasonable to surmise that the Rh component would not have to be fully oxidised for this behaviour to occur, even a thin layer of oxidation would suffice.

After light off temperatures are attained and the subsequent collapse of the Rh phase occurs, the particulate Rh is seen to be very selective for the reduction of NO to N_2.

It is therefore the potential for the aforementioned equilibrium between the Rh phases, that is responsible for the 'unwanted' production of N_2O, and removing this bi-stability, the introduction of an adjunct metal, palladium, is investigated in the next chapter.

In summary, the catalytic experiments highlighted that the selectivity of the reduction of NO by H_2 to N_2, occurring on reduced metallic sites, and N_2O, occurring on oxidised sites, can be directly attributed to the phase of the rhodium. The interconversion of the Rh phase appears to occur over a very short time scale and temperature range, highlighting the dynamic response of the supported Rh nanoparticles present in the systems under investigation.

3.8 References

(1) D. Burnaby, PhD Thesis, University of Southampton, 2000.

(2) A. Jentys, *Phys. Chem. Chem. Phys.*, 1999, **1**, 4059.

(3) G. Rupprechter, K. Hayek, H. Hofmeister, *J. Catal.*, 1998, **173**, 409.

(4) M.A. Newton, A.J. Dent, S. Diaz-Moreno, S.G. Fiddy, J. Evans, *Angew. Chem. Intl. Ed.*, 2002, **41**, 2587.

(5) M.A. Newton, B. Jyoti, A.J. Dent, S. Diaz-Moreno, S.G. Fiddy, J. Evans, *J. Phys. Chem. B.*, Submitted.

(6) P. Johnston, R.W. Joyner, *J. Chem. Soc. Faraday Trans.*, 1993, **89**, 863.

(7) H.A Martens, R. Prins, H. Zandbergen, D.C. Koningsberger, *J. Phys. Chem.*, 1988, **92**, 1903.

(8) H.A Martens, R. Prins, D.C. Koningsberger, *J. Phys. Chem.*, 1989, **93**, 3179.

(9) S.H. Oh, C.C. Eickel, *J. Catal.*, 1991, **128**, 526.

(10) S.H. Oh, J.E. Carpenter, *J. Catal.*, 1983, **80**, 472.

(11) H. Neinhaus, *Surf. Sci. Rep.*, 2002, **45**, 1.

(12) T. Campbell, A.J. Dent, S. Diaz-Moreno, J. Evans, S.G. Fiddy, M.A. Newton, S. Turin, *Chem. Communn.*, 2002, 304.

(13) T. Chafik, D.I. Konarides, X.E. Verykios, *J. Catal.*, 2000, **190**, 446.

(14) M.J.P Hopstaken, J.W. Niemantsverdriet, *J Phys. Chem. B.*, 2000, **104**, 3058.

(15) B.E. Nieuwenhuys, *Adv. Catal.*, 2000, **44**, 259.

(16) C.H.F. Fenden, D.W. Goodman, D.S. Blair, P.J. Berlowitz, G.B. Fisher, S.H. Oh, *J. Phys. Chem.*, 1988, **92**, 1563.

(17) G.L. Kellog, *J. Catal.*, 1985, **92**, 167.

(18) A. Tolia, R.J. Smiley, W.N. Delglass, C.G. Takondis, M.J. Weaver, *J. Catal.*, 1994, **150**, 56.

(19) J. Koshy, *Thin Solid Films*, 1978, **51**, 56.

(20) J.H. Lasen, I. Chorkendorff, *Surf. Sci. Rep.*, 1999, **35**, 163.

(21) M.M. Bowker, Q. Guo, R.W. Joyner, *Surf. Sci. Rep.*, 1999, **35**, 163.

(22) F.M. Leibsle, P.W. Murray, S.M. Francais, G. Thornton, M. Bowker, *Nature*, 1993, **92**, 1903.

(23) M.A. Newton, D.G. Burnaby, A.J. Dent, S. Diaz-Moreno, J. Evans, S.G. Fiddy, T. Neisius, S. Pascarelli, S. Turin, *J. Phys. Chem. A.*, 2001, **105**, 5965.

(24) M.A. Newton, A.J. Dent, J. Evans, *Chem. Soc. Rev.*, 2002, **31**, 83.

(25) M. Menon, B.C. Khanra, *Indian J. Chem., Sec. A.*, 1998, **37**, 802.

Chapter 4

Rhodium and Palladium Systems

4.1 Introduction

Following the investigation of the catalytic systems containing rhodium as the 'active' metal, the role of palladium as an adjunct metal component was investigated. The experiments performed on these systems were analogous to the experiments conducted on the 'Rh only' systems to allow for direct comparisons to be made and the role of Pd in the systems to be observed. The experiments will allow for the investigation of how inherent factors such as segregation events, alloy formation, phase changes and possible hydrogen spillover affects the performance and structure of the metal components present in the systems.

The procedure for determining the correct DW factors, as outlined in chapter 3, was also performed for Pd, utilising a 5wt% Pd sample. Two sets of data were obtained for analysis of the Pd containing systems, one data set was taken with the Pd exposed to He, and the other exposed to H_2. The cooling experiments were undertaken in He and H_2 as the DW factors for Pd metal and a possible low temperature PdH_x phase may be different.

Figure 4.1 shows the difference between the DW factors obtained for the experiment under H_2 and He, highlighting the difference between the two values at low temperatures. Although these differences are present, they cannot be assigned as significant, the two differing sets of values were however used in the analysis of EXAFS data.

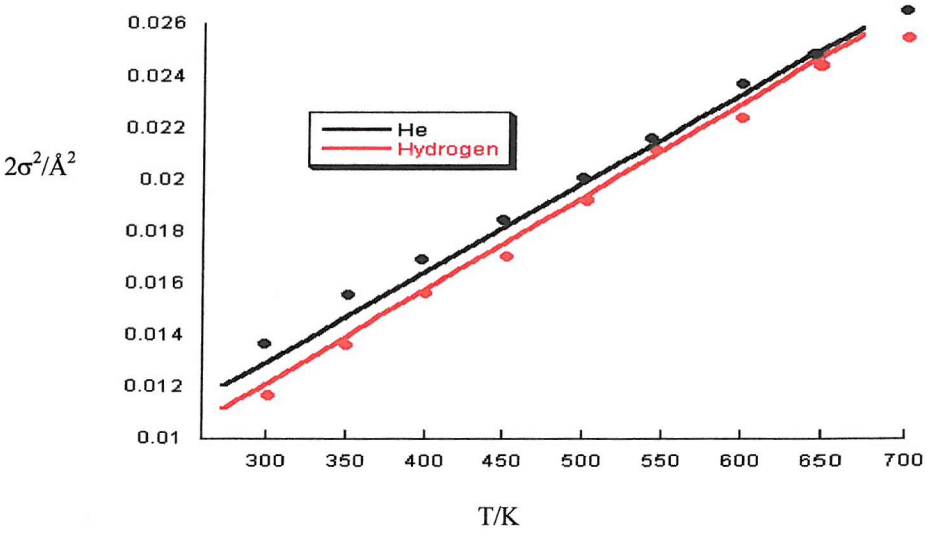

Figure 4.1: Plot of DW factor as a function of temperature. The difference in the two environments producing differing DW factors is highlighted.

The Pd K-edge EDE spectrum and its Fourier transform for a Pd foil is shown in figure 4.2, with the corresponding physical data listed in table 4.1. This highlights the EDE signature for bulk Pd and the consequent calibration obtained for the analysis of the Pd systems. The foil was run at room temperature and was analysed with full multiple scattering for five shells.

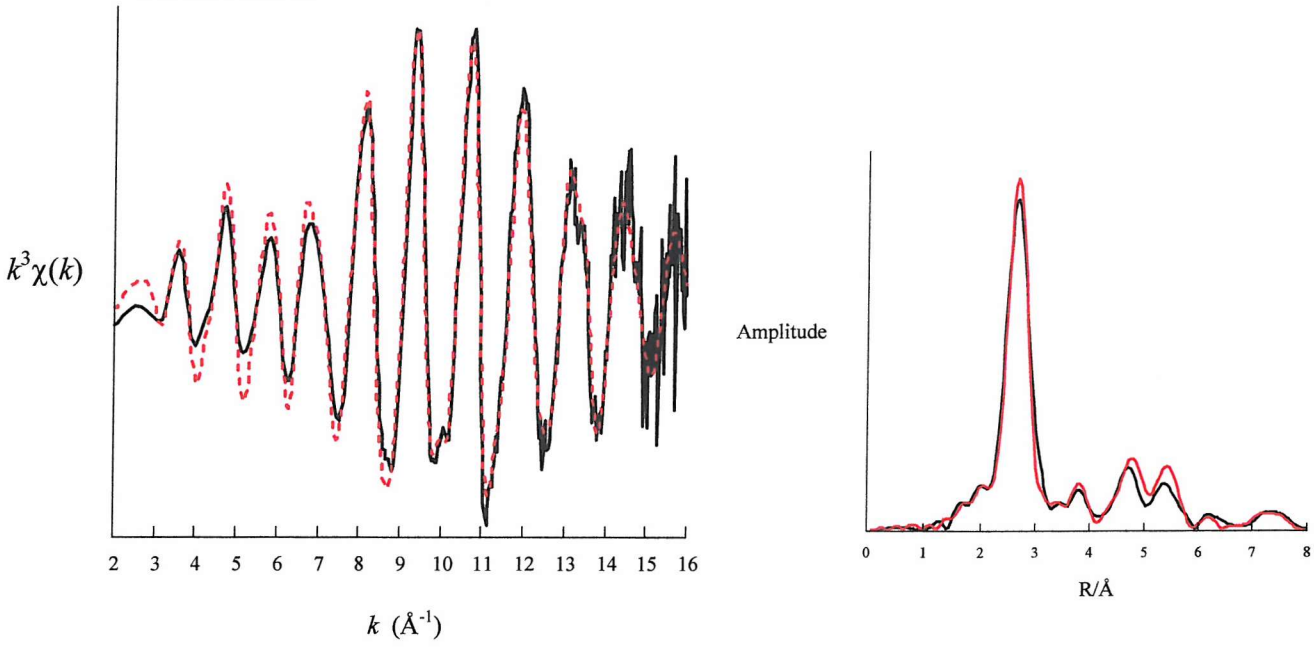

Figure 4.2: Rh *k*-Edge EXAFS spectra for Palladium foil and the corresponding Fourier transform.

Sample	Time/spectrum	k_{min} (Å^{-1})	k_{max} (Å^{-1})	Shell	CN	*r/Å*	$2\sigma^2$/Å^2
Pd Foil(N_1)	9 msecs	2	15	Pd	12	2.746	0.013
Pd Foil(N_2)	9 msecs	2	15	Pd	6	3.9	0.02
Pd Foil(N_3)	9 msecs	2	15	Pd	24	4.78	0.018
Pd Foil(N_4)	9 msecs	2	15	Pd	12	5.509	0.024
Pd Foil(N_5)	9 msecs	2	15	Pd	24	6.199	0.021

Table 4.1: Elemental coordination (N_x^s), bond length (R), and statistical parameters derived from explicit analysis of EDE spectra in figure 2. Ef= -4.3, R= 20%

4.2 Study of a Pd Only System

Prior to the analysis of the Rh/Pd systems, a 'Pd only' system was analysed to observe its intrinsic properties. Figure 4.3 shows the k^3-weighted Pd edge EDE spectra for the 5wt% Pd system taken under 'fresh' conditions, after a room temperature reduction by H_2, and after exposure to the catalytic mixture, a 60:40 mix of NO/H_2. Initial observation of the signatures shows the EXAFS intensity to decrease markedly from the 'fresh' signature after exposure to H_2 and the catalytic mixture. There is also an apparent phase shift accompanying this change, which is rationalised below.

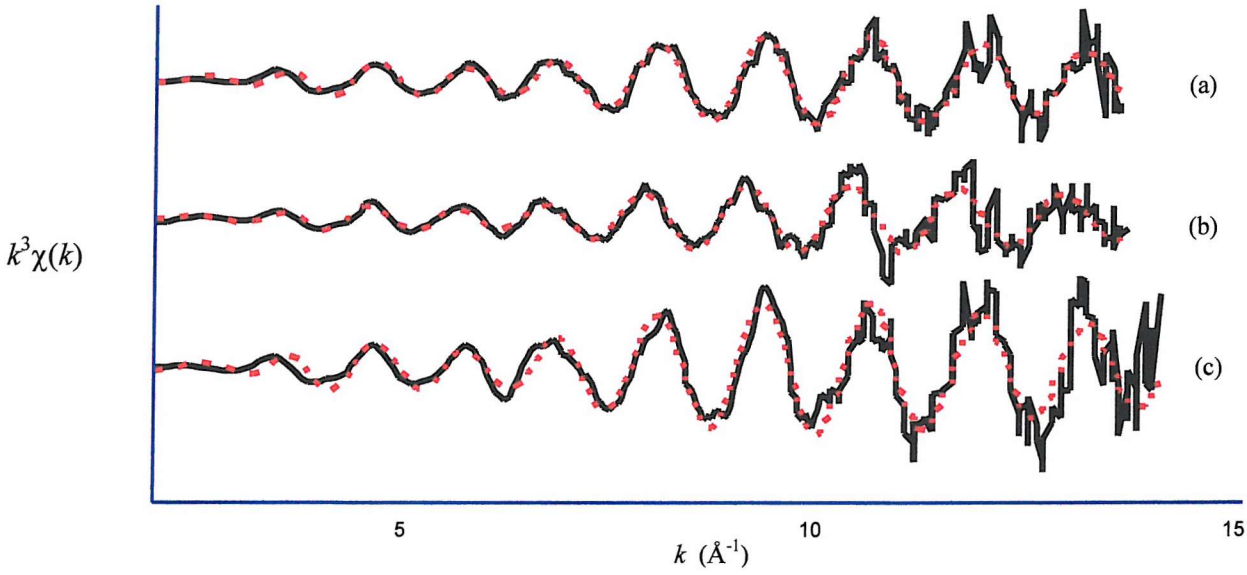

Figure 4.3: k^3-weighted EDE spectra of the 'fresh' 5wt% Pd system under (a) 60:40 NO/H_2 catalytic mixture; (b) H_2 and (c) He.

Spectrum	Scatterer (s)	k_{min} (Å^{-1})	k_{max} (Å^{-1})	CN	*r*/Å	$2\sigma^2$/Å^2	E_F	R (%)
5wt% Pd under He	Rh	2	14	11	2.763	0.011	-8.312	42.75
5wt% Pd under H_2	Rh	2	14	6.5	2.821	0.013	-3.254	48.3
5wt% Pd under NO/H_2	Rh	2	13.5	7.6	2.767	0.011	-6.63	40.58

Table 4.2: Data derived from analysis of EDE spectra in figure 4.3.

The data in table 4.2 shows the 'fresh' Pd system [trace (c)] to have an essentially metallic signature, with no apparent (room temperature) oxidation of the Pd component present. After the room temperature reduction of Pd by H_2, a surprising result is observed. The coordination

number apparently falls from a 'metallic' N_1^{Pd} value of 11 to 6.5 after exposure to H_2. This effect is markedly different to that observed in the Rh only case, where the metal component was reduced in the presence of H_2 to give a wholly metallic signature. Consequently, the Pd component does not 'recover' to its original state after exposure to the catalytic mixture. These processes occurring over the Pd can be attributed to the well known bulk uptake of H_2 by Pd at room temperature yielding a 'swollen' PdH_x phase, discussed later in this chapter. The lack of 'recovery' of the Pd component after exposure to the catalytic mixture could be attributed to the continued presence of hydrogen in the particle bulk. Although these processes are apparent at room temperature, there is no indication of any catalysis occurring. The changes occurring over the Pd component can also be visualised in figure 4.4, which shows the Pd-M bondlengths. The decrease in Pd coordination can also be observed in the subsequent increase in bondlength, from 2.76Å in the 'fresh' state to 2.82Å after exposure to H_2.

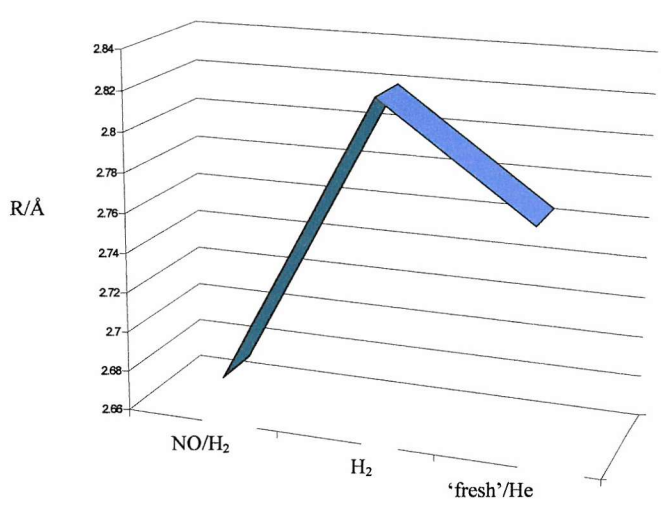

Figure 4.4: Bondlength values for the Pd system after exposure to the environments indicated.

Figure 4.5 shows the N_1^{Pd} data acquired during the temperature controlled catalytic experiment. The values obtained from the experiment highlight the apparent low N_1^{Pd} values obtained prior to the experiment to have increased to a value of ca. 10 by 308K. Stabilisation of the coordination numbers occurs by ca. 350K, where the N_1^{Pd} value is around 11.5. The changes occurring here can be attributed to the collapse of the apparent PdH_x phase to the

metallic Pd phase with increasing temperature, the bulk hydrogen being desorbed at higher temperatures to yield the stable metallic Pd phase.

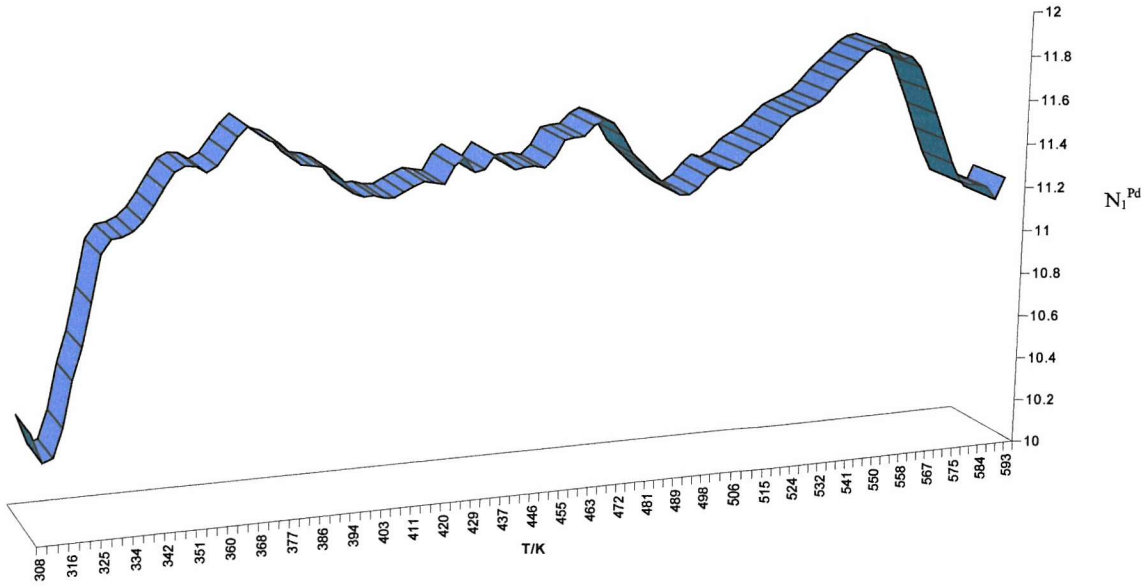

Figure 4.5: Coordination data for the 5wt% Pd system as a function of temperature, during the catalytic experiment.

4.2.1 TEM Study of the Pd only system

Figure 4.6 shows the TEM particle sizes distribution data derived from a 'fresh' untreated 5wt%Pd sample, after room temperature exposure to air. The supported particles, that are associated with the Pd component, were clearly visible on the background of Al_2O_3. The dark features present on the TEM images analysed can be assigned to be metallic Pd, as the EXAFS data derived from the fresh sample highlights the Pd phase not to be oxidised at room temperature. The average particle size of the Pd component is observed to be ca. 48Å, and has a broader effective distribution of particle sizes than the analogous Rh system, ranging from 23Å to73Å. Table 4.3 shows the statistical data derived from the TEM analysis. The figures reported here are based upon averages of the data accumulated, and assume particles to exist in a hemispherical state.

	5wt% Pd
Average particle size (Å)	48.4
Std. Deviation	9.8
Number of atoms in particle	2762
Number of surface atoms	624
Dispersion	0.225

Table 4.3: Statistical information obtained from TEM images of the 5wt% Pd system.

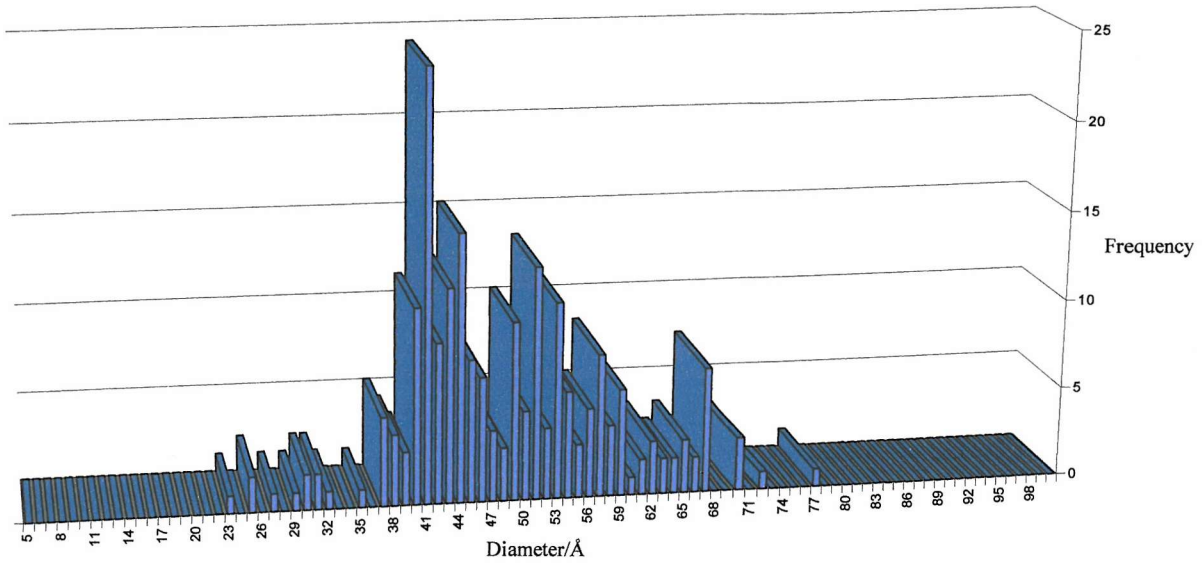

Figure 4.6: Particle size distribution for the 5wt% Pd system. TEM images were taken at room temperature under exposure to air.

4.2.2 Catalytic properties of the Pd only system

Figure 4.7 shows the NO conversion data acquired during the catalytic experiment. The data shows the consequent light off region to be around 340K, which subsequently correlates to the stabilisation of the metallic Pd phase reported by EXAFS. The catalytic activity of the Pd component may therefore be tentatively attributed to the formation of the 'fully' metallic Pd phase, which is also highlighted in the N_2O selectivity of the system, shown in figure 4.8.

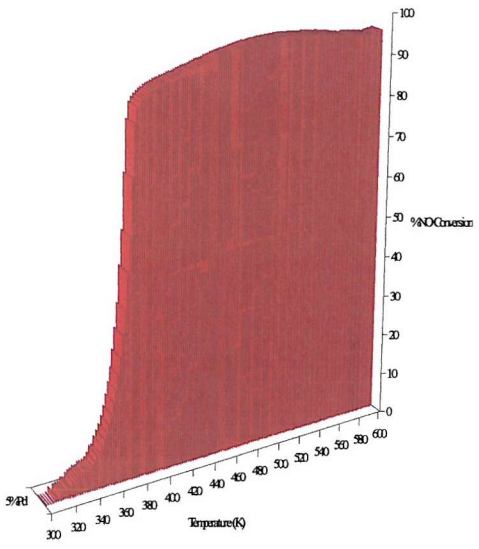

Figure 4.7: NO conversion as a function of temperature over the 5wt% Pd system.

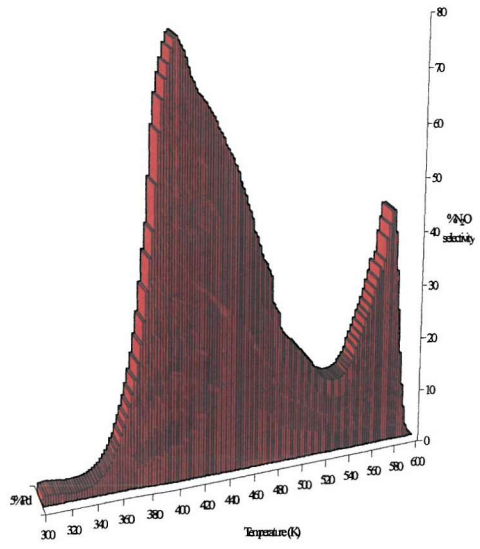

Figure 4.8: N_2O selectivity (mass 44) as a function of temperature over the 5wt% Pd system.

The consequent production of N_2O at the light off region is seen to decrease to a minimum by 490K. The higher selectivity towards N_2O by the Pd system compared to the analogous Rh system is an expected result due to the intrinsic property of Pd to catalyse this reaction (see discussion). This effect correlates well with previous surface science work, which shows that N_2O production is an intrinsic property of the surface chemistry of Pd, whereas this is not the case for Rh surfaces (see discussion). The area of increased N_2O production at T>530K can be attributed to anomalous CO_2 production. The catalytic properties and processes occurring over the Pd system will be discussed in detail below, where it is compared to the other Pd containing systems.

4.3 Energy Dispersive EXAFS study of Rh and Pd Supported Nanoparticles on γ-Al_2O_3

Figure 4.9 shows the k^3-weighted Rh K edge EDE spectra derived from 'fresh' samples of 4.5%Rh/0.5%Pd, 4%Rh/1%Pd and 5%Rh for comparison. The spectra shows the Rh and Pd components of both species to be partially oxidised, an expected result due to extensive exposure to air at room temperature. However, the EDE signatures highlight a definite difference in EXAFS intensity between the two systems. Incorporation of Pd at the 1wt% level has resulted in a metallic Rh signature, i.e. the Rh has been effectively insulated against room temperature oxidation. An analysis of the XANES structure of the two systems reveals that an intermediate situation is present in the case of the 0.5wt%Pd system, it is neither fully oxidised nor fully reduced. Therefore it is only at the 1wt% Pd level that an absolutely metallic signature is seen.

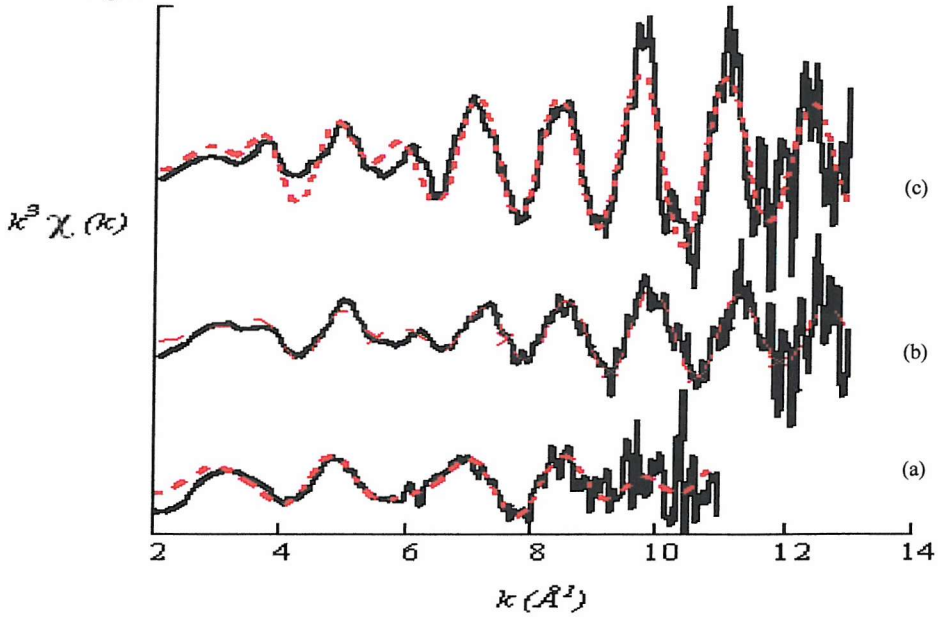

Figure 4.9: k^3-weighted Rh K edge EDE spectra derived from 'fresh' samples: (a) 5wt% Rh; (b) 4.5wt%Rh:0.5wt%Pd; and 4wt%Rh:1wt%Pd.

An expected result is again observed via the EDE signatures after exposure to the catalytic mixture, with the 1wt%Pd and 0.5wt%Pd systems not being as extensively oxidised compared with their 'fresh' states. However, this effect is most marked for the 1%Pd system, the Rh component giving a more 'metallic' signature than the system with Pd loaded at the 0.5wt% level.

This observation is carried forward into the catalytic experiments performed on the systems, figure 4.10 shows the NO conversion as a function of temperature for both systems.

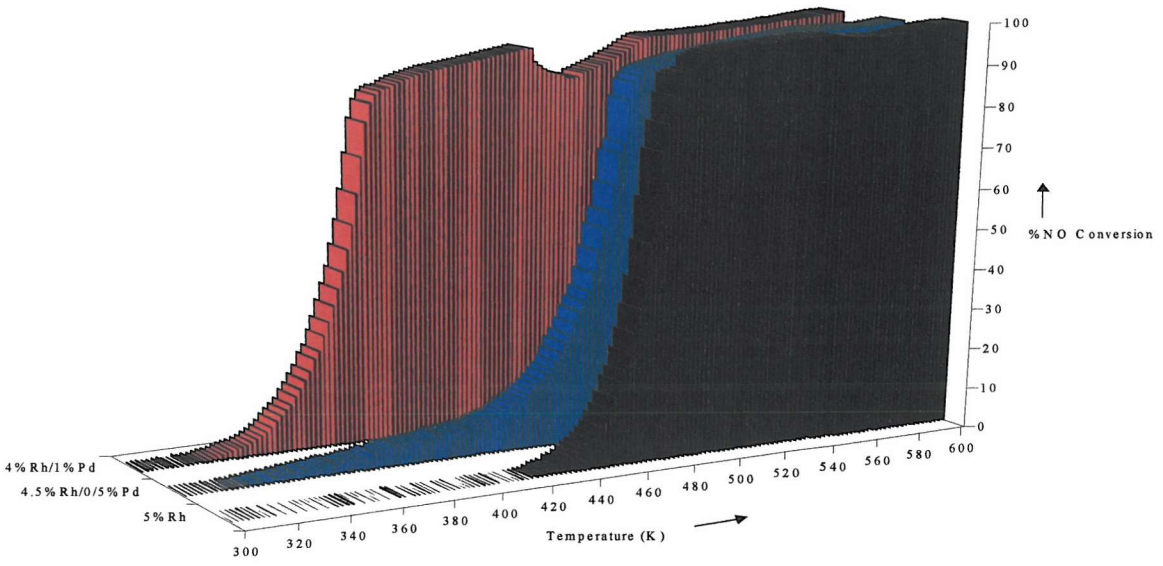

Figure 4.10: NO conversion as a function of temperature occurring over the systems indicated.

It is evident from figure 4.10 that the 0.5wt%Pd system behaves very similarly to the 5wt% Rh system, although the formation of metallic Rh particles occurs over a broader temperature window. The results show a marked difference in catalyst properties when the Pd loading is marginally increased from the 0.5wt% level to the 1wt% level, in that the behaviour of the system becomes very similar to the 'Pd only' case. A significant lowering of light off temperature is observed for the 1wt% system, by ca. 60K. The Pd/Rh *k* edge data derived from the EDE experiment performed on the 1%wt Pd system highlight both components to have a metallic phase at all temperatures, under reactive conditions. This relatively small change in Pd loading has a marked impact on the overall behaviour of the catalyst when compared to the 0.5wt% Pd system, in which the Rh component stays heavily oxidised until the light off region. This system therefore behaves similarly to the 5wt% Rh system. The Pd-M bondlengths derived from the 1%Pd system shown in figure 4.12, indicate a 'Rh like' environment present, as opposed to Pd-M bondlengths expected from phase separated and discrete Pd particles. The Pd loaded at the 1wt% level has it seems therefore resulted in the formation of RhPd nanoparticles. Although the 1wt% Pd system does give

consistently higher r values, the individual measurements cannot be viewed as significant as errors intrinsic to the analysis are between 1.5-5%.

This observation is also seen in the TEM data derived from the 1wt% Pd sample, the particle size distribution for this system is shown in figure 4.11 and the statistical data shown is shown in table 4.4.

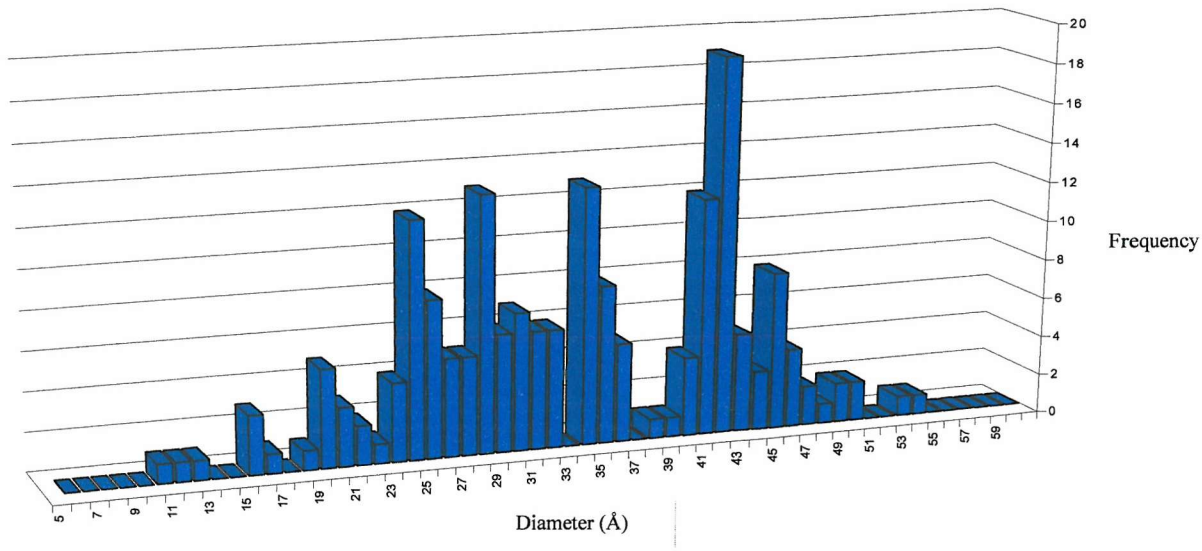

Figure 4.11: Particle size distribution for the 4wt%Rh:1wt%Pd system.

	4wt%Rh:1wt%Pd
Average particle size (Å)	32.5
Std. Deviation	16.31
Number of atoms in particle	989
Number of surface atoms	416
Dispersion	0.43

Table 4.4: Statistical data derived from the data in figure 4.11.

The TEM data shows 4wt%Rh:1wt%Pd system to exhibit a bimodal particle size distribution. This could be due to the metal components, and hence particles, no longer existing as discrete entities, i.e. alloying has occurred. This could occur due to the effect of phase separation, where 'Rh-like' nucleation sites yield smaller particles, and 'Pd-like' sites yield the larger particles seen. The predominant particle size regime ranges from ca. 24-34Å and 40-43Å. This result is consistent with similar studies[1] of supported Rh/Pd systems, where comparable particle sizes were defined, even though microcluster sized particles were

sampled. The TEM data acquired for the other alloyed systems was of insufficient quality to permit analysis.

Discussion in chapter 1 reported Rh and Pd to be essentially immiscible in the bulk across the compositional range at moderate temperatures,[2,3] but the results obtained here show that this hypothesis cannot be applied for the systems being observed on the nanoscale. This reinforces results of the structurally indirect techniques such as IR studies.[4] The observed alloying of the metal components results in the 'insulation' of the Rh component against the extensive, and rapid oxidation by NO as observed in the 'Rh only' containing systems. An overall lowering of light off temperature, inherent to any catalyst design, is also observed, compared with the Rh only system.

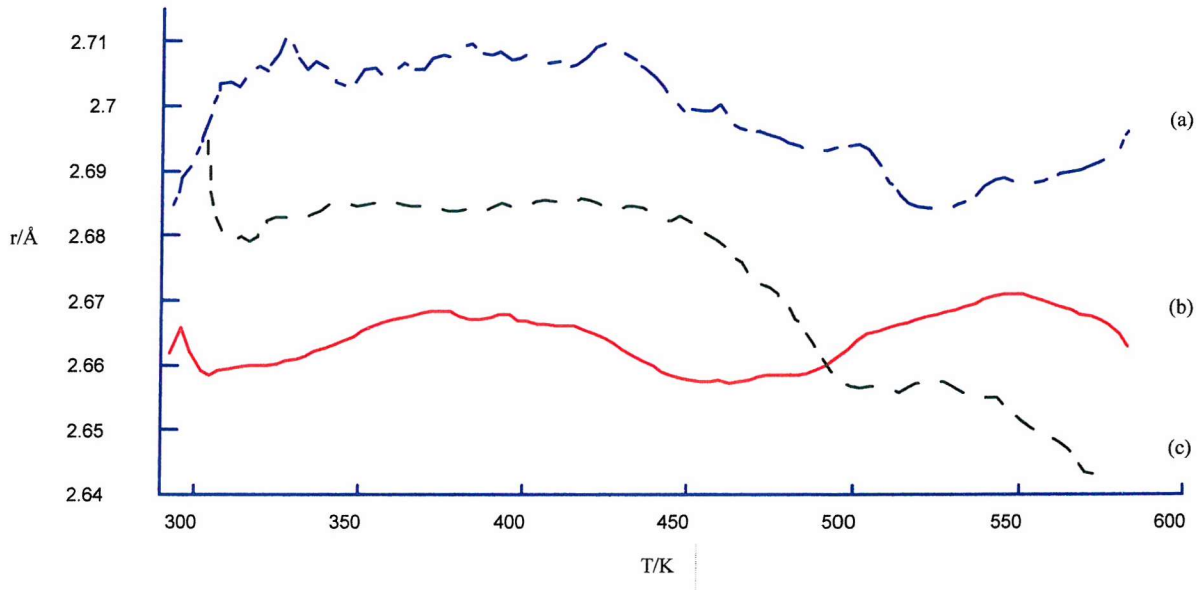

Figure 4.12: Metal-metal bondlengths as a function of temperature for (a) 4wt%Rh derived from the Rh *k* edge; (b) 1wt%Pd derived from the Pd *k* edge and (c) 4.5wt% Rh derived from the Rh *k* edge. Data derived from the 0.5wt% Pd case was of insufficient quality to permit analysis.

The results from the 1wt% Pd system also show the metal components to exhibit dynamic behaviour under reactive conditions, across the temperature range. Figure 4.13 shows the $N_1^{Rh/Pd}$ values for the 1wt% Pd system derived from the Pd *k* edge. The figure shows N_1^{Pd} values to initially rise from a room temperature value of ca. 6 to 9.7 in the light off region.

Interestingly, the N_1^{Pd} value decreases back to a value of ca. 7 before increasing again at temperatures over 500K to a value of around 9. The changes observed in the Pd *k* edge can be assigned as significant, as they occur at greater than the 15% level.

The Rh *k* edge derived data also shows a rise in coordination parallel to this region, from a value of 8.7 to a maximum of 9.5, before stabilisation at higher temperatures. This is effectively shown in figure 4.14, where the data from the Rh *k* edge from the 0.5wt% Pd system is shown for comparison. These changes in the metal components can be attributed to a second segregation event, and hence the reoccupation of low coordination sites by the Pd. After these events, at higher temperatures, a re-homogenisation of Rh and Pd is observed.

The figure also highlights the apparent 'Rh like' behaviour of the 0.5wt% Pd system mentioned before, where similar coordination numbers and light off temperatures are observed.

The average size and surface composition of the RhPd nanoparticles can therefore be thought of as being fluxional under the catalytic conditions employed. Therefore, in this case, a very high percentage of the Pd present has been segregated to the surface with the nanoparticles containing, on average, 30-270 atoms (~11-22Å diameter). This observation is highlighted by the EDE data, which shows an initially low value of N_1^{Pd} compared to a higher initial value of N_1^{Rh}. Furthermore, these low N_1^{Pd} values indicate the Pd atoms to preferentially occupy surface within the particles supported in this system.

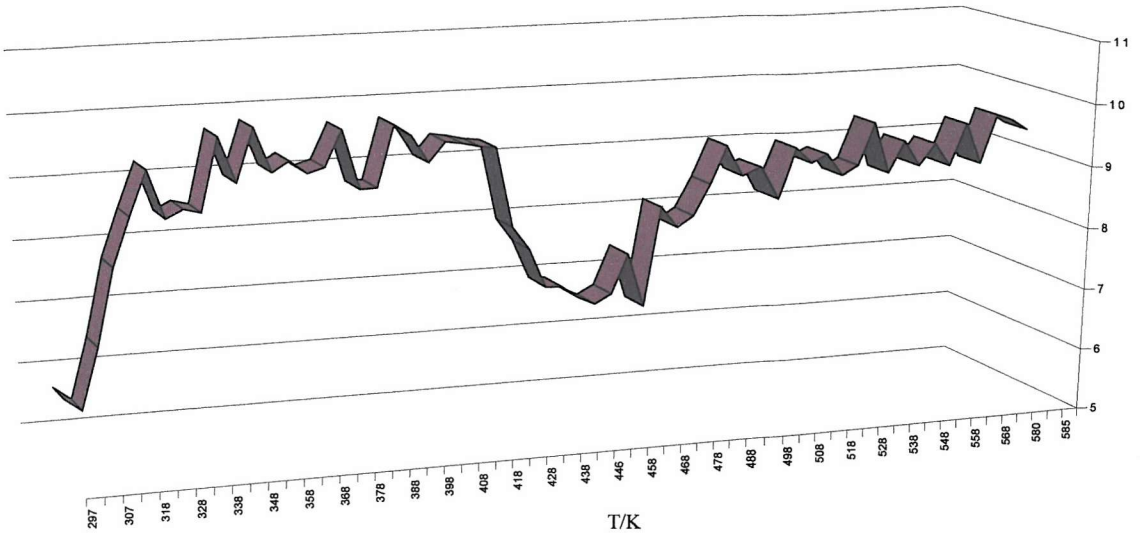

Figure 4.13: Coordination data as a function of temperature for the Pd *k* edge of the 4wt%Rh:1%Pd system. Data derived from the 4.5wt%Rh:0.5wt%Pd case was of insufficient quality to permit analysis.

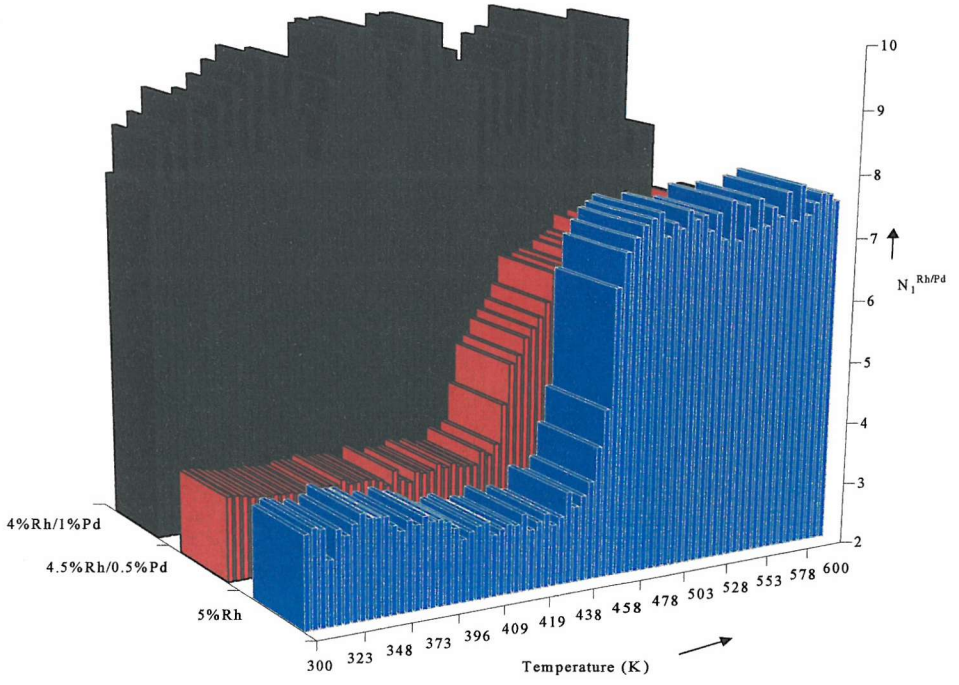

Figure 4.14: Coordination data derived from the Rh *k* edge as a function of temperature for the systems indicated.

4.4 Study of a Physically Mixed Sample

Figure 4.15 shows k^3-weighted Rh K edge EDE obtained from three 'fresh' systems; a physically mixed sample comprising of equal quantities of 5wt% Rh and 5wt% Pd; the 4wt% Rh:1wt% Pd system; and 5wt% Rh system for comparison. Figure 4.16 shows the data derived from the Pd k edge for the physically mixed system and the 4wt% Rh:1wt% Pd system after exposure to H_2 at room temperature. Tables 4.5 and 4.6 show the relevant data derived from the respective systems.

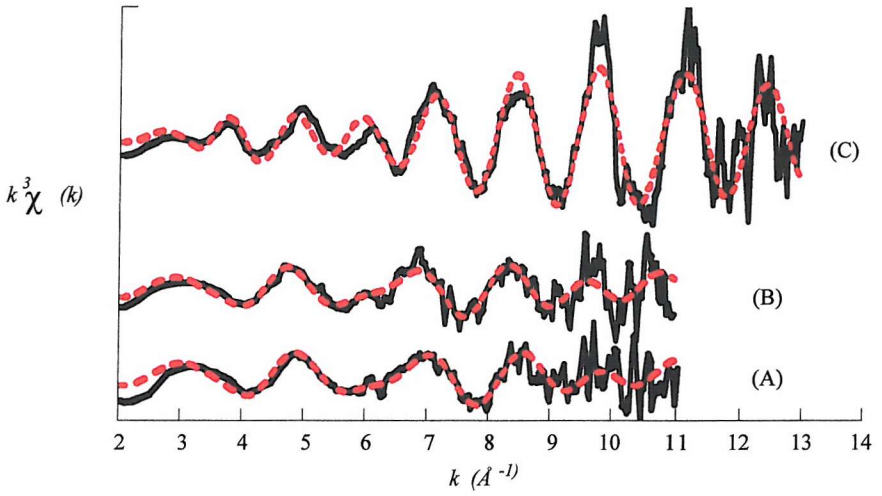

Figure 4.15: k^3-weighted Rh K edge EDE spectra derived from 'fresh' samples: (A) 5wt% Rh; (B) a physical mixture comprising equal weights 5wt% Pd/Rh; and (C) 4wt% Rh: 1wt% Pd.

Sample	k_{min} (Å^{-1})	k_{max} (Å^{-1})	Shell	CN	r/Å	$2\sigma^2$/Å^2	E_F	R (%)
(A) 5% Rh/Al_2O_3	2	11	Rh	2.1	2.66(3)	0.011(2)	-2.4	57.3
			O	3.0	1.97(1)	0.005(1)		
(B) 5% Rh/Al_2O_3 + 5%Pd/Al_2O_3	2	11	Rh	2.3	2.71(3)	0.011(2)	-3.6	64.1
(Physical Mixture)			O	2.7	2.04(1)	0.005(1)		
(C) 4%Rh/1%Pd/Al_2O_3	2	13	Rh/Pd	8.2	2.67(2)	0.011(1)	2.2	55.5

Table 4.5: Coordination, bondlength and statistical data obtained from analysis of the Rh k edge EDE spectra shown in figure 4.15.

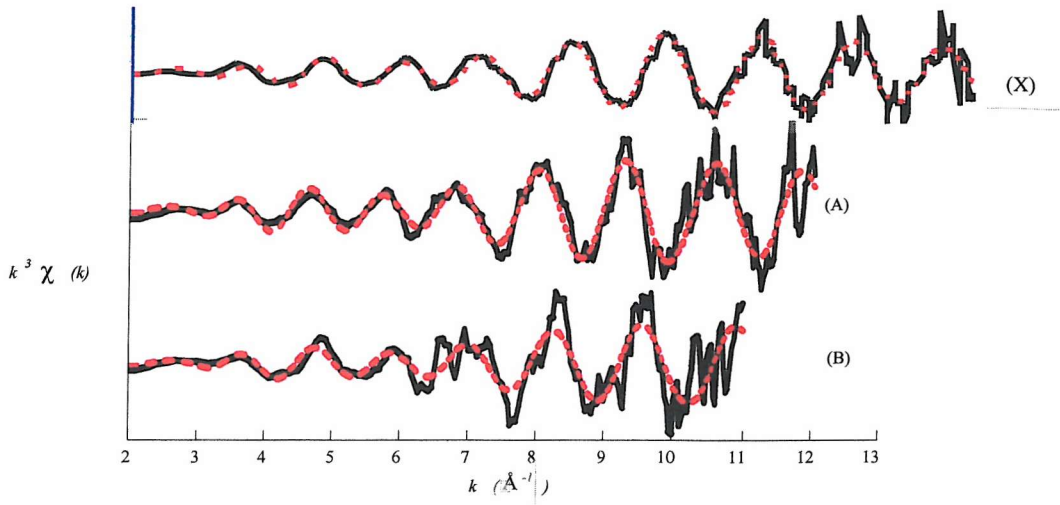

Figure 4.16: k^3-weighted Pd K edge EDE spectra derived from 'fresh' samples: (A) a physical mixture comprising equal weights 5wt% Pd/Rh; (B) 4wt% Rh: 1wt% Pd and (X) 5wt% Pd system for comparison. The figure highlights the apparent amplitude and phaseshift difference between the systems, giving rise to the mentioned physical states.

Sample	k_{min} (Å^{-1})	k_{max} (Å^{-1})	Shell	CN	*r*/Å	$2\sigma^2$/Å^2	E_F	R (%)
(A) 5% Rh/Al_2O_3 + 5%Pd/Al_2O_3 (Physical Mixture)	2	12	Rh/Pd	11.0	2.75(1)	0.012	1.9	48
(B) 4%Rh/1%Pd/Al_2O_3	2	11	Rh/Pd	6.5	2.68(1)	0.011	4.5	59

Table 4.6: Coordination, bondlength and statistical data obtained from analysis of the Pd *k* edge EDE spectra shown in figure 4.16.

The data derived from figure 4.15 reinforce the observations made above for the 4wt% Rh:1wt% Pd system at the Rh *k* edge, where the Rh component has been effectively insulated against room temperature oxidation, highlighted by the increased amplitude and differing phaseshift in the EDE signature. An expected result is obtained from the physical mixture, where the formation of essentially Rh_2O_3 nanoparticles has occurred after room temperature exposure to air, comparable to the result obtained from the 5wt% Rh system.

The data derived from the Pd *k* edge also shows an expected result from the Pd component, it is essentially metallic as N_1^{Pd} values are around 11.

These expected results from the physically mixed system in its 'fresh' state are not however propagated in the systems' behaviour under catalytic conditions, and some interesting observations are made when compared to the alloyed systems. The Fourier

transforms shown in figure 4.17 highlight the marked difference of the Pd component in the physically mixed and 5wt% Pd system, after exposure to the catalytic mixture. The obvious decrease in amplitude for the physically mixed Pd component can be attributed to the differing physical state the Pd is in, explained below. The second shell data shown in the Fourier transforms could assign the physically mixed sample Pd component to have a BCC structure, and the Pd component in the 5wt% Pd system to have an FCC structure. However, the quality of the data obtained is not high enough to solidify this assumption, and the postulation is only one possible explanation of these clear differences.

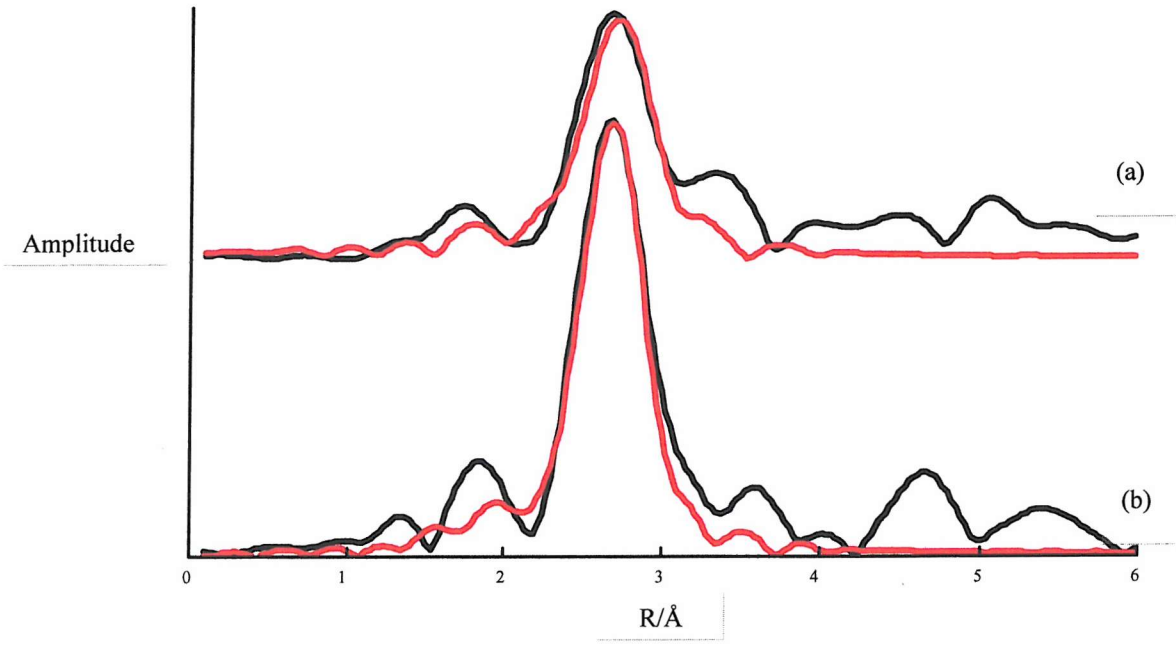

Figure 4.17: Fourier transforms derived from the (a) physically mixed sample; and (b) 5wt% Pd system.

Figure 4.18 shows the $N_1^{Rh/Pd}$ values derived from the Pd *k* edge for the physically mixed sample over the catalytic experiment. After exposure to the catalytic mixture the coordination number of the Pd falls to a relatively low value of ca. 8, which rises to ca. 11 by 400K.

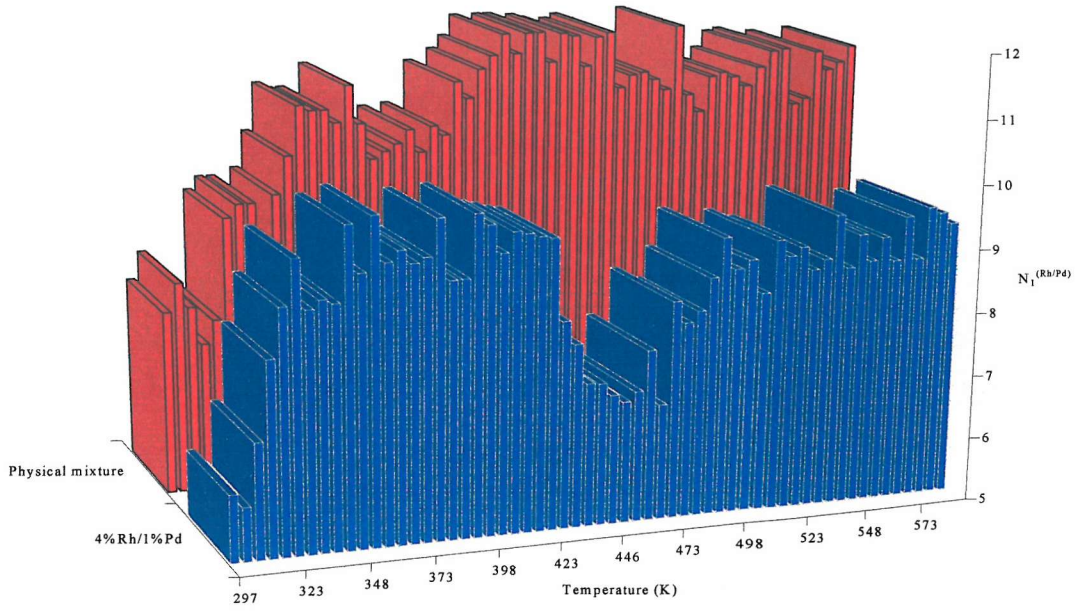

Figure 4.18: Coordination data as a function of temperature for the systems indicated. The data from the Pd *k* edge of the 4wt% Rh:1wt%Pd system is shown for comparison.

This variation in $N_1^{Rh/Pd}$ has a different reason for occurring compared to the 4wt% Rh:1wt% Pd case. The effective room temperature reduction of the physically mixed sample prior to exposure to the catalytic mixture could result in a well-known bulk uptake of H_2. This uptake results in a 'swollen' PdH_x phase, which can be viewed in figure 4.16, the EDE signatures giving differing amplitude and phaseshifts when compared to the Pd only system.

The PdH_x phase bulk structure in this case could therefore be assigned as a BCC structure, as the bulk structures in this case are assigned as a function of stoichiometry. The relatively low N_1^{Pd} values obtained at low temperatures would point to this, as opposed to the FCC structure expected at higher N_1^{Pd} values. The discussion section expands on possible explanations of the observed processes occurring over the Pd component.

The 'BCC' structure therefore collapses at higher temperatures to the 'FCC' Pd structure, as the adsorbed H_2 is lost. Figure 4.19 shows the variation of metal-metal bondlength as a function of temperature derived from the EDE data. The variation in Pd-M bondlengths, compared with the Rh-M bondlengths obtained for the physically mixed system point to the Rh and Pd components existing as discrete entities, as they posses M-M bondlengths comparable to bondlengths obtained from their discrete analogue systems.

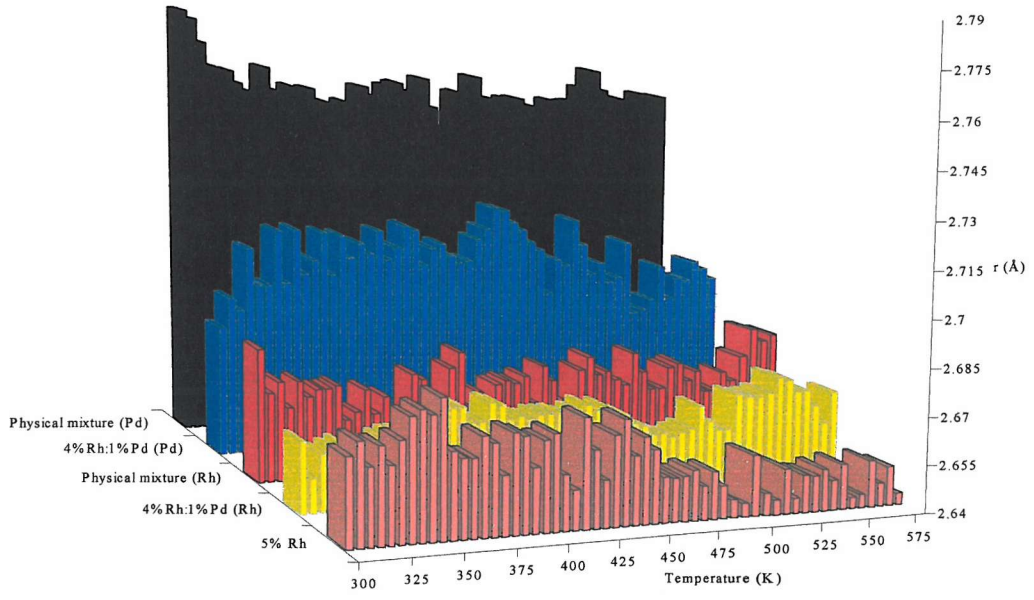

Figure 4.19: Variation of metal bondlengths as a function of temperature for the systems indicated.

The catalytic experiment viewed from the Rh *k* edge also provides an interesting result. Figure 4.20 shows the coordination data obtained from the physically mixed sample.

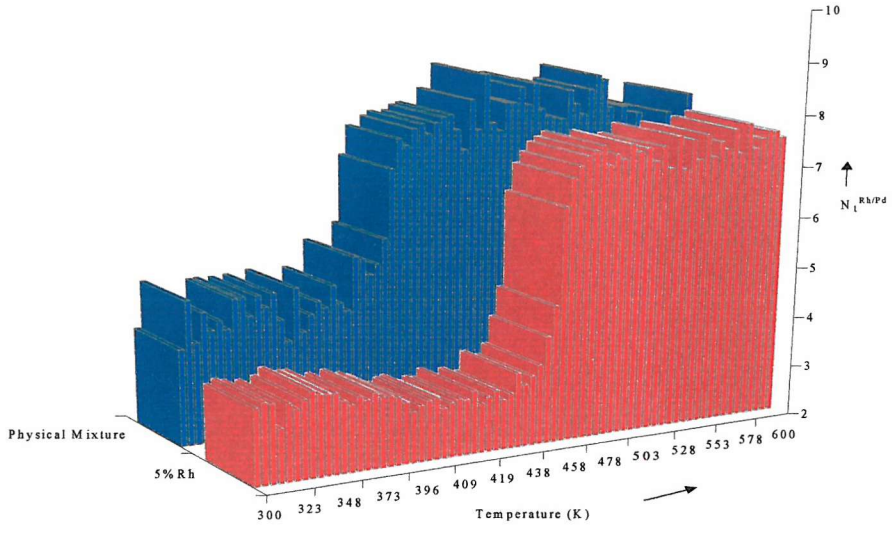

Figure 4.20: Coordination data as a function of temperature for the systems indicated. The data from the Rh *k* edge of the 5wt% Rh system is shown for comparison

The Rh phase is initially seen to be extensively oxidised, an expected result based on previous observations, and the comparability of coordination numbers to the 5wt% Rh system shown in figure 4.20. However, the subsequent collapse of the oxidised Rh phase to the metallic phase is ca. 60K lower than the analogous Rh only system. This observation can also be effectively visualised in figure 4.21, which shows the lowering of light off temperature for the subsequent conversion of NO.

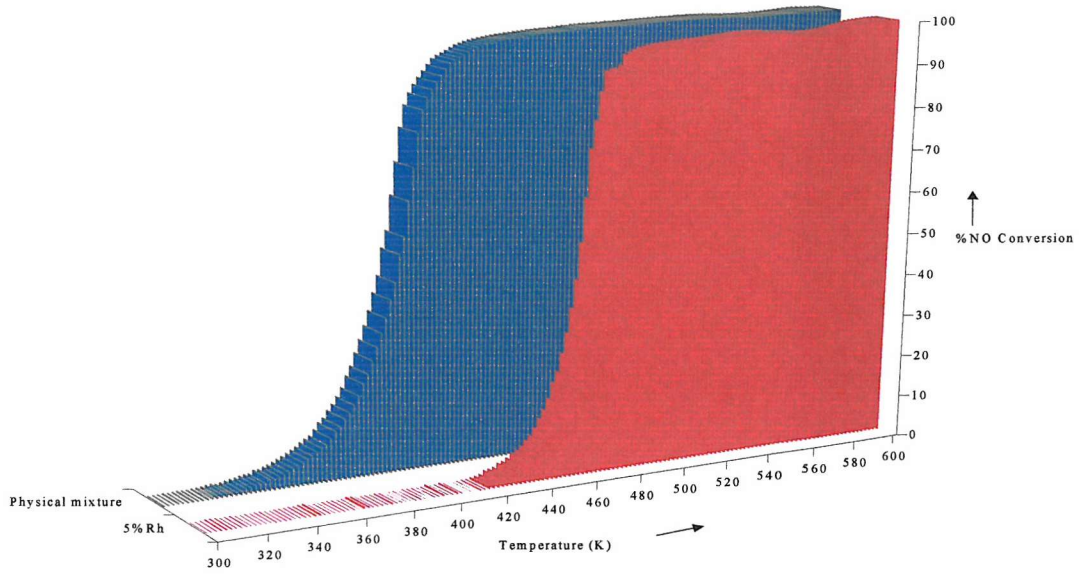

Figure 4.21: NO conversion as a function of temperature for the systems indicated.

This differing activity of the Rh component could be attributed to a process of hydrogen spillover from the Pd component to the Rh metal, occurring between catalyst particles. The physically mixed system is observed to have the same effectiveness of NO removal, under the conditions used, as the other Pd containing systems. This behaviour is observed despite there being no intimate contact between the Rh/Pd components. Similar trends are seen in the inspection of consequent N_2O production. Figure 4.22 shows that there is no apparent difference in the maximal level of N_2O production observed between the systems investigated in this chapter. The reduction of light off temperature being associated with hydrogen spillover is only one possible explanation for this effect. The data does however definitively show that in the presence of physically discrete Pd the reduction of the oxidised Rh phase is promoted. Therefore the only process being able to 'act' over the long distances

required for such an observation to be made is hydrogen spillover from the Pd phase to the Rh phase.

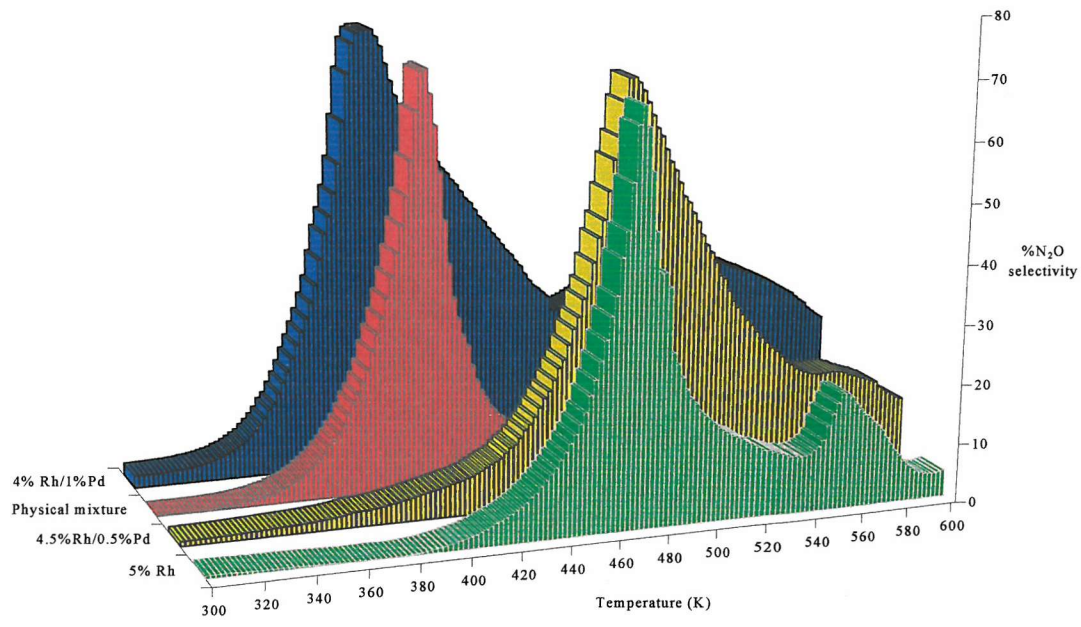

Figure 4.22: N_2O (mass 44) production as a function of temperature for the systems indicated. The figures accurately represent the net N_2O selectivity for the indicated systems in the region of light off only. Data above 500K can be disregarded due to anomalous carbon containing entities.

Although there is a significant reduction in light off temperature observed for the 1wt%Pd system compared with the Rh only system, the relatively high production of N_2O is seen over a much wider temperature range. It is therefore the physically mixed sample that yields the most desirable catalyst under these circumstances, as it exhibits a combination of lowered light off temperature and a relatively narrow thermal window for significant N_2O production. Perhaps the most interesting observation made with the physically mixed sample is the absence of 'Pd like' N_2O selectivity. When compared to the Pd only system, the thermal window for N_2O production is seen to be ca. 90K narrower for the physically mixed sample. The Pd only system also has a slightly lower light off temperature, showing the apparent differences in the Pd components. The Rh component is therefore seen to be the dominating metal in terms of catalytic performance in the physically mixed sample. Further work would be required to delineate any possible explanations for these processes.

The observations described here also underline an apparent synergism occurring in the physically mixed system. This synergism can be viewed as rapid and dynamic processes occurring upon the Pd metal component, which in turn directly affects the Rh component. More specifically, this process can be ascribed to the physically separate Pd having promoted the reductive collapse of the oxidised Rh phase produced by NO dissociation. The observations made above point to the process of H_2 spillover from Pd effectively promoting the reduction of the physically separated oxidised Rh phase. This in turn leads to the promotion of NO reduction, the 'desired' catalytic reaction in this case.

4.5 XPS Study of the Rh/Pd Catalyst Systems

XPS spectra were taken for all of the systems investigated in this chapter in their 'fresh' states. The data obtained from the XPS directly supports the observations made via the EDE experiments.

Figure 4.23 compares the XPS spectra taken from the 0.5wt% Pd and the 1wt% Pd systems. It is evident from the spectra that the Rh component exists in a different phase in each of the systems. In the 0.5wt% case, the binding energy is seen to ca. 308eV, which is consistent with the Rh essentially existing as Rh_2O_3 (BE= ca. 309eV). This ties in with the observations made via EDE, where the Rh component is seen to be susceptible to room temperature oxidation at the low loading of Pd. The spectrum for the 1wt% Pd loading shows the binding energy of the Rh to be ca. 307eV, which correlates well to the signature from metallic Rh. The XPS measurements made here therefore conclusively assign the phase of the Rh to be metallic at the 1wt% Pd loading level. Hence this reinforces the effective the 'insulation' of the Rh component by Pd against oxidation observed in the EDE studies of the 'fresh' systems. The spectra also show the data obtained from the Pd component, in both the systems the data points to the Pd to be in a 'slightly' oxidised state, which is a reasonable result as the EDE showed the Pd not to be 'fully' metallic in its respective 'fresh' state, but this is only one possible explanation. This signature from the Pd would also suggest the Pd to have segregated to the surface; the evidence for this is detailed below.

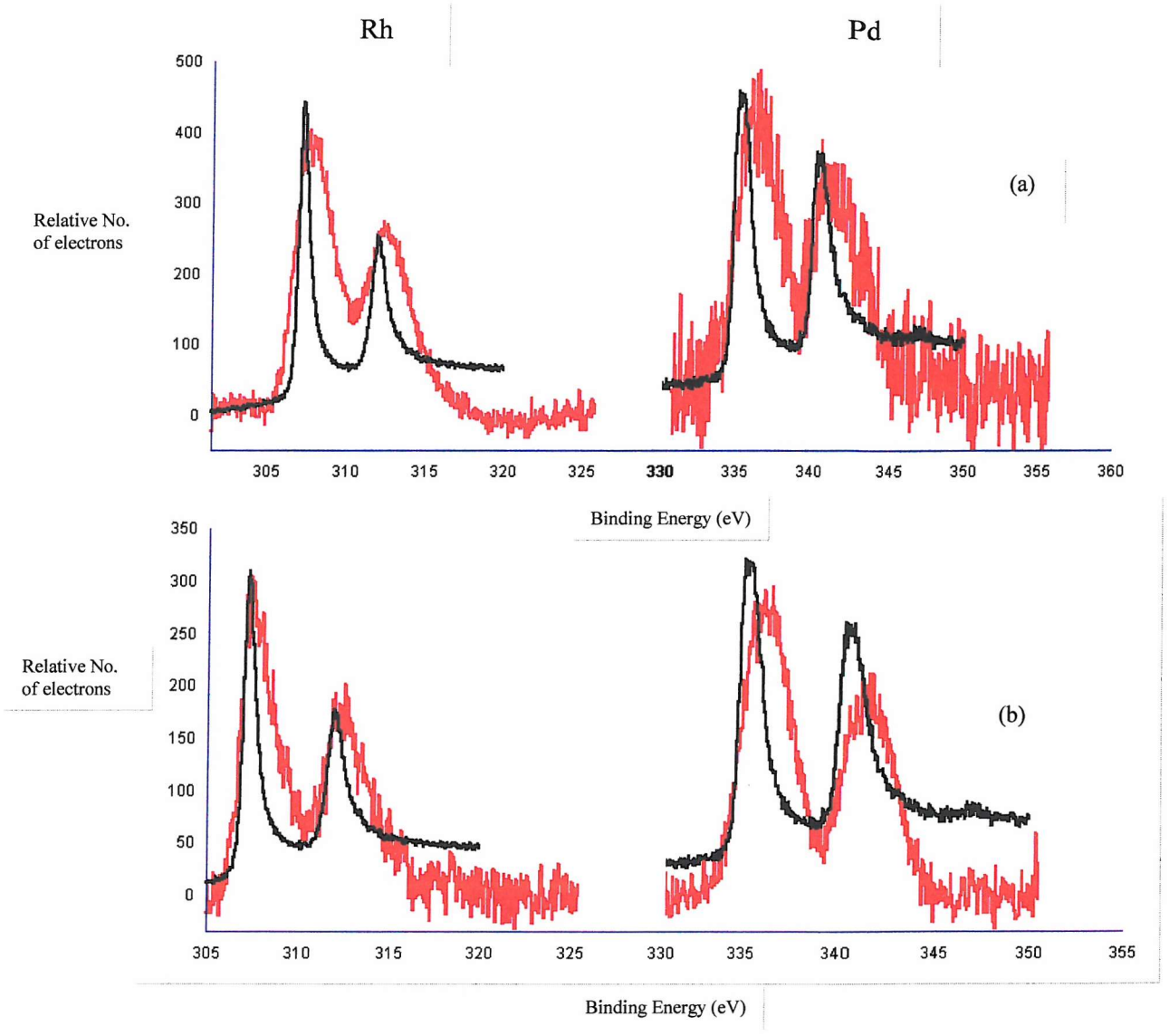

Figure 4.23: XPS spectra taken for (a) 0.5wt% Pd system and (b) 1wt% Pd system, showing both Rh and Pd 3d 5/2 regions; the red line indicates the experimental data; the black line indicates the spectra taken from the respective bulk foil.

The results obtained from the EDE of the alloy systems indicated that the Pd component in the systems had essentially segregated to the surface of the particles. This would in part explain the effective insulation of the Rh component against oxidation. The XPS results also indicate that this is the case, and a large proportion of the Pd has segregated to the surface and can be viewed by the analysis of figure 4.24.

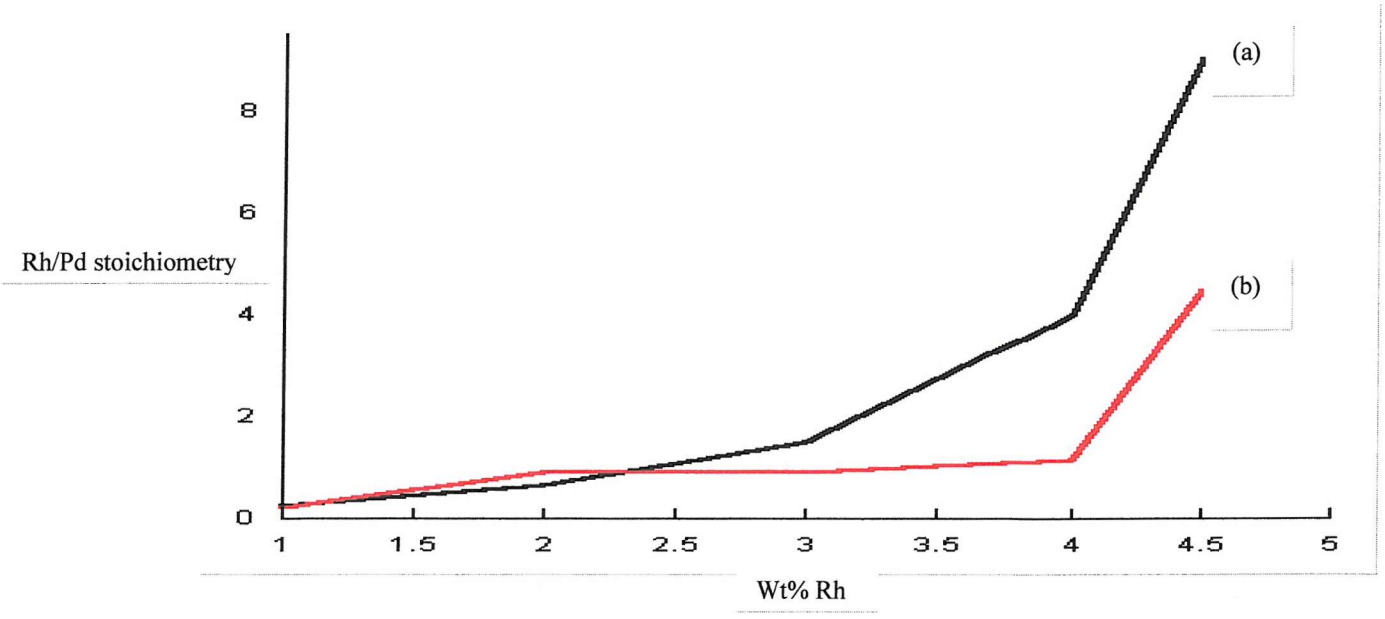

Figure 4.24: Rh/Pd ratio as a function of Rh metal loading; (a) represents the systems in their respective 'homogeneous' states; and (b) represents the experimental values obtained.

It is clear from figure 4.24 that the catalyst systems do not exist as completely homogeneous systems after ca. 2.5wt% Rh metal loading is surpassed. At the 3wt% Rh loading level ca. 1.6 times as much Pd is present at the surface compared to the homogeneous case. This effect is seen to increase markedly by a factor of ca. 2 by the 4wt% Rh level, where there is ca. 3.5 times as much Pd at the surface. The 4.5wt% Rh system has ca. 2 times as much Pd segregated to the surface. These results were obtained with the use of the XPS equation outlined in chapter 2 (equation 2.2, p.18), and data set (b) was attained by applying the relevant sensitivity factors to the 'homogeneous' data.

The XPS results obtained here therefore semi-quantitatively explain the 'fresh' states that are seen via EDE measurements for the catalyst systems. There is enough Pd present at the surface in the 1wt% Pd system for the Rh to be completely insulated against any oxidation, subsequently it would be reasonable to suggest that all of the Pd has segregated to the surface in the 0.5wt% Pd system, but an inadequate coverage of the surface means that the Rh component can be partially oxidised. This would suggest an inherent loading limit to which total, and 'effective', coverage of the particle surface by Pd could be attained. This limit would seem to be between the 0.5-1wt% Pd loading. Although the XPS data indicates the 2wt% Rh system to be essentially homogeneous, the EDE shows the Rh component to be

metallic in its 'fresh' state. This would in turn suggest another loading limit of Pd, where there is enough Pd present to promote the 'insulating' effect, irrespective of any segregation to the surface.

These factors regarding the behaviour of Pd in these systems can be rationalised by considering the extent of 'influence' Pd has on the surface of an atypical particle. This atypical particle, taken as an 'average' particle from the available data, assumes an average coordination of 8 around a Pd atom, and an average hemispherical particle size of 32.5Å containing 989 atoms in total and 416 surface atoms, giving a total particle surface area of ca. 830Å^2. If all of the Pd were assumed to have segregated to the surface and to lie in a [111] plane, then a Pd atom would essentially influence an area of ca. 25Å^2. Therefore, within a [111] plane, a single Pd atom would 'influence' all 8 adjacent Rh atoms. This means that only a small fraction of Pd needs to be present to have a direct influence on the adjunct metal, which is successfully shown by the complimentary techniques used in this chapter.

The amount of chlorine retained by these systems, semi-quantitatively assessed by the XPS measurements, yielded some interesting results. Figure 4.25 shows the Rh:Cl ratio as a function of Rh metal loading.

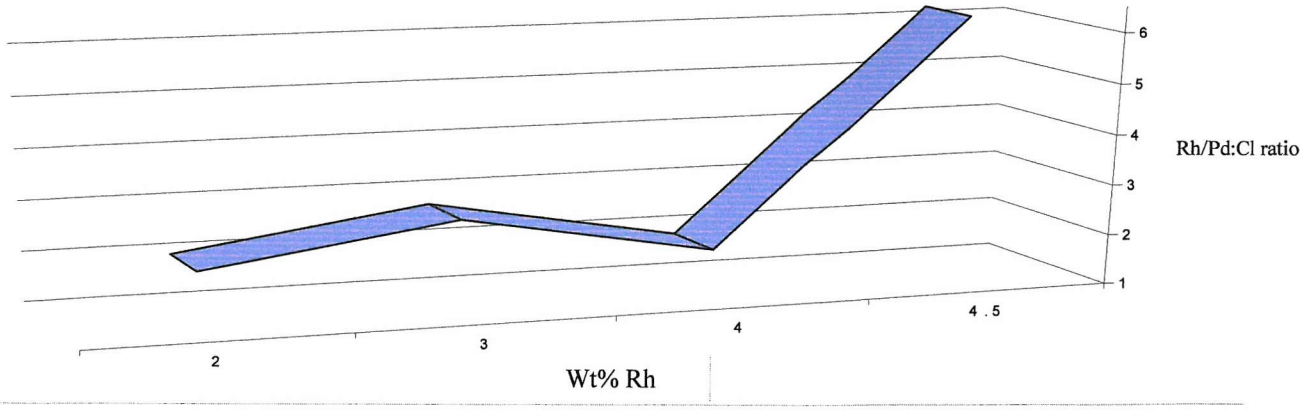

Figure 4.25: Rh/Pd:Cl ratio as a function of Rh metal loading, after applying the relevant sensitivity factors. The 5wt% 'Pd only' system gave a value of 17.14.

It is evident from the figure that the catalyst systems retain a relatively large amount of chlorine compared to their 'metal only' analogues. Interestingly, the 2wt%, 3wt% and 4wt% Rh systems all retain the approximately the same high amount of chlorine, but the 4.5wt% system retains much less, by a factor of 3. This lack of retention could be due to the physical

state of the catalyst derived from the EDE and XPS data, where Pd is at low concentrations at the surface. As the XPS technique samples 'layers' of the nanoparticle, it would be reasonable to suggest that the primary layers, that are palladium rich, are influencing the results obtained. A conclusion drawn from this could be that the catalysts exhibiting partial or full homogeneity retain a high and similar amount of chlorine.

4.6 Discussion and Conclusions

The primary reason for alloying palladium, as an adjunct metal with rhodium, in this study was to potentially minimise or eliminate the oxidised phase of the Rh component that was the source of the 'unwanted' N_2O production in the previous chapter.

However, the results from the catalytic experiments performed on the alloyed systems point to the Pd itself acting to produce N_2O in certain temperature domains. A scrutiny of existing work reveals that this observation is an intrinsic catalytic property of Pd. Palladium is seen to promote the production of N_2O in a variety of catalytic reactions upon low dispersed and single crystal surfaces,[5,6] most notably in the NO-CO reaction[7] and similar studies using the reduction of NO by H_2.[8] All of the studies point to Pd exhibiting a propensity for N_2O production, in one case persisting throughout the catalytic regime employed (NO-CO reaction; 335-573K).[8]

This behaviour is also observed for highly dispersed Pd systems, an effective example being a comparison of the CO-NO reaction over Pd using single crystal and supported Pd systems.[7] The study found that the highly dispersed system was more effective at NO dissociation than the single crystal system, yet this did not have an effect on the overall production of unwanted N_2O. Studies dealing with the action of NO over Pd[9,10] delineate one of the reasons why this property is observed, the 'borderline' between dissociative and molecular adsorption passes between Rh and Pd. Metals including and to the left of (metallic) Rh relatively easily dissociate NO, whereas this is not the case for Pd (N and O adsorbates are strongly bound).

The catalytic study of the Pd only system therefore effectively showed this behaviour, and that this propensity for N_2O production is not due to any change in phase as it was in the case of the Rh metal. The majority of the surface science studies noted above made use of mono-layered Pd to show the behaviour of the metal, therefore only a small fraction of Pd is required for 'Pd like' catalytic behaviour to occur, an effect which is seen successfully in the catalyst systems studied in this chapter. The TEM data obtained from the Pd only system yielded expected values for particle sizes and distributions when compared to previous studies[7] of supported Pd nanoparticles, although a much wider range (ca. 18-150Å) of particle distributions were seen for the 5wt%Pd/Al_2O_3 system.

An interesting observation is made when comparing the physical mixture and the Pd only system. The metal component present in the Pd only system exhibits markedly different behaviour compared to the Pd present in the physical mixture. The physical mixture demonstrates a narrower thermal window in which N_2O is produced, compared not only with the Pd only system but also with all the catalytic systems studied. Inspection of the available data points to the Pd having a different physical structure, where the Pd 'stockpiles' H_2. This retention in turn means that 'Pd like' behaviour is not seen under catalytic conditions, and the Rh component is catalytically dominant.

The promotion of the Rh phase change could be due to three factors. Firstly, electron transfer could occur from the Pd metal to the Rh, which would act over a short range only. A gas phase transfer of desorbed species (i.e. H_2/atomic H) could also be taking place from the Pd constituent. However, due to the distances involved for any influence from the Pd component to occur in a physically mixed system, a long-range effect would be the most likely explanation for the effect seen. The consequently desorbed species could therefore either recombine to the gas phase and be available for further reactions over the Rh, or the well known catalytic effect of H_2 spillover from the 'swollen' BCC PdH_x phase to the metallic Rh phase could be occurring. Considering all the available data from this study, it would be reasonable to conclude that the latter explanation would be feasible to explain the processes occurring. Other factors that could rationalise the structural effects seen prior to the catalytic experiment could be the Pd phase effectively 'wetting' the surface of the system, yielding monolayered Pd, which could account for the activity observed. The use of static or dynamic Debye-Waller factors to analyse the EDE data for this system could also be significant in understanding the processes involved. Due to the complexity of the processes occurring before and during catalysis, the physically mixed sample needs further investigation to delineate any significant conclusions.

The study of the alloyed systems demonstrated the fact that, in this case, nanoparticulate catalytic behaviour is not predictable by bulk structures, which is utilised by the majority of the work noted above. Chapter 1 discussed bulk Rh and Pd to be essentially immiscible across the compositional range,[2,3] but the supported systems studied here show that in the nano regime alloying occurs, yielding some interesting results. The EDE and XPS of the 'fresh' alloy systems showed the Pd to have segregated to the surface. This segregation leads

to the effective insulation of the Rh component against the room temperature oxidation seen in the previous chapter. The XPS also highlighted that only a small fraction of Pd is needed at the surface for this effect to occur. This effect can be 'finely tuned' to achieve differing phases of the Rh component (i.e. varying the Pd loading from 0.5-1wt%). Similar photoemission studies[13] on Pd/Rh [111] surfaces have found comparable Pd 'dominance' over the Rh component at low temperatures (<380K) in the dissociation of NO_2 species. However, although the objective of the elimination of the bi-stable Rh phase is achieved, the Pd component in the systems is seen to be dominant under the catalytic conditions employed. This means that the intrinsic property of N_2O selectivity, noted above, is present for these catalysts, as no 'intermediate' is seen with the Pd phases.

The physical mixture catalyst is therefore, somewhat surprisingly, found to be the 'desired' catalyst within the scope of this study. The Pd component is found to 'communicate' with the Rh via what is most likely H_2 spillover. This indicates that the oxidation of Rh still occurs, but the promotion of this phase to the metallic phase, that is highly selective for NO reduction, occurs at much lower light off temperatures. The absence of 'typical' Pd like catalytic behaviour, i.e. when compared to a Pd only system, shows a physical result of the proposed H_2 spillover occurring. These results are in stark contrast to previous related work,[11,12] where preferential synergistic and catalytic behaviour was seen for similar bimetallic Rh/Pd systems and not for the physical mixture, under the CO-NO reaction.

In conclusion, the *in situ*, time resolved, double edge EDE/MS experiments has allowed the observation of a range of dynamic processes occurring over the catalyst systems during the reduction of NO by H_2. The complimentary probes utilised showed the physical behaviour of the systems in unprecedented detail, both statically and in time-resolved studies. The results obtained from the co-impregnated Rh/Pd systems show that the metal components will form alloyed particles on the nanoscale. The nanoparticulate surface is therefore initially Pd rich, this enrichment reduces the rapid oxidation of the Rh metal component by NO. This effect is only observed when a certain, critical metal loading of Pd is reached. The effective result of this in terms of catalysis is the significant lowering of light off temperatures, as the 'unwanted' NO stabilised oxidised Rh phase is circumvented. However, the intrinsic chemistry of the Pd component implies that the production of N_2O

cannot be avoided, even with the 'desired' physical mixture system, and that another concept needs to be evoked for this effect to be eliminated.

4.7 References

(1) M. Harada, K. Asakura, Y. Ueki, N. Toshima, *J. Phys. Chem.*, 1993, **97**, 10742.

(2) H. Noh, J.D. Clewley, T.B. Flanagan, A.P. Craft, *Journal of alloys and compounds*, 1996, **240**, 235.

(3) Y. Wang, J.S. Faulkner, *Phys. Rev. Lett.*, 1993, **70**, 3287.

(4) Y.J. Mergler, D.R.G. Ramsarangsing, B.E. Nieuwenhuys, *Recueil des travaux chimiques des pays bays*, 1994, **113**, 110.

(5) K. Alumusaiteer, S.S.C. Chuang, *J. Catal.*, 1999, **189**, 189.

(6) J. Nováková, *Appl. Catal. B.*, 2001, **30**, 445.

(7) D.R. Rainer, S.M. Vesecky, M. Koranne, W.S. Oh, D.W. Goodman, *J. Catal.*, 1997, **167**, 234.

(8) N.W. Cant, D.E. Angove, D.C. Chambers, *Appl. Catal. B.*, 1998, **17**, 63.

(9) D. Loffreda, F. Delbecq, D. Simon, P. Sautet, *J. Chem. Phys.*, 2001, **115**, 8101.

(10) W.A. Brown, D.A. King, *J. Phys. Chem. B.*, 2000, **17**.

(11) S.H. Oh, J.E. Carpenter, *J. Catal.*, 1986, **98**, 178.

(12) P. Araya, C. Ferrada, J. Cortés, *Catal. Lett.*, 1995, **35**, 175.

(13) T. Jirsak, J. Dvorak, J.A. Rodriguez, *Surf. Sci.*, 1999, **436**, 683.